



Université du Québec
à Rimouski

**DYNAMIQUE SÉDIMENTAIRE HOLOCÈNE DANS LE
DÉTROIT DE JONES RECONSTITUÉE À PARTIR DES
CAROTTES SÉDIMENTAIRES RECUEILLIES DANS LA
BAIE DE BELCHER (CALOTTE GLACIAIRE DE DEVON,
NUNAVUT, CANADA)**

Mémoire présenté
dans le cadre du programme de maîtrise en océanographie
en vue de l'obtention du grade de maître ès en sciences

PAR
© Jade Brossard

26 avril 2021

Composition du jury :

André Rochon, président du jury et examinateur interne, ISMER-UQAR

Anne Jennings, examinatrice externe, INSTAAR, University of Colorado

Jean-Carlos Montero-Serrano, directeur de recherche, ISMER-UQAR

Guillaume St-Onge, codirecteur de recherche, ISMER-UQAR

Dépôt initial le 13 janvier 2021

Dépôt final le 26 avril 2021

UNIVERSITÉ DU QUÉBEC À RIMOUSKI
Service de la bibliothèque

Avertissement

La diffusion de ce mémoire ou de cette thèse se fait dans le respect des droits de son auteur, qui a signé le formulaire «*Autorisation de reproduire et de diffuser un rapport, un mémoire ou une thèse*». En signant ce formulaire, l'auteur concède à l'Université du Québec à Rimouski une licence non exclusive d'utilisation et de publication de la totalité ou d'une partie importante de son travail de recherche pour des fins pédagogiques et non commerciales. Plus précisément, l'auteur autorise l'Université du Québec à Rimouski à reproduire, diffuser, prêter, distribuer ou vendre des copies de son travail de recherche à des fins non commerciales sur quelque support que ce soit, y compris l'Internet. Cette licence et cette autorisation n'entraînent pas une renonciation de la part de l'auteur à ses droits moraux ni à ses droits de propriété intellectuelle. Sauf entente contraire, l'auteur conserve la liberté de diffuser et de commercialiser ou non ce travail dont il possède un exemplaire.

REMERCIEMENTS

Je tiens tout d'abord à remercier sincèrement mon directeur **Jean-Carlos Montero-Serrano** pour ce beau projet de maîtrise et pour les expériences à bord du NGCC Amundsen. Je voudrais aussi remercier mon codirecteur **Guillaume St-Onge** pour son implication et ses précieux commentaires. Merci aussi à tous les techniciens et techniciennes de laboratoire; **Dominique Lavallée, Mathieu Babin, Quentin Beauvais et Claude Belzile** pour leur aide constante avec les instruments de mesures à l'ISMER. Je voudrais aussi remercier **Édouard Philippe, Quentin Duboc et Myriam Caron** pour leur aide précieuse et pour avoir toujours répondu à mes nombreuses questions. Merci à ma collègue et grande amie **Anne Corminboeuf** et à **Maria-Emilia Rodriguez** pour les beaux moments passés en mer. Merci au capitaine et à l'équipage du NGCC Amundsen pour les deux merveilleuses expéditions en Arctique. Merci à mes collègues et amis d'*ArcTrain* pour les beaux moments partagés en congrès et sur le terrain.

Un grand merci à mes colocs et amis **Bruno St-Denis, Jonathan Pierron, Mélanie Cleton** et **Alexandre DuFraysseix** pour les bons moments, les fous rires constants et les bons repas partagés. Merci à **Joanie Roy** pour les escapades, les tours d'auto et les soirées films, tu as toujours su me changer les idées. J'aimerais aussi remercier mes deux âmes sœurs **Liza St-Germain et Laurence Renaud** pour leur soutien, leur présence malgré la distance et leur sens de l'humour unique. Finalement, un gros merci à **Élie Dumas-Lefebvre** pour avoir toujours été à mes côtés dans les hauts et bas de ce projet et dans la vie en générale, et merci à **mes parents** qui m'ont toujours encouragé peu importe la voie que je prenais.

AVANT-PROPOS

Ce mémoire de maîtrise est présenté en trois parties: une introduction générale rédigée en français, d'un chapitre principal rédigé en anglais sous la forme d'article scientifique en prévision d'être soumis pour publication à la revue internationale «BOREAS», et une brève conclusion générale rédigée en français. L'article présenté dans ce mémoire de maîtrise : Brossard, J., Montero-Serrano, J.-C., St-Onge, G. *Holocene sedimentary dynamics in Jones Sound as recorded in sediment cores from Belcher Inlet (Devon Ice Cap, Nunavut, Canada)*, et a été rédigé par moi-même avec la supervision des professeurs Jean-Carlos Montero-Serrano et Guillaume St-Onge de l'ISMER-UQAR. En tant que premier auteur, ma contribution fut la réalisation des analyses de laboratoire des différents traceurs minéralogiques, géochimiques et paléomagnétiques et la rédaction de l'article. Les professeurs Jean-Carlos Montero-Serrano et Guillaume St-Onge ont fourni l'idée originale, l'implémentation du développement de la méthode et la formation nécessaire pour réaliser les analyses de laboratoires, et ont contribué à la rédaction et révision de l'article. Quentin Beauvais (ISMER-UQAR) à effectuer les analyses de propriétés physiques des carottes, alors que les analyses des isotopes stables du carbone et de l'azote et les mesures de ^{210}Pb ont été effectuées par les techniciens du centre de recherche GEOTOP (Montréal, Canada).

Au cours ma maîtrise, j'ai eu l'opportunité de présenter les principaux résultats de mon projet de recherche lors de divers congrès nationaux et internationaux:

Brossard, J., Montero-Serrano, J.-C., St-Onge, G. (2019). *Holocene sedimentary dynamics of the Belcher Glacier (Devon Ice Cap, Nunavut, Canada)*. ArcticNet réunion scientifique annuelle, 2-5 décembre 2019, Halifax, Canada. Affiche et présentation (Prix du public : Elevator Pitch Contest).

Brossard, J., Montero-Serrano, J.-C., St-Onge, G. (2019). *Sedimentary record of the Belcher glacier dynamics (Devon Ice Cap, Nunavut, Canada) during the last centuries*. Réunion scientifique d'ArcTrain, 16-20 septembre 2019, Rimouski, Canada. Affiche et présentation.

Brossard, J., Montero-Serrano, J.-C., St-Onge, G. (2019). *Holocene sedimentary dynamics of the Belcher glacier (Devon Ice Cap, Nunavut, Canada)*. European Geosciences Union (EGU), 7–12 Avril, Vienne, Autriche. Affiche.

Brossard, J., Montero-Serrano, J.-C., St-Onge, G. (2019). *Holocene sedimentary dynamics of the Belcher Glacier (Devon Ice Cap, Nunavut, Canada)*. Réunion scientifique annuelle du GEOTOP, 22-24 mars 2019, Jouvence, Canada. Présentation.

Brossard, J., Montero-Serrano, J.-C., St-Onge, G. (2018). *Sedimentary record of the Belcher glacier dynamics (Devon Ice Cap, Nunavut, Canada) during the last centuries*. Réunion scientifique annuelle d'Arctrain, 29 octobre au 2 novembre 2018, Jouvence, Canada. Affiche et présentation.

Brossard, J., Montero-Serrano, J.-C., St-Onge, G. (2018). *Sedimentary dynamics of the Belcher Glacier (Devon Ice Cap, Nunavut) during the last centuries*. réunion scientifique annuelle, 10-14 décembre 2019, Ottawa, Ontario, Canada. Affiche et présentation.

Brossard, J., Montero-Serrano, J.-C., St-Onge, G. (2018). *Dynamique sédimentaire du glacier Belcher (calotte glaciaire du Devon, Nunavut) durant les derniers siècles*. Réunion scientifique annuelle de Québec-Océan, 5 au 6 Novembre, Rivière-du-Loup, Québec, Canada. Affiche et présentation.

Brossard, J., Montero-Serrano, J.-C., St-Onge, G. (2017). *Holocene sedimentary dynamics of the Belcher Glacier (Devon Ice Cap, Nunavut, Canada)*. Réunion scientifique annuelle du GEOTOP, 22-24 mars 2017, Malbaie, Canada. Affiche et présentation.

J'ai également eu l'opportunité d'embarquer à bord du NGCC Amundsen à l'été 2018 et à l'été 2019 dans l'Arctique canadien pour fournir mon aide pour les opérations de carottage et pour les échantillonnages de rivières et de glaciers. J'ai co-organisé le congrès annuel, ainsi que l'école d'été du regroupement étudiant *ArcTrain* à Rimouski à l'automne 2019. J'ai aussi donné divers ateliers scientifiques, soit dans le cadre du cours de Paléo-

océanographie et paléoclimatologie à l'hiver 2019 et dans le cadre de l'école d'été en océanographie au printemps 2019.

RÉSUMÉ

Une carotte à boîte (27BC) et une carotte à piston (02PC) ont été recueillis près du glacier Belcher (calotte glaciaire de Devon, Nunavut, Canada), pour analyser les propriétés physiques, minéralogiques, géochimiques (élémentaires et isotopiques) et magnétiques afin de reconstituer la dynamique sédimentaire holocène dans le détroit de Jones et la baie de Belcher depuis la dernière déglaciation. Dans un premier temps, la chronologie des carottes a été établie en combinant des analyses de ^{210}Pb , AMS ^{14}C et des données paléomagnétiques. Les propriétés physiques et les traceurs détritiques, ainsi que des modèles de mélange de sédiments, illustrent la transition d'un régime glaciaire à un régime postglaciaire dans la baie Belcher. Des sédiments laminés riches en kaolinite et chlorite sont observés à la base de la carotte 02PC (avant 12,6 cal ka BP) et ont probablement été déposés dans un environnement glaciomarin proximal dominé par des panaches turbides de sédiments provenant des eaux de fonte sous-glaciaires de la marge glaciaire de l'Inlandsis innuitien. Au cours de la période de déglaciation (12,6 et 8 cal ka BP), la présence de nombreux galets, la prédominance de sédiments grossiers, les concentrations élevées de carbonates détritiques et de feldspaths et les valeurs élevées de Ca/Fe et Zr/Al, suggèrent que la dynamique sédimentaire était principalement contrôlée par le vêlage d'icebergs (IRD) et par la décharge d'eau de fonte lié à la déglaciation du bassin de Jones. Au cours de cette période, le retrait progressif de la glace du bassin de Jones et le retrait du glacier Belcher jusqu'au trait de côte actuel sont caractérisés dans la carotte 02PC par une couche de IRD riche en carbonate détritique datée entre 11,2 et 10,3 cal ka BP et par une couche de IRD riche en feldspath datée entre 10,3 et 9,7 cal ka BP, respectivement. Durant l'Holocène moyen et tardif (8,0 à 0,8 cal ka BP), les indicateurs détritiques suggèrent que la dynamique sédimentaire au sein de la baie de Belcher était influencée par des changements régionaux du niveau marin, par l'intensification du courant ouest groenlandais, et par la diminution à long terme de l'insolation estivale boréale. Finalement, des tendances similaires sont observées dans les indicateurs détritiques de la carotte 27BC et dans les anomalies de température de l'air à la surface de l'Arctique depuis la fin des années 1800. Ceci suggère

que l'augmentation des températures atmosphériques a un impact sur la dynamique du glacier Belcher depuis le début de la période industrielle.

Mots clés: Île de Devon; détroit de Jones; Holocène; minéralogie; géochimie; dynamique glaciaire; dynamique sédimentaire.

ABSTRACT

The sedimentological, mineralogical, geochemical (elemental and isotopic), and magnetic properties of two sediment cores (27BC and 02PC) recovered from the Belcher Inlet (Devon Ice Cap, Nunavut, Canada) were investigated to document changes in the sediment dynamics in Jones Sound and Belcher Inlet related to climate variability since the last deglaciation. The chronostratigraphic framework of these cores was developed by combining ^{210}Pb , AMS- ^{14}C , and paleomagnetic analyses. Physical properties and detrital proxies, together with unmixing of the sediment composition, illustrate the transition from a deglacial to a postglacial regime in the Belcher Inlet. Kaolinite- and chlorite-rich laminated glacial sediments (prior to 12.6 cal ka BP) in core 02PC were likely deposited in an ice-proximal setting dominated by subglacial meltwaters plumes associated with the grounding line retreat of the Innuitian Ice Sheet margin into the Jones Sound basin. During the deglaciation phase (12.6 and 8.0 cal ka BP), the presence of numerous pebbles, the dominance of coarse-grained sediments, high concentrations of detrital carbonates and feldspars, and high Ca/Fe and Zr/Al values suggest that the sediment dynamics were mainly controlled by ice rafting debris (IRD) and meltwater discharge related to the deglaciation of the Jones Sound basin. At this time, the progressive ice retreat of the Jones Sound basin and retreat of the Belcher Glacier to the present coastline are typified in core 02PC by a detrital carbonate-rich IRD layer dated at 11.2 to 10.3 cal ka BP and by a feldspar-rich IRD layer dated at 10.3 to 9.7 cal ka BP, respectively. During the middle to late Holocene (8.0 to 0.8 cal ka BP), detrital proxies suggest that the sedimentary dynamics in the Belcher Inlet were probably influenced by changes in regional sea level, the intensification of the West Greenland Current and the long-term decrease in boreal summer insolation. Finally, the similar trend observed between the detrital proxies in core 27BC and the Arctic surface air temperature anomalies since the late 1800s suggests that increased atmospheric temperatures have an important influence on the Belcher Glacier dynamics during the industrial period.

Keywords: Devon Island; Jones Sound; Holocene; mineralogy; geochemistry; glacier dynamics; sediment dynamics.

TABLE DES MATIÈRES

AVANT-PROPOS	viii
RÉSUMÉ.....	xi
ABSTRACT.....	xiii
TABLE DES MATIÈRES	xv
LISTE DES TABLEAUX	xvii
LISTE DES FIGURES	xviii
LISTE DES ABRÉVIATIONS, DES SIGLES ET DES ACRONYMES	xxiv
INTRODUCTION GÉNÉRALE	26
CONTEXTE SCIENTIFIQUE ET PROBLÉMATIQUE.....	26
OBJECTIFS DE RECHERCHE ET APPROCHE MÉTHODOLOGIQUE	29
PRÉSENTATION DE LA ZONE D'ÉTUDE	31
CIRCULATION OCÉANIQUE	32
SÉDIMENTATION ET GÉOLOGIE.....	34
Holocene sedimentary dynamics of the Belcher glacier as recorded in sediment cores from Belcher inlet, jones sound, nunavut	37
1. INTRODUCTION	39
2. REGIONAL SETTING	39
2.1. OCEANIC CIRCULATION.....	39
2.2. SURROUNDING GEOLOGY AND SEDIMENTATION IN JONES SOUND.....	41
3. MATERIALS AND METHODS.....	42
3.1. CORING AND SAMPLING	42
3.2. MULTI-SENSOR CORE LOGGER ANALYSES	43
3.3. GRAIN-SIZE DISTRIBUTION AND END-MEMBER MODELING ANALYSES.....	43
3.4. ELEMENTAL GEOCHEMISTRY	44
3.5. QUANTITATIVE BULK MINERALOGY.....	45

3.6. CARBON AND NITROGEN ANALYSES	45
3.7. MAGNETIC AND PALEOMAGNETIC ANALYSES.....	46
3.8. CHRONOSTRATIGRAPHIC FRAMEWORK	47
3.9. STATISTICAL APPROACH.....	49
3.10. SEDIMENT SOURCES AND UNMIXING MODEL	49
4. RESULTS AND INTERPRETATIONS	50
4.1. CHRONOLOGY OF THE CORES	50
4.2. MINERALOGICAL AND GEOCHEMICAL ASSOCIATIONS	56
4.3. ORGANIC CARBON SOURCES.....	57
4.4. GRAIN SIZE END-MEMBERS.....	58
4.5. SEDIMENTARY UNITS	61
4.6. SEDIMENT PROVENANCE	66
5. DISCUSSION	68
5.1 UNIT 1: GLACIAL SEDIMENT DYNAMICS (PRIOR TO 12.6 CAL KA BP)	68
5.2. UNIT 2: DEGLACIAL/EARLY HOLOCENE SEDIMENT DYNAMICS (12.6 TO 8.2 CAL KA BP).....	69
5.3. UNIT 3A: MIDDLE TO LATE HOLOCENE SEDIMENT DYNAMICS (8.0 CAL KA BP TO 800 AD)	72
5.4. UNIT 3B AND 3C: LATE HOLOCENE TO MODERN SEDIMENT DYNAMICS (800 AD TO PRESENT)	74
6. SUMMARY AND CONCLUSION	82
7. ACKNOWLEDGMENTS	83
CONCLUSION GÉNRALE.....	85
ANNEXES	88
RÉFÉRENCE S BIBLIOGRAPHIQUES	96

LISTE DES TALBEAUX

Table 1. Location, water depth and length of the two sediment cores used in this study.....	43
Table 2. Radiocarbon ages from core 02PC. The ages were calibrated with the Marine20 calibration curve with a $\Delta R = 157 \pm 17$ (Heaton et al., 2020).	49
Table 3. Paleomagnetic chronostratigraphic markers (tie points) used in this study. The points marked with I, D and P correspond to inclination, declination and RPI, respectively (Fig. 9). The age is expressed in cal ka BP.	54

LISTE DES FIGURES

Fig. 1. Carte schématique (England et al., 2006) de la dernière glaciation. Le bleu représente l’Inlandsis innuitien, le vert l’ouest de l’Inlandsis groenlandais et en rouge, le nord de l’Inlandsis laurentidien.....	29
Fig. 2. Profil sismique (3,5 kHz) avec la localisation des carottes à boîte (27BC) et à piston 02PC) étudiés dans le cadre de ce projet de maîtrise.	31
Fig. 4. Carte géologique simplifiée du bassin de Jones (adaptée de Zhang et al., 2016) et une image sentinelle du glacier Belcher, avec la localisation du carottage (point rouge), le vêlage d’icebergs (VI) et les plumes turbides de sédiments (PT).....	35
Fig. 5. Location of cores 27BC and 02PC (black star). The oceanic circulation is represented by red and blue arrows. Red arrows illustrate the West Greenland Current (WGC), a warm and salty current, while blue arrows represent the Baffin Island Current (BIC), a cold Arctic current. Red, green and yellow circles denote sediment cores mentioned in the text.....	39
Fig. 6. Bedrock geology of Jones Sound (adapted from Trettin, 1991 and Zhang et al., 2016) showing the location of the sediment source samples discussed in this study.	42
Fig. 7. (A) ^{210}Pb total activity in the top 20 cm of core 27BC. The vertical line represents the supported ^{210}Pb activity (asymptote = 41.9 mBq g $^{-1}$). (B) Logarithm of excess ^{210}Pb activity used for the estimation of mean sedimentation rates (SR). The gray boxes in (A) and (B) represent the biological mixing zones. (C) Age-depth model for the first 12 cm of core 27BC.	51

Fig. 8. Magnetic properties for core 02PC. X-ray computed tomography images (X-CT) of the core; High-resolution digital image (HRI); natural remanent magnetization (NRM), anhysteretic remanent magnetization (ARM), isothermal remanent magnetization (IRM), saturated isothermal remanent magnetization (SIRM) calculated for the demagnetization range from 10-50 mT; MDF _{NRM} (mT) is a magnetic mineralogy indicator; k _{ARM} /k _{LF} is a magnetic grain-size indicator (lower values indicate an enhanced contribution of coarser magnetic grains, whereas higher values indicate finer magnetic grains; Banerjee et al., 1981). Distinct lithological facies are delimited by red lines. Unreliable intervals for paleomagnetic reconstruction are highlighted in gray.	52
Fig. 9. Full vector paleomagnetic comparison of (A) inclination, (B) declination and (C) relative paleointensity (RPI) from sediment cores 02PC (this study) and HU2008-42 (St-Onge and St-Onge, 2014) and the CALS10k.1b geomagnetic field model (Korte et al., 2011). The blue triangle represents one radiocarbon age determined in this study and used in the age model.	55
Fig. 10. Composite age model using ^{210}Pb , ^{14}C ages (Table 3) and paleomagnetic tie points (Table 3). The Bayesian age-depth model was constructed using the R package BACON (Blaauw and Christen, 2011). The red dashed line shows the best age model and the gray shading represents the chronological uncertainties (95% confidence interval). Note that the first 80 cm and the basal layer of the core were not reliable for paleomagnetic reconstructions. Due to the lack of dateable material, ages below 10.5 cal ka BP were extrapolated assuming a constant sedimentation rate.	56

Fig. 11. $\delta^{13}\text{C}_{\text{org}}$ vs. $\delta^{15}\text{N}_{\text{total}}$ for cores 02PC and 27BC. Additional data: C3-land plant and marine plankton EM from(Peterson and Howarth (1987) and mean terrestrial OM from(Fogel and Cifuentes (1993).....	58
Fig. 12. EMMA performed on the grain-size distribution of the detrital fraction and EM scores (%) derived from EMMA for cores (A) 27BC and (B) 02PC.....	60
Fig. 13. Examples of X-radiographs and high-resolution photographs of different units identified in core 02PC. (A) Unit 1: laminated clayey silt; (B) Unit 2: IRD2 interval with Cal+Dol coarse silt layer; (C) Unit 2: IRD3 interval with Pl+Kfs coarse silt layer; and (D) Unit 3: homogenous clayey silt.....	61
Fig. 14. Downcore variations in core (A) 27BC and (B) 02PC, showing X-CT image, HRI, heat map of grain-size data, wet bulk density, magnetic susceptibility (k_{LF}), IRD counts (>2 mm fraction), a^* , TOC, $\delta^{13}\text{C}_{\text{org}}$ and $\delta^{15}\text{N}_{\text{total}}$. The gray box in (B) represents the IRD-rich intervals identified in core 02PC, and the red triangles represent dropstones. Lithofacies are displayed on the right side of the figure.	63
Fig. 15. Downcore variations of core (A) 27BC and (B) 02PC showing: X-ray computed tomography image (X-CT), high-resolution digital image (HRI), ratios of total feldspar/total clays (Pl+Kfs/clays), detrital carbonates/total clays (Cal+Dol/clays), Al/Ca, Ca/Fe and Zr/Al. The grey box represents the IRDs rich intervals in (B) identify in the core 02PC and the red triangles represent dropstones. Lithofacies are displayed on the right side of the figure.	66

- Fig. 16.** (A) Al_2O_3 - SiO_2 - CaO ternary plot showing the overall composition of the sediment from cores 27BC and 02PC and the average shale composition (Post-Archean average Australian Shale or PAAS;(Turekian and Wedepohl 1961). (B) Total feldspar (Pl+Kfs)-carbonates (Cal+Dol)-kaolinite+chlorite (Kln+Chl) based on the bulk mineralogy and the composition of the three sources of sediments discussed in this study.....68
- Fig. 17.** (A) Summer temperature reconstruction from the Agassiz Ice Cap (Lecavalier et al., 2017), (B) summer insolation at 60°N (W/m^2 , Laskar et al., 2004), (C) RSL reconstruction from Cape Hardy (Devon Island; Dyke, 1998), (D) SST (Ledu et al., 2010), (E) *Cassidulina reniforme* percentages from core 2001LSSL-014 collected in Smith Sound (Jennings et al. 2019); from core 02PC: (F) very coarse silt content, (G) IRD counts of >2 mm clasts from X-CT radiographs, (H) $k_{\text{ARM}}/k_{\text{LF}}$ ratio (magnetic grain-size indicator), and proportion of sediment from the (I) Canadian Shield, (J) detrital carbonates, and (K) weathered bedrock for core 02PC. Note that ages below 12 cal ka BP were extrapolated, and thus, our interpretations remain hypothetical.....78
- Fig. 18.** (A-B) Winter and summer insolation at 60°N (W/m^2 , Laskar et al., 2004), (C-D) proportion of sediments from the Canadian Shield and Paleozoic carbonates, (E) GS-EM3, (F) IRD counts of >2 mm clasts from X-CT radiographs, (G) SST and primary production (Cormier et al., 2016), and (H) reconstructed Arctic surface air temperature (SAT) anomalies (Kaufman et al., 2009).....79

Fig. 19. Schematic map showing the evolution of the sedimentary dynamics in the Jones Sound basin since the last deglaciation. (A) During the last glaciation, at approximately 13.5 cal ka BP, the sediment dynamics were mainly controlled by subglacial outwashes bringing fine-grained sediments (GS-EM1) rich in Kln+Chl, Al and terrestrial OM. An ice shelf could have been present at the entrance of the Jones Sound during this time. (B) Ice margin retreat started at approximately 12 cal ka BP with an increase in iceberg delivery in Jones Sound (IRD1), an increase in Zr/Al- and Pl+Kfs-rich sediments and an increase in the SR. (C) At 11 cal ka BP (IRD2), there is an increase in the Ca/Fe and Zr/Al ratios and Cal+Dol-rich sediments with an increase in the wet bulk density, k_{ARM}/k_{LF} and a predominant marine origin for the OM. These results suggest that sediments originated mainly from the deglaciation of the western Devon and southwestern Ellesmere Island margins and that more distal glaciomarine conditions were established in Belcher Inlet during this time. (D) The Belcher Glacier retreated to the present coastline at ~10 cal ka BP (Dyke 1999; Dyke and Evans, 2003) and promoted a large Pl+Kfs-rich IRD input (IRD3) to the Belcher Inlet. The decrease in the IRD input recorded at approximately 9.7 cal ka BP supports the idea (e.g., Dalton et al, 2020) that deglaciation in the Jones Sound sector ended at this time. (E) During the early mid-Holocene, the proportion of sediment derived from detrital Cal+Dol-rich sources dominate relative to Pl+Kfs-rich sources, suggesting that sediment dynamics continued to be impacted by the progressive inland ice retreat in the southwestern Ellesmere Islands, and that Belcher Glacier was probably reduced in size during this time. (F) During the late Holocene, detrital

sediment supply rich in Al/Ca and Pl+Kfs in the Belcher Inlet was largely dominated by meltwater plumes and ice rafting from the Belcher Glacier. The West Greenland Current (WGC) and Baffin Island Current (BIC) are represented by red and blue arrows, respectively. The size of arrows represents the strength/intensity of the ocean currents. The reconstruction of ice sheet extents is adapted from Dalton et al. (2020).....81

Fig. S7. Full vector paleomagnetic comparison of (A) inclination, (B) declination and (C) relative paleointensity (RPI) in sediment core 02PC and the CALS10k.1b geomagnetic field model (Korte et al., 2011). The blue triangle represents one radiocarbon age determined in this study and used in the age model.....94

LISTE DES ABRÉVIATIONS, DES SIGLES ET DES ACRONYMES

AMOC	<i>Atlantic Meridional Overturning Circulation</i> , circulation mérienne de retournement de l'Atlantique.
BIC	<i>Baffin island current</i> , Courant de l'île de Baffin.
CAA	<i>Canadian Arctic Archipelago</i> , Archipel arctique canadien.
CCGS	<i>Coastal Canadian Guard Ship</i> , navire de la Garde-Côtière canadienne.
C_{tot}	<i>Total carbon</i> , carbone totale.
IIS	<i>Innuitian Ice Sheet</i> , Inlandsis innuitien.
IRD	<i>Ice Rafted Debris</i> , vêlage d'icebergs.
IPCC	<i>Intergovernmental Panel on Climate Change</i> , comité intergouvernemental sur le changement climatique.
IRM	<i>Isothermal Remanent Magnetization</i> , aimantation isothermale rémanente.
ISMER	Institut des sciences de la mer de Rimouski.
GIS	<i>Greenland ice sheet</i> , calotte glaciaire du Groenland.
k_{LF}	<i>low field magnetic susceptibility</i> , susceptibilité magnétique mesurée à champ faible.
LGM	<i>Last Glacial Maximum</i> , Dernier maximum glaciaire.
LIA	<i>Little Ice Age</i> , petit âge glaciaire.
LIS	<i>Laurentide Ice Sheet</i> , Inlandsis laurentidien.
MDF_{NRM}	<i>Median Destructive Field of the Natural Remanent Magnetization</i> , champs destructif médian de l'aimantation naturelle rémanente.

MSCL	<i>Multi-Sensor Core Logger</i> , banc de mesure à senseurs multiples.
NGCC	<i>Navire de la Garde-Côtière canadienne</i> .
N_{tot}	<i>Total nitrogen</i> , azote total.
NRM	<i>Natural Remanent Magnetization</i> , aimantation naturelle rémanente.
OM	<i>Organic matter</i> , matière organique.
PCA	<i>Principal component analysis</i> , analyse en composantes principales.
SIRM	<i>Saturation Isothermal Remanent Magnetization</i> , aimantation rémanente isothermale de saturation.
UQAR	Université du Québec à Rimouski.
WGC	<i>West Greenland Current</i> , courant ouest groenlandais.
XCT	<i>X-ray Computed Tomographic</i> , radiographie à rayons X.
XRD	<i>X-Ray diffraction</i> , diffraction à rayon X.
XRF	<i>X-ray fluorescence</i> , fluorescence à rayons X

INTRODUCTION GÉNÉRALE

Contexte scientifique et problématique

Il y a de cela 100 ans, l'exploration de l'Arctique était une mission périlleuse. Différents explorateurs s'y sont aventurés avec des objectifs divers, allant de la découverte du passage du Nord-Ouest, à l'emplacement exact du pôle Nord ou encore pour reconnaître la souveraineté du Canada dans les îles de l'archipel Arctique (Neatby et Kikkert, 2016). Aujourd'hui, l'exploration de cet archipel a des buts bien différents. L'avènement des changements climatiques anthropiques, datant de la révolution industrielle, a alarmé beaucoup de scientifiques à cause du réchauffement planétaire qu'ils engendrent (IPCC, 2019). Les conséquences de ceux-ci se font sentir partout à travers le globe et leurs effets sont encore plus néfastes pour la région de l'Arctique (Serreze and Francis, 2006). En effet, les changements climatiques suscitent beaucoup de questionnements et d'inquiétudes concernant l'avenir de la glace et du niveau marin. Selon les différents modèles de simulation de climat, les régions polaires seraient celles qui se réchauffent le plus rapidement (IPCC, 2014, 2019) et ceci se traduit notamment par la fonte de la glace de mer, des glaciers et des calottes glaciaires. En effet, les taux d'accélération de fonte de la glace dans l'Archipel Arctique Canadien (AAC), au Groenland et dans certains glaciers du Svalbard ont augmenté drastiquement depuis la fin du 20^e siècle, suggérant ainsi une tendance générale de fonte de l'Arctique (Fisher et al., 2012).

L'AAC contient plusieurs petites calottes glaciaires et glaciers principalement concentrés sur les îles d'Ellesmere, de Devon, d'Axel Heiberg, de Meighen, faisant parties du regroupement d'îles de la Reine Élisabeth, et ainsi que sur les îles de Baffin et Bylot plus au sud (Noël et al., 2018). Les plus grandes calottes glaciaires de l'AAC sont la calotte glaciaire de Devon, sur l'île de Devon et la calotte glaciaire Agassiz sur l'île Ellesmere (Dowdeswell et al., 2004). Des études récentes indiquent que les glaciers et les calottes glaciaires de l'AAC ont connu une diminution en superficie au cours des deux dernières décennies (ex., Sharp et al., 2011). Cela a été en partie attribué à une augmentation de la décharge du vêlage d'icebergs provenant des glaciers aboutissant dans la mer (Van Wychen et al., 2016). À la fin du 21^e siècle, il est estimé que les glaciers de l'AAC pourraient perdre

18% de leur superficie, contribuant ainsi à une augmentation du niveau marin de $0,35 \pm 0,24$ mm/an et à une diminution de l'albédo planétaire (Shepherd et al. 2007; Marzeion et al. 2012; Noël et al. 2018). Cependant, très peu d'informations sont connues concernant les taux des décharges d'icebergs et les flux de sédiments glaciaires à long terme (>50 ans) des glaciers dans la l'AAC ainsi que sur les mécanismes précis qui contrôlent les changements frontaux de ces glaciers (Cook et al., 2019). Dans un contexte de réchauffement climatique, les enregistrements sédimentaires sont donc essentiels pour documenter la sensibilité des glaciers et des calottes glaciaires aux variations climatiques et océanographiques du Quaternaire récent, et donc de mieux comprendre les mécanismes actuels qui induisent ces changements (ex., Briner et al., 2009; Hodson et al., 2012).

Les glaciers et les calottes glaciaires situés au sud-est des îles de la Reine Élisabeth se trouvent dans la polynie des eaux du Nord (NOW pour North Water Polynya), situé dans l'axe d'un corridor océanographique majeur pour l'exportation d'eau douce arctique dans le nord de la baie de Baffin. La NOW est la polynie la plus importante dans l'Arctique canadien avec une superficie de $80\,000\text{ km}^2$ d'eau libre en été (Dunbar et Dunbar 1972; Stirling 1980; Steffen et Ohmura 1985; Lyn Lewis et al., 1996). Celle-ci est formée grâce à la combinaison de plusieurs phénomènes. Durant l'hiver, la glace dérive vers le sud par les courants polaires du bassin de Kane causant un barrage de glace dans le détroit de Smith (Stirling, 1980). Au sud de ce barrage, la glace est emportée par les courants et par les vents dominants du nord laissant une eau complètement libre de glace même en hiver (Stirling, 1980). Cette polynie est aussi reconnue pour ses taux de sédimentation élevés et sa grande productivité biologique (Knudsen et al., 2008). Autour de 25% de l'exportation des eaux froides arctiques transitent par cette polynie jusqu'aux eaux de l'Atlantique Nord par le biais des détroits de Lancaster, de Smith, et de Jones (ex., Tang et al., 2004). Ainsi, des variations dans l'apport de ces eaux, principalement avec la fonte de la glace de mer et des glaciers, peuvent avoir un impact sur la circulation méridienne de retournement de l'Atlantique (AMOC pour Atlantic Meridional Overturning Circulation; Curry et Mauritzen 2005, Serreze et al., 2006) et sur la formation d'eau profonde dans la mer du Labrador (Belkin et al., 1998).

Pendant le dernier maximum glaciaire (LGM pour Last Glacial Maximum; ~20 cal ka BP), la confluence des Inlandsis laurentidien (LIS pour Laurentide Ice Sheet), innuitien (IIS pour Innuitian Ice Sheet) et groenlandais (GIS pour Greenland Ice Sheet) a complètement bloqué les détroits de l'AAC (ex., Dyke et al., 2002; England et al., 2006; Jennings et al., 2011, 2019) empêchant donc l'écoulement vers le sud des eaux froides et peu salées de l'Arctique dans la baie de Baffin (Fig. 3). Plusieurs études glaciologiques, sédimentologiques et paléocéanographiques dans l'AAC ont documenté les phases de retraits glaciaires et d'ouvertures des principaux détroits qui relient les océans Arctique et Atlantique Nord dans la région Nord-Est du Canada/Nord-Ouest du Groenland pendant la déglaciation (ex., Dyke et al., 1998; England et al., 2006; Jennings et al., 2011; Georgiadis et al., 2018; Caron et al., 2019). Cependant, l'impact de l'ouverture du détroit de Jones et de l'établissement du flux arctique-atlantique sur la dynamique des glaciers et l'environnement marin dans le bassin de Jones ont été très peu documentés par des séquences sédimentaires marines. Or, cette information pourrait donner des pistes pour améliorer notre compréhension sur le développement paléocéanographique de la baie de Baffin ainsi que sur la variabilité naturelle des glaciers situés au sud-est des îles de la Reine Élisabeth dans le contexte du réchauffement climatique.

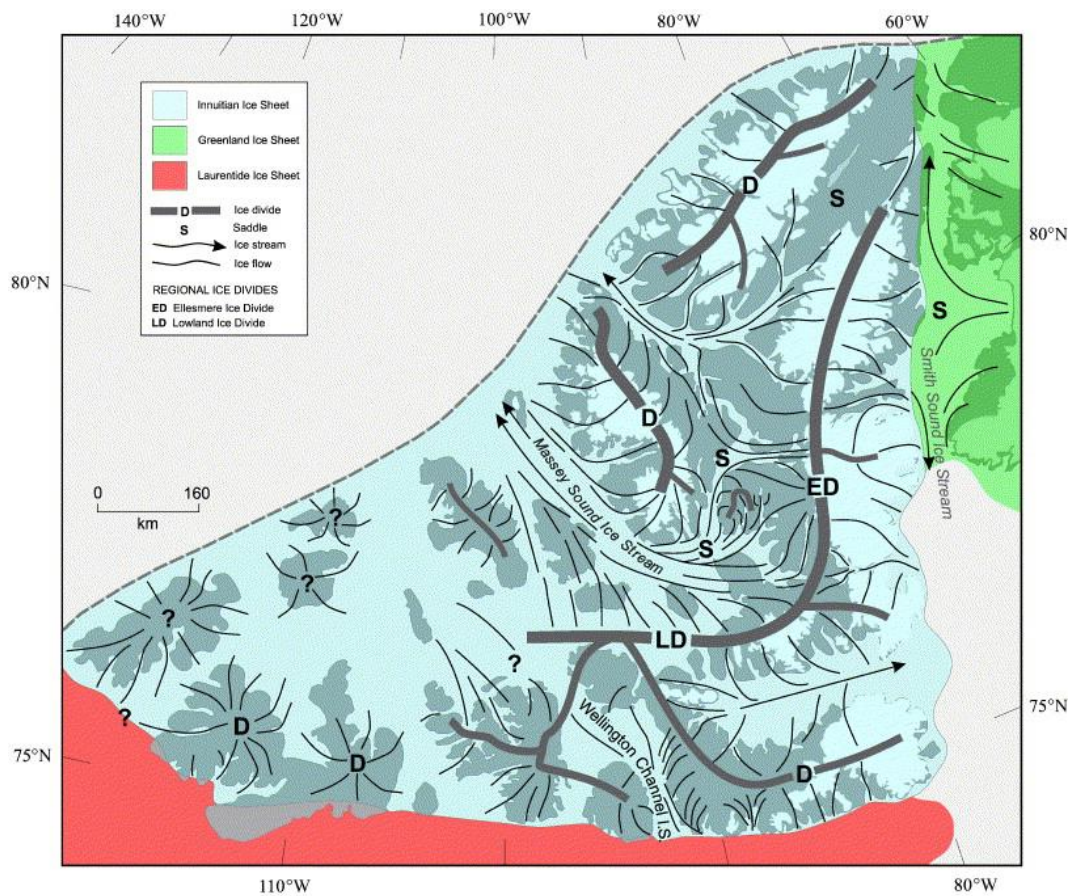


Fig. 1. Carte schématique (England et al., 2006) de la dernière glaciation. Le bleu représente l'Inlandsis innuitien, le vert l'ouest de l'Inlandsis groenlandais et en rouge, le nord de l'Inlandsis laurentidien.

Objectifs de recherche et approche méthodologique

Dans le cadre de ce projet de maîtrise, les événements et les processus sédimentaires survenus pendant l'ouverture du détroit de Jones ainsi que la dynamique sédimentaire du glacier de Belcher depuis la déglaciation ont été étudiés en utilisant des analyses sédimentologiques, minéralogiques, géochimiques (élémentaires et isotopiques) et magnétiques de deux séquences sédimentaires (AMD0217-27BC; 43 cm, AMD0217-02PC; 705 cm). Celles-ci ont été récoltées près du glacier Belcher, soit le principal glacier de décharge de la calotte glaciaire de Devon, située sur l'île du même nom et du côté nord-ouest de la baie de Baffin (Fig. 3).

Les carottes sédimentaires ont été récoltées à bord du brise-glace de la Garde côtière canadienne (NGCC) Amundsen lors de la mission ArcticNet de 2017 (Leg 2b; Montero-Serrano et al., 2017). Les sites d'échantillonnage ont été choisis en utilisant des profils sismiques et des profils multifaisceaux (Fig. 2). Le sous-échantillonnage des sédiments a été réalisé selon un intervalle de 1 cm pour la carotte à boîte et à tous les 8 cm pour la carotte à piston. La chronologie des carottes a été établie avec des données de ^{210}Pb pour la carotte à boîte et avec des mesures paléomagnétiques ainsi que des âges ^{14}C pour la carotte à piston. Les carottes ont été passées au *X-ray Computed Tomography* (X-CT) et au *Multi Sensor Core Logger* (MSCL) de GEOTEK pour la mesure des propriétés physiques (densité, susceptibilité magnétique, couleurs). Les analyses granulométriques ont été réalisées à l'aide d'un analyseur de taille des particules *Beckman Coulter LS13320* et la distribution granulométrique et les paramètres statistiques ont été calculés à l'aide du logiciel *GRADISTAT* (Blott and Pye 2001). Les analyses magnétiques ont été effectuées à l'aide d'un magnétomètre à gradient alternatif (AGM; *MicroMag 2900*) et à l'aide d'un magnétomètre cryogénique. La composition minéralogique des échantillons a été étudiée par diffraction de rayon X (DRX, Eberl 2003) et le programme Excel SedUnMixMC (Andrews and Eberl 2012) a été utilisé pour quantifier les changements de provenance des apports détritiques. La composition chimique a été déterminée sur des pastilles de verre par la méthode de spectrométrie de fluorescence à rayon X à dispersion d'énergie (FRX-DE) en utilisant un spectromètre *PANalytical Epsilon 3-XL* (Gamboa et al. 2017). Finalement, les proportions (%) et les analyses isotopiques du carbone et de l'azote ($\delta^{13}\text{C}_{\text{org}}$ et $\delta^{15}\text{N}_{\text{total}}$) ont été mesurées à l'aide d'un analyseur élémentaire *COSTECH ECS 4010* couplé avec un spectromètre de masse à rapport isotopique (*IRMS*) *delta XP*. L'ensemble des données sera archivé dans le système de gestion des données PANGAEA (<https://www.pangaea.de/>).

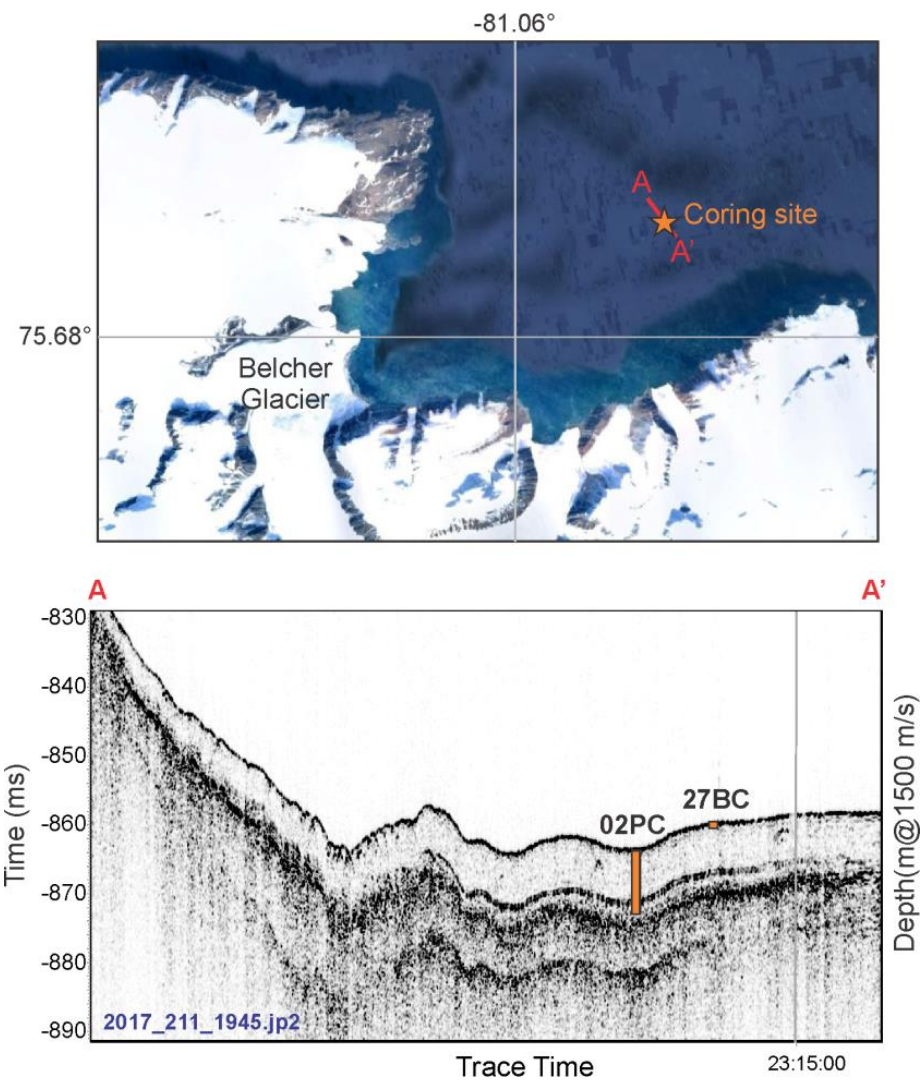


Fig. 2. Profil sismique (3,5 kHz) avec la localisation des carottes à boîte (27BC) et à piston (02PC) étudiés dans le cadre de ce projet de maîtrise.

Présentation de la zone d'étude

La calotte glaciaire du Devon, sur l'île de Devon, fait partie du regroupement d'îles de la Reine Élizabeth dans l'AAC (Fig. 3). La perte de masse de glace dans cette région est passée de $31 \pm 8 \text{ Gt.an}^{-1}$ entre 2004 et 2006, à $92 \pm 12 \text{ Gt.an}^{-1}$ entre 2007 à 2009, mais très peu d'informations sont connues concernant la dynamique sédimentaire des glaciers individuels dans ces îles. La calotte glaciaire de Devon a une superficie de $14\,000 \text{ km}^2$ et est donc une des plus grandes calottes glaciaires de l'AAC avec un volume de glace de 411

$\pm 140 \text{ km}^3$ (Shepherd et al., 2007). Des études récentes ont démontré que la calotte glaciaire de Devon aurait perdu 600 km^2 (4%) de sa superficie entre les années 1960 et 1999 principalement à cause des plus hautes températures durant l'été, augmentant ainsi la fonte de la glace (Burgess et Sharp 2004; Mair 2005). De plus, la modélisation du bilan de masse de la calotte glaciaire de Devon a démontré que dans les prochaines décennies le bilan de masse de la calotte va diminuer de $2.2 \pm 0.7 \text{ Gt.an}^{-1}$, une perte suffisante pour faire augmenter le niveau marin de manière significative (0.006 mm/an; Shepherd et al., 2007).

À l'Est de la calotte glaciaire de Devon se trouve le glacier Belcher, soit le principal glacier de décharge. À lui seul, il contribue à plus de 42% de la décharge totale d'icebergs de la calotte glaciaire (Van Wychen et al., 2012). La connexion avec la mer de la plupart des glaciers qui drainent la calotte glaciaire de Devon fait en sorte que ceux-ci sont vulnérables face aux changements climatiques et océanographiques (Burgess and Sharp 2004). De plus, les plus hautes vitesses d'écoulement des glaciers de l'île de Devon ont été observées aux glaciers Belcher et Fitzroy, suggérant une plus forte activité en lien avec le réchauffement climatique (Burgess and Sharp 2004; Van Wychen et al., 2017). L'étude de la dynamique sédimentaire du glacier Belcher va donc permettre de mieux documenter la dynamique sédimentaire de l'Est de l'île de Devon depuis la dernière déglaciation.

Circulation océanique

L'Île de Devon est encerclée par trois détroits, tous connectés avec le nord de la baie de Baffin: le détroit de Lancaster, le détroit de Jones et le détroit de Smith (Fig. 3). La baie de Baffin et la calotte glaciaire de Devon sont influencées par deux courants principaux, soit le courant de l'Île de Baffin et le courant ouest groenlandais. Le courant de l'Île de Baffin est originaire des eaux froides (température $> -1^\circ\text{C}$; Zweng et Münchow, 2006) et douces de l'Arctique et s'écoule vers le Sud, longeant la partie Ouest de la baie de Baffin (Tang et al., 2004). De l'autre côté, le courant ouest groenlandais s'écoule vers le Nord et longe le côté ouest du Groenland avant de se mélanger avec le courant de l'île de Baffin dans le détroit de Smith (Tang et al., 2004). Le courant Ouest groenlandais est un mélange d'eaux froides et de faible salinité provenant de l'Est du Groenland et des eaux chaudes et

salées provenant du courant Irminger. Ceci fait en sorte que le courant ouest groenlandais est relativement chaud et salé comparativement au courant de l'île de Baffin, qui est froid et moins salé (température $> 2^{\circ}\text{C}$; Zweng and Münchow, 2006). Une augmentation de température d'un de ces courants pourrait contribuer à l'augmentation de la perte de masse des calottes glaciaires (Holland et al., 2008). La partie Nord de l'Île de Devon est bordée par le détroit de Jones. Deux courants principaux caractérisent ce détroit; un courant de surface avec des eaux d'origine pacifique passant par le détroit de Cardigan, qui est constitué d'un seuil peu profond (150 m, $S < 33.5$) et un courant profond d'origine atlantique, similaire aux eaux circulant dans le détroit de Smith (Jones et al., 2003). Le détroit de Jones est caractérisé par un bassin profond de 850 m de profondeur (Harrison et al., 2011)

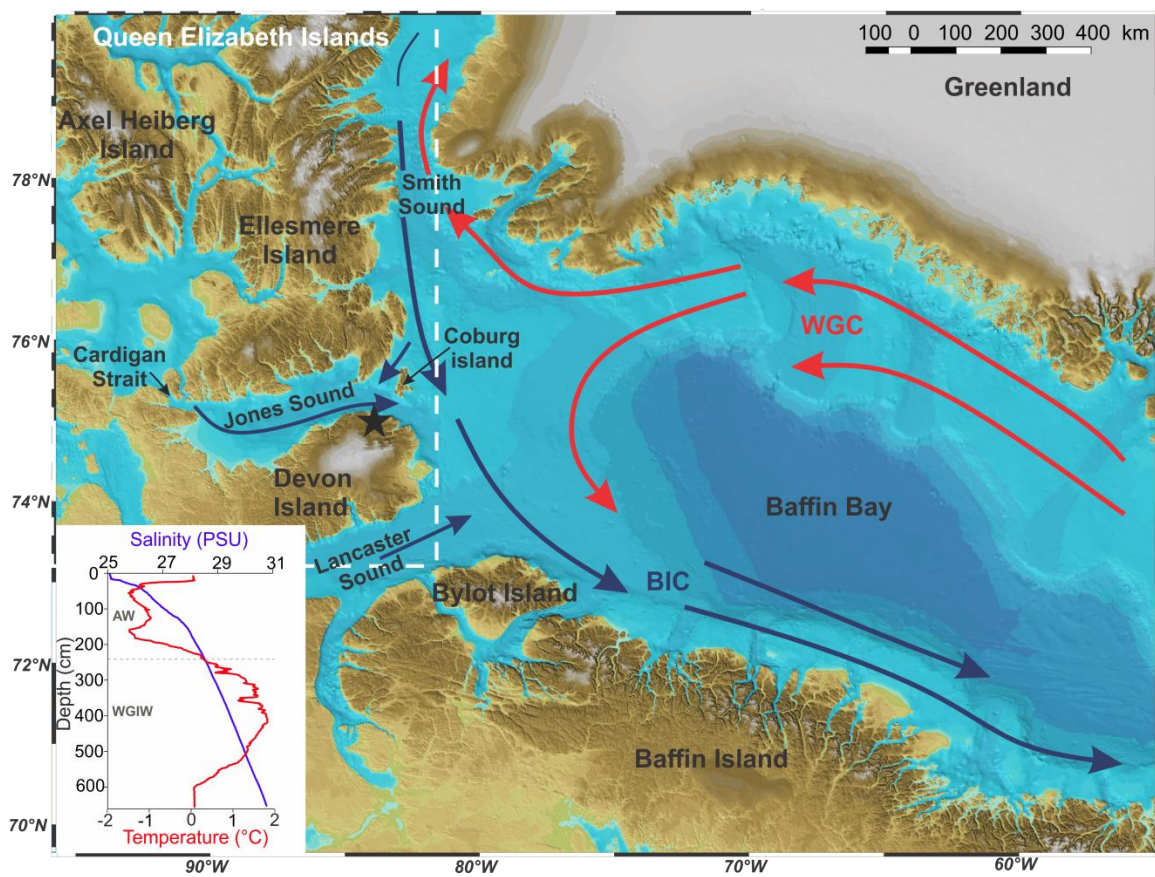


Fig. 3. Emplacement des deux carottes de sédiments AMD1702-27BC et AMD1702-02PC (étoile noire) et profil de température et salinité (AW : Arctic Water et WGIW; West Greenland Intermediate Water) mesurée à la même position que les carottes (Amundsen science data). La circulation océanique est représentée par les flèches rouges et bleues. Les flèches rouges représentent le courant ouest groenlandais (WGC), tandis que les flèches bleues représentent le courant de l'île de Baffin (BIC).

Sédimentation et géologie

La baie de Baffin est caractérisée par un grand apport de sédiments provenant d'une multitude de chenaux glaciaires issus des calottes du Groenland et de l'ancienne calotte Innuitienne et de l'Inlandsis laurentidien (Fig. 2; Dyke et al., 2002). Toutefois, ces sédiments peuvent aussi provenir de différents agents de transport tels que la glace de mer, les rivières, les eaux de fontes ainsi que les plumes turbides de sédiments (Andrews and

Eberl, 2012). La sédimentation moderne dans la baie de Baffin peut être influencée par des débris délestés par des icebergs (IRD) et par le transport des sédiments en suspension par les plumes d'eau de fonte dans les fjords provenant des glaciers (Fig. 4; Andrews and Syvitski, 1994). Aujourd'hui, la sédimentation dans le détroit de Jones est principalement contrôlée par les glaciers, par les rivières continentales et par le transport par la glace (Harrison et al., 2011).

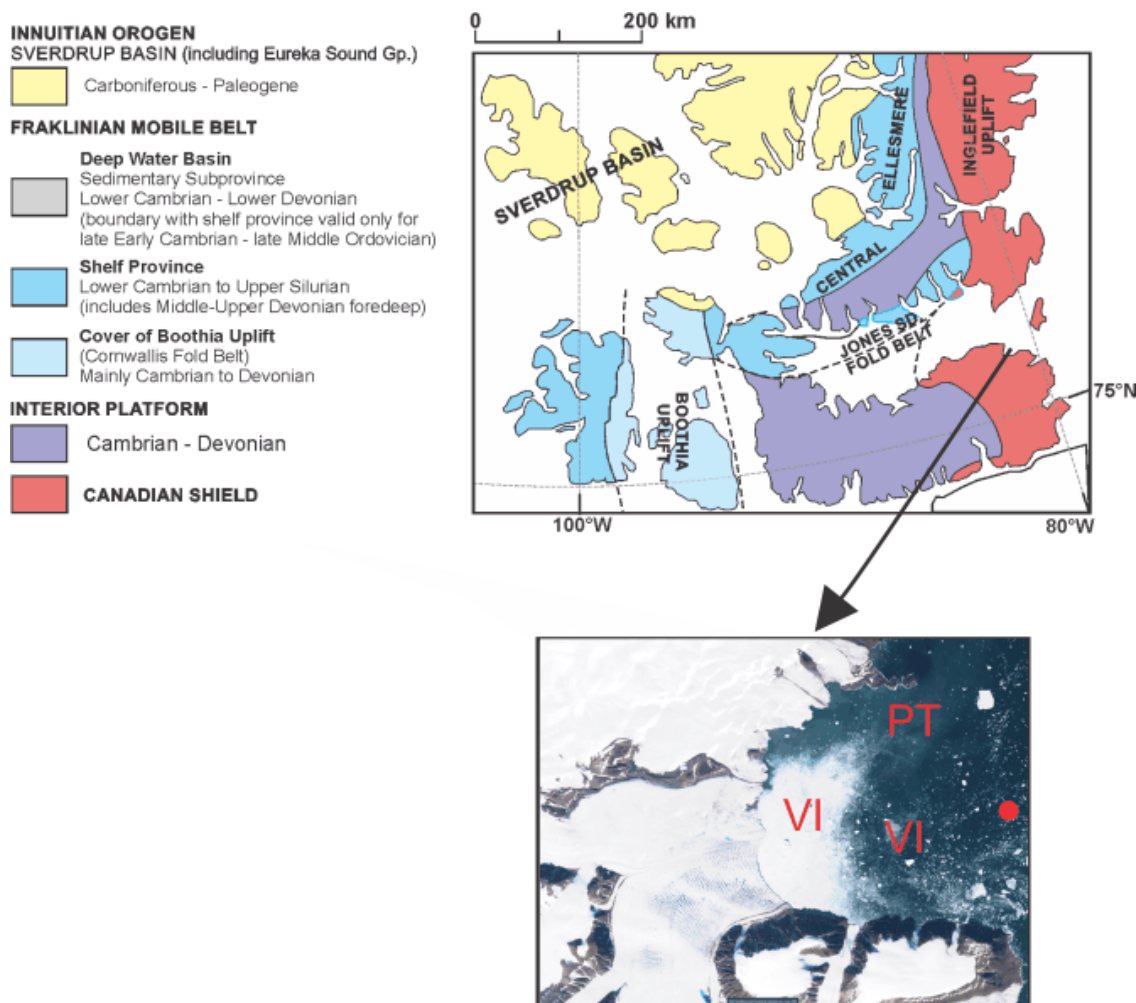


Fig. 4. Carte géologique simplifiée du bassin de Jones (adaptée de Zhang et al., 2016) et une image sentinelle du glacier Belcher, avec la localisation du carottage (point rouge), le vêlage d'icebergs (VI) et les plumes turbides de sédiments (PT).

Le socle rocheux de l'île de Devon est divisé en deux lithologies différentes. Les parties Ouest et centrale de l'île sont composées principalement de roches sédimentaires telles du grès, du shale et du gypse, toutes riches en carbonates détritiques datant du Paléozoïque (Thorsteinsson and Mayr, 1987). De l'autre côté, la partie Est est composée de roches précambrrientes du Bouclier Canadien, soit principalement du gneiss et du granite. Le glacier Belcher, étant dans la partie Est, repose sur un socle de roches métasédimentaires riches en veines de granite (Frisch, 1988). Dans le bassin de Jones, le socle rocheux est recouvert par une couche plate et non uniforme de sédiments datant du Quaternaire (Harisson et al., 2011). Le bassin est aussi affecté par une série de failles normales qui influencent les strates sédimentaires qui reposent par-dessus (Keen et Barrett, 1973). Ces sédiments sont tronqués à l'entrée du détroit par un socle rocheux plus élevé près de l'île Coburg (Keen et Barrett, 1973). La baie de Baffin, quant à elle, est aussi largement dominée par des roches cristallines précambrrientes superposées par des carbonates du Paléozoïque issus de l'érosion glaciaire (Simon et al., 2014). Durant le Pléistocène, le socle rocheux a été impacté successivement par l'Inlandsis laurentidien en transportant du matériel érodé à travers l'Arctique canadien. Ces couches riches en carbonates détritiques (principalement de la dolomite) sont attribuées aux courants glaciaires du Nord-Est de l'Inlandsis laurentidien ainsi qu'à l'Inlandsis innuitien, ou encore par des débâcles d'icebergs riches en débris (Simon et al., 2014).

HOLOCENE SEDIMENTARY DYNAMICS IN JONES SOUND AS RECORDED IN SEDIMENT CORES FROM BELCHER INLET (DEVON ICE CAP, NUNAVUT, CANADA)

Jade Brossard^{1,2,3}, Jean-Carlos Montero-Serrano^{1,3}, Guillaume St-Onge^{2,3}

¹Institut des sciences de la mer de Rimouski, Université du Québec à Rimouski, Rimouski, Québec, Canada.

²Canada Research Chair in Marine Geology, Institut des sciences de la mer de Rimouski, Université du Québec à Rimouski, Rimouski, Québec, Canada.

³GEOTOP Research Center, Montréal, Québec, Canada.

1. INTRODUCTION

The Canadian Arctic Archipelago (CAA) contains many small ice caps and glaciers located mainly on Ellesmere, Devon, Axel Heiberg, Meighen, with more in the south on Baffin and Bylot Islands (Noël et al., 2018). The largest ice caps in the Canadian Arctic are the Devon Ice Cap on Devon Island and the Agassiz Ice Cap on Ellesmere Island (Dowdeswell et al., 2004). With the rising impact of climate change, glaciers in the CAA could lose 18% of their surface area by the end of the 21st century, thus contributing an increase of 0.35 ± 0.24 mm/year to global sea-level rise and diminishing albedo (Shepherd et al., 2007; Marzeion et al., 2012; Noël et al., 2018). Sea-level rise will also impact humanity, as ice sheets will continue to respond to anthropogenic climate perturbations for hundreds or even thousands of years (Clark et al., 2016). However, recent changes in the extent of the ice masses in the CAA and uncertainties caused by the contribution of outlet glaciers are not well known (Burgess and Sharp 2004; Andresen et al., 2013). Moreover, the Canadian Arctic contains more than 300 marine-terminating glaciers, but very few studies have investigated changes in their frontal positions in response to changes in the ocean-climate system (Cook et al., 2019).

The Devon Ice Cap is on Devon Island in Nunavut, Canada (Fig. 6) and has an area of 14 000 km² with a significant volume of land based ice (411 ± 140 km³; Shepherd et al., 2007). Recent studies have revealed that this ice cap lost 4% (~600 km²) of its area between 1960 and 1999 because higher summer air temperatures have increased surface melt and runoff (Burgess and Sharp 2004; Mair 2005). Instrumental data predict that over the next decades, the ice sheet mass balance will decrease by 2.2 ± 0.7 Gt yr⁻¹, which is sufficient to raise the sea level by 0.006 mm yr⁻¹ (Shepherd et al., 2007). The Belcher Glacier, a tide water glacier, is the largest contributor to the overall mass flux of the Devon Ice Cap, with 42% (0.17 ± 0.03 Gt yr⁻¹) of total iceberg discharge (Van Wychen et al., 2012). While major tide-water glaciers along the east coast of Devon Island have already retreated up to 1.3 km in the last 40 years, the highest velocities (~300 m yr⁻¹) occur at the Belcher and Fitzroy Glaciers' termini (Burgess and Sharp 2004; Van Wychen et al., 2017). Between 2009 and 2015, the Belcher Glacier underwent a progressive speedup driven by terminus thinning, which facilitated faster ice flow (Van Wychen et al., 2017). Therefore, studying the long-term (> 50 years) Belcher Glacier dynamics will help us to better understand the dynamics of the Devon Ice Cap and the impact of future climate change on the CAA.

In this context, this study focuses on the sedimentological, mineralogical, geochemical (elemental and isotopic), and magnetic properties of two sediment cores (AMD1702-27BC-A and AMD1702-02PC; hereafter referred to as 27BC and 02PC, respectively) sampled in the Belcher Inlet to document changes in the sediment dynamics in Jones Sound and Belcher Inlet related to climate variability since the last deglaciation. Studying sedimentary sequences makes it possible to document the glacier's sensitivity to late Quaternary climatic variations and, therefore, to better understand the modern mechanisms that induce these changes (e.g., Briner et al., 2016).

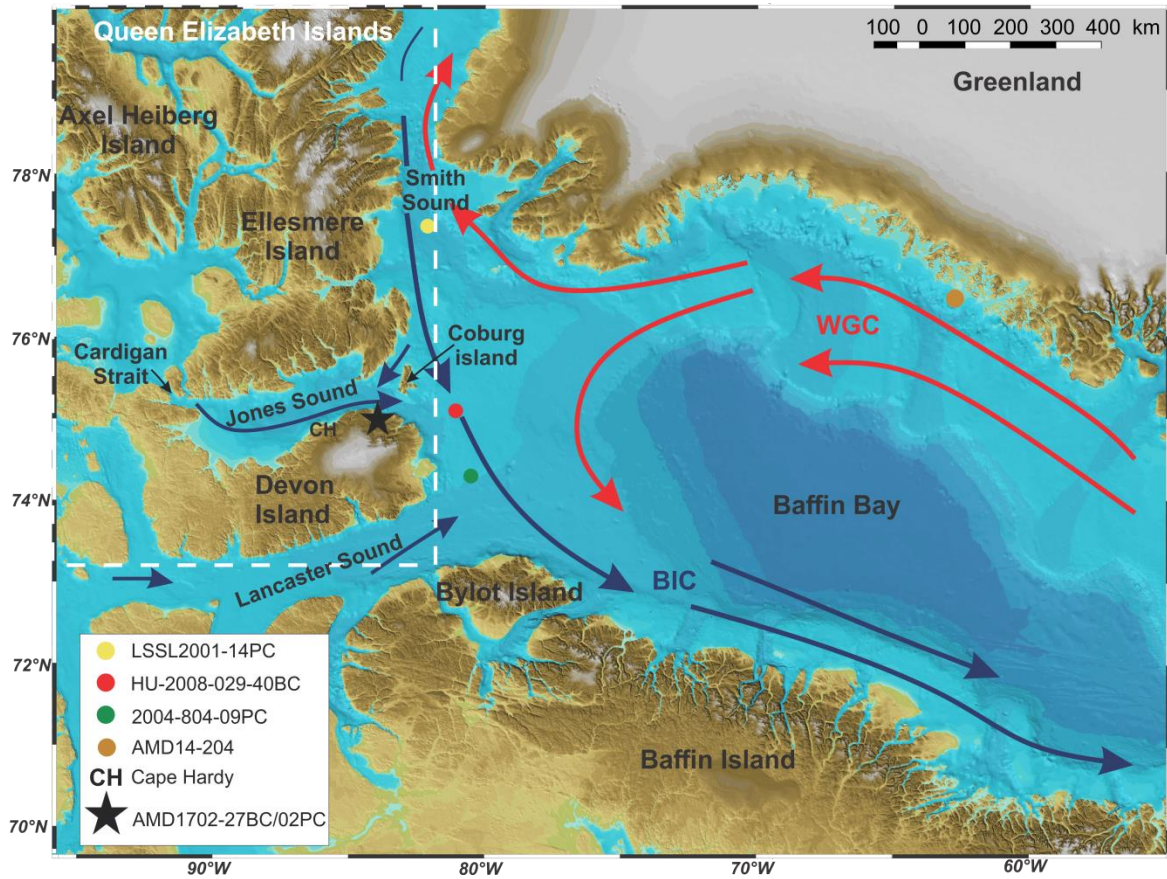


Fig. 5. Location of cores 27BC and 02PC (black star). The oceanic circulation is represented by red and blue arrows. Red arrows illustrate the West Greenland Current (WGC), a warm and salty current, while blue arrows represent the Baffin Island Current (BIC), a cold Arctic current. Red, green and yellow circles denote sediment cores mentioned in the text.

2. REGIONAL SETTING

2.1. Oceanic circulation

Devon Island is bounded by: Lancaster and Jones Sounds that connect with the Arctic Ocean. These channels have shallow depths, thus limiting the amount of water that enters Baffin Bay from the Arctic Ocean and making Baffin Bay a pathway for freshwater and sea ice (Tang et al., 2004). The Devon Ice Cap is influenced by two main currents, the Baffin

Island Current (BIC) and the West Greenland Current (WGC). While the BIC flows southward in the western part of Baffin Bay and originates from cold Arctic waters, the WGC flows northward along the western coast of Greenland before mixing with the BIC in Smith Sound (Fig. 5; Tang et al., 2004). The WGC is a mixture of the cold low-salinity waters from the East Greenland Current and the warm and salty Irminger Current, making the WGC relatively warm and salty compared to the BIC. Therefore, enhanced northward inflow of the WGC can influence the frontal ablation of marine-terminating glaciers in the western Greenland margin and north of Baffin Bay (e.g., Motyka et al., 2011; Caron et al., 2018). On the other hand, the opening of the Nares Strait during the early Holocene (9.0–8.3 cal ka BP; Caron et al., 2018; Georgiadis et al., 2018; Jennings et al., 2019) connected the Arctic and North Atlantic Oceans in Baffin Bay and allowed the development of modern ocean circulation in the bay (e.g., Georgiadis et al., 2018; Jennings et al., 2019). The eastern part of Devon Island is adjacent to the North Water Polynya, which is the largest polynya in the Canadian Arctic with 80 000 km² of open water in summer (Dunbar and Dunbar, 1972; Stirling, 1980; Steffen and Ohmura, 1985; Lyn Lewis et al., 1996). During the winter, pack ice being carried south through Kane Basin by currents from the polar basin becomes congested and forms an impassable ice dam in Smith Sound (Stirling, 1980). New ice formed to the south of the ice dam is swept away by the southward flowing current, aided by northerly winds, leaving open water behind it throughout the winter (Stirling, 1980). This Polynya is an area of high biological productivity (Knudsen et al., 2008). The sedimentation rates (SR) vary between 0.04 cm yr⁻¹ and 0.17 cm yr⁻¹, which is very high compared to SR in the subpolar region (Bailey et al., 2013; Cormier et al., 2016; Rochon and de Vernal, 1994; St-Onge and St-Onge, 2014). The northern part of the Devon Island faces Jones Sound. In eastern Jones Sound, the upper waters come mostly from the Pacific and are similar to those flowing in the Nares Strait (Jones et al., 2003). The water flowing into Jones Sound passes through the Cardigan Strait, a shallow sill, which excludes anything other than Pacific water flowing through the channel (Jones et al., 2003).

2.2. Surrounding geology and sedimentation in Jones Sound

Jones Sound is a 300 km long and 55 to 75 km wide basin characterized by a deep axial trough with water depths mainly between 500 and 850 m (MacLean et al., 1984; Harrison et al., 2011). Gravity and seismic data from this basin reveal that the bedrock is composed of Cretaceous to Neogene sedimentary rocks overlain by flat-lying Quaternary sediments (Keen and Barrett, 1973; Maclean et al., 1984; Harrison et al., 2011). Rocks outcropping on western Devon and southwestern Ellesmere Islands are mainly composed of Paleozoic carbonates, sandstone, and shale, which are part of the Franklinian mobile belt (Fig. 2; Thorsteinsson and Mayr 1987). Precambrian rocks (gneiss and granite) from the Canada-Greenland shield (Inglefield mobile belt) outcrop in eastern Devon Island and southeastern Ellesmere Islands (Fig. 6).

Few studies provide a general view of the SR within the Jones Sound basin (Williams, 1990). However, one shell date (2.6 ± 0.1 ka BP) obtained at 240 cm in a sediment core collected in the central part of the basin (HU83-023-053; Williams, 1990) allows us to estimate that SR were approximately ~ 0.11 cm yr $^{-1}$ in the late Holocene. This estimate of SR is in agreement with sedimentological and paleoceanographic studies performed in the eastern side of the basin and North Water Polynya area (e.g., Rochon and deVernal, 1994; Mudie et al., 2006; Bailey et al., 2013; St-Onge and St-Onge, 2014; Cormier et al., 2016), where the deglacial and Holocene SR range from 46 to 0.19 cm yr $^{-1}$. The surficial seabed sediments in Jones Sound are mainly composed of sand and gravels nearshore and finer grained (olive-grey silty clay) sediments off shore in the central part of the basin (Perry, 1961). These sediments are mainly derived from glacial erosion by the glaciers (including land-terminating and tidewater glaciers) on Devon and southwestern Ellesmere Islands (Maclean et al., 1984). Various sedimentary processes, such as ice rafting debris (IRD), glaciogenic debris flows, meltwater plumes, and turbidity currents, influence sedimentation in this glaciated environment (e.g., Andrews et al., 2014, 2018; Hiscott et al., 1989; Marlowe, 1966; Cofaigh et al., 2003; Simon et al., 2014; Caron et al., 2020; Lévesque et al., 2020). During deglaciation and the early Holocene, sediment inputs to the

Jones Sound basin were controlled by the retreat of the Innuitian Ice Sheet (IIS; e.g., England et al., 2006; Dalton et al., 2020).

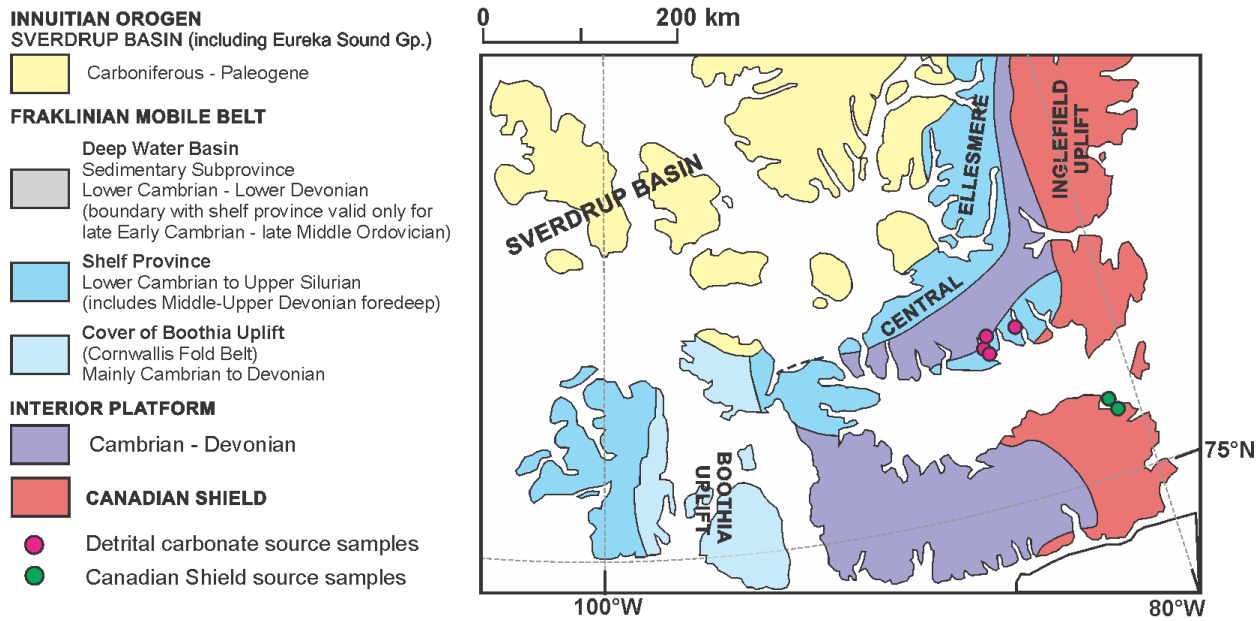


Fig. 6. Bedrock geology of Jones Sound (adapted from Trettin, 1991 and Zhang et al., 2016) showing the location of the sediment source samples discussed in this study.

3. MATERIALS AND METHODS

3.1. Coring and sampling

Box core 27BC and piston core 02PC (water depth: 626 m; location: 75°42.384'N, 80°45.593'W) were collected in the Belcher Inlet onboard the icebreaker Canadian Coast Guard Ship Amundsen during the 2017 ArcticNet expedition (Fig. 5). All coring sites were targeted using high-resolution seismic profiles that indicated high SR not influenced by mass wasting events (Montero-Serrano et al., 2017). Core 27BC is 43 cm long, whereas core 02PC is 705 cm long. Core 27BC was evenly sampled on 1-cm-wide section taken at 1 cm intervals (total of 43 samples), whereas core 02PC was sampled on 1-cm-wide section taken at 8 cm intervals with additional samples in the IRD section (total of 114 samples).

Table 1. Location, water depth and length of the two sediment cores used in this study.

Samples	Latitude (°N)	Longitude (°W)	Water depth (m)	Length (cm)
AMD1702-27BC	75°42.130'	80°45.122'	623	43
AMD1702-02PC	75°42.384'	80°45.593'	626	705

3.2. Multi-Sensor Core Logger analyses

The whole round sediment core sections were scanned using a GEOTEK X-ray computed tomography (X-CT) system. The digital X-ray images obtained by X-CT are useful to visualize the different facies and sedimentary structures, as well as changes in bulk density within the cores (St-Onge et al., 2007). Next, wet bulk density, low field volumetric magnetic susceptibility (k_{LF}), diffuse spectral reflectance and chemical composition by portable X-ray fluorescence (pXRF) were measured on sediment cores at 1 cm intervals using a GEOTEK Multi-Sensor Core Logger (MSCL). The reflectance was obtained by using a hand-held Minolta CM-2600d spectrophotometer online with the MSCL, and the sediment color is expressed according to the L*, a* and b* color space of the *International Commission on Illumination*. L* is black with a scale (0-100), a* is a green to red scale (-60 to +60) and b* is a blue to yellow scale (-60 to +60). The pXRF scans were made using an energy-dispersive Olympus Innov-X DELTA portable XRF analyzer equipped with a 40 kV rhodium anode X-ray tube. The pXRF analysis was conducted using the two-beam (40 and 10 kV) GeoChem mode at 60-second exposures per beam.

3.3. Grain-size distribution and end-member modeling analyses

Sediment grain-size analyses were performed with a Beckman Coulter LSI3320 laser diffraction grain-size analyzer, which has a detection range of 0.04–2000 μm . Prior to analysis, the sediment samples were pretreated with 10 mL of hydrogen peroxide (H_2O_2 ;

30% v/v) for at least 72 h to remove the organic matter. Carbonate was not removed from sediment samples, as erosion of Paleozoic sedimentary carbonate-bearing rock provides an important fraction of dolomite and calcite in the samples and thus informs on sedimentary processes. Deflocculation of the samples was performed by mixing approximately 1 g of wet sediment with a Calgon electrolytic solution (sodium hexametaphosphate; 20 g L⁻¹) and subsequently shaking for at least 3 h using an in-house rotator. The grain-size distribution and parameters were calculated using the moment methods from the Excel GRADISTAT software (Blott and Pye, 2001). IRD abundance was determined using the method described by Grobe (1987), which consists of counting the >2 mm fraction on the X-ray image of the core (here, X-CT scan image). Moreover, the end-member modelling analysis (EMMA) developed by Weltje (1997) and adapted by Dietze et al. (2012) was applied to the grain-size data to extract the meaningful end-member (EM) grain-size distribution and estimate their proportional contribution to the sediment. The cumulative explained variance (r^2) was calculated to assess the minimum number of EMs needed for a good estimate of our grain-size data (e.g., Weltje, 1997; Prins & Weltje, 1999; Dietze et al., 2012). The grain-size distribution and EMMA were used to investigate the sedimentary regime because the grain-size distribution reflects the transport conditions (Montero-Serrano et al., 2009; Dietze et al., 2012; Simon et al., 2012; Stuut et al., 2014).

3.4. Elemental geochemistry

A total of 9 major and minor elements (Al, Si, Ti, Mg, Ca, K, Fe, Mn and P) and 5 trace elements (V, Cr, Zn, Sr and Zr) were analyzed by energy dispersive X-ray fluorescence (ED-XRF) spectrometry using a PANalytical Epsilon 3-XL. Before ED-XRF analysis, loss on ignition (LOI) was determined gravimetrically by heating the dried samples up to 950 °C for two hours. Next, to transform the samples into glass pellets, 0.6 g of calcined sediments was mixed with 6 g of lithium borate (CLASSE, pure, 49.75% Li₂B₄O₇, 49.75% LiBO₂, 0.5% LiBr) and melted in Pt-Au crucibles using an automated fusion furnace (CLASSE® M4 Fluxer). Acquired XRF spectra were processed with the standardless Omnia software package (PANalytical). Procedural blanks always accounted for less than 1% of the lowest concentration measured in the sediment samples. Analytical

accuracy and precision were found to be better than 1–5% for major elements and 5–10% for trace elements, as checked by an international standard (USGS SDC-1) and analysis of replicate samples.

3.5. Quantitative bulk mineralogy

Quantitative X-ray diffraction mineralogy (qXRD) of the <2 mm sediment fraction from sediment cores, till and rock samples collected around Devon Island and the Belcher Glacier were studied using the method developed by Eberl (2003) and used in other Quaternary glacial marine studies that address sediment mineralogy (Andrews et al. 2016; Andrews et al. 2018; Deschamps et al. 2018a; Caron et al., 2020). For this, 1 g of each sample was spiked with 0.25 g of corundum and then ground in a McCrone micronizing mill using 5 mL of ethanol. The slurry was dried at 60 °C overnight and then slightly homogenized with an agate mortar. Next, 0.5 mL of vertrel was added to the mixture to prevent the possible agglomeration of finer particles. The powder sample was then sieved (<300 µm), back loaded into the holders and analyzed on a PANalytical X’Pert Powder diffractometer. Samples were scanned from 5° to 65° two theta in steps of 0.02° two theta, with a counting time of 2 seconds per step. The sediment XRD scans obtained were converted into mineral weight percent (wt.%) of non-clay and clay minerals using the Excel macro program ROCKJOCK v11 (Eberl, 2003), which uses a full-pattern fitting method that permits the quantification of whole-sediment mineralogy with a precision of ±3 wt % (Eberl 2003). The calculated total mineral wt.% was normalized to a sum of 100%. The principal minerals that were analyzed by this method are quartz (Qz), K-feldspar (Kfs), plagioclase (Pl), calcite (Cal), dolomite (Dol), amphibole (Am), Fe-bearing, amorphous silica (A. silica), kaolinite (Kln), chlorite (Chl), illite (Ill), biotite (Bt), muscovite (Mus), smectite (Sme) and vermiculite (Vrm).

3.6. Carbon and nitrogen analyses

Carbon (C) and nitrogen (N) analyses were performed on 42 samples of 27BC at ISMER and 30 samples of 02PC at GEOTOP (Montreal, Québec) to determine variations in sources of organic matter (OM). The total carbon (TC) and total organic carbon (TOC)

contents were analyzed in the bulk and carbonate-free (1 N HCl treatment) fractions, respectively. TC and TOC contents in the 27BC samples were determined with a COSTECH 4010 elemental analyzer, while 02PC samples were analyzed with a Carlo-Erba NC 2500 elemental analyzer. Organic carbon isotopes ($\delta^{13}\text{C}_{\text{org}}$) and total nitrogen isotopes ($\delta^{15}\text{N}_{\text{total}}$) were measured in the carbonate-free and bulk fractions, respectively. At ISMER, C and N isotopic compositions were measured using a continuous flow system that comprises an elemental analyzer (COSTECH 4010) interfaced with an isotope ratio mass spectrometer (IRMS; Thermo Scientific Delta-plus XP). At GEOTOP, C and N isotopic compositions were determined with a Micromass IsoprimeTM IRMS coupled to an Elementar Vario MicroCube elemental analyzer in continuous flow mode. All $\delta^{13}\text{C}_{\text{org}}$ values are given in ‰ versus the Vienna Pee-Dee Belemnite (VPDB) standard, and $\delta^{15}\text{N}_{\text{total}}$ values are expressed as ‰ versus air. Analytical precision and accuracy were determined by replicating analyses of samples and replicate analyses of in-house and international standards (caffeine, nannochloropsis and Mueller Hinton Broth at ISMER, and low organic content soil standard B2152, DORM-2 and Casein at GEOTOP) and were better than ± 0.015 (1σ) for C, $\pm 0.2\text{‰}$ (1σ) for $\delta^{13}\text{C}_{\text{org}}$ and $\pm 0.4\text{‰}$ (1σ) for $\delta^{15}\text{N}_{\text{total}}$. The cross-plot of $\delta^{13}\text{C}_{\text{org}}-\delta^{15}\text{N}_{\text{total}}$ is used to distinguish between marine and terrestrial sources for sedimentary OM (e.g., Meyers 1994; St-Onge and Hillaire-Marcel, 2001).

3.7. Magnetic and paleomagnetic analyses

The magnetic properties of cores 27BC and 02PC were obtained by measuring the hysteresis properties of bulk samples with a Princeton Measurements MicroMag 2900 alternating gradient force magnetometer (AGM) to determine the saturation magnetization (Ms), saturation remanence (Mrs), coercive force (Hc) and remanent coercive force (Hrc). The Mrs/Ms and Hrc/Hc ratios were calculated and reported in a biplot (Day et al. 1977). These ratios are used as magnetic grain-size proxies.

Core 02PC was also subsampled with U-channels (u-shaped plastic liners 2x2 cm in cross section and up to 1.5 m in length) for continuous paleomagnetic analysis. The measurements were performed using a 2G EnterprisesTM SRM-755 cryogenic

magnetometer. The natural remanent magnetization (NRM) was measured by alternating field (AF) demagnetization from 0 to 85 mT using 16 steps of demagnetization to determine the characteristic remanent magnetization (ChRM). Then, a continuous field was applied with a peak AF of 100 mT in the presence of a direct current (0.5 mT) followed by peak AF demagnetization from 0 to 85 mT to measure the anhysteretic remanent magnetization (ARM). The isothermal remanent magnetization (IRM) was then induced with a 300 mT direct current, followed by the same AF demagnetization steps as the ARM. Finally, saturated isothermal remanent magnetization (SIRM) was induced with a direct current of 950 mT and demagnetized at AF peaks of 0, 10, 30, 50, 70 and 90 mT. The IRM and SIRM were induced with a pulse magnetizer. The first and last 4 cm of each section were excluded because the response function of the magnetometer pick-up coils integrates measurements over several centimeters (7–8 cm).

The ChRM inclination and declination were calculated by principal component analysis (PCA; Kirschvink 1980) using AF demagnetization steps between 10 mT and 50 mT using the Excel macro developed by Mazaud (2005). This computation also gives the maximum angular deviation (MAD) and the median destructive field (MDF). MAD values lower than 5° indicate high-quality data (Stoner and St-Onge 2007).

3.8. Chronostratigraphic framework

The chronology of core 27BC was assessed with ^{210}Pb measurements. Approximately 1.5 g of dried and crushed sediment was sampled at 1 cm intervals down to 20 cm. The ^{210}Pb measurements were performed at the GEOTOP research center (Montréal, Canada) by alpha spectrometry. Excess ^{210}Pb measurements were processed by counting the activity of the ^{210}Po daughter isotope (Zhang, 2000) and the ^{209}Po was used as a chemical yield. The counting error was evaluated at $1\sigma \sim 2\text{--}4\%$. To estimate the sedimentation rates, we firstly visually determined the $^{210}\text{Pb}_{\text{supported}}$ and secondly calculated the $^{210}\text{Pb}_{\text{excess}}$ ($^{210}\text{Pb}_{\text{excess}} = ^{210}\text{Pb} - ^{210}\text{Pb}_{\text{supported}}$). Then, the constant rate of supply (CRS) model (Appleby and Oldfieldz, 1983; Oldfield and Appleby, 1984) was used to calculate the average SR as

follows: $SR = -\ln(2)/(slope * 22.3)$ where 22.3 is the half-life of ^{210}Pb (Ghaleb, 2009). The slope is derived from the linear regression between the $\ln(^{210}\text{Pb}_{\text{ex}})$ versus depth.

The chronology of core 02PC was assessed by combine ^{14}C dating with paleomagnetic data. Three ^{14}C ages were obtained from shell fragments (*Hiatella arctica*; 371 cm and 413 cm) and a well-preserved shell (*Portlandia arctica*; 436 cm; Table 2). ^{14}C measurements on pelecypod shells were performed at the Keck Carbon Cycle AMS laboratory from the University of California - Irvine (California, USA). The conventional ^{14}C ages were calibrated using the CALIB 7.1 software (Stuiver & Reimer 2017; <http://calib.org/calib/>) and the Marine20 dataset (Heaton et al., 2020). A regional reservoir age correction of $\Delta R = 157 \pm 18$ years was applied, corresponding to the mean reservoir age corrections reported by three modern shell samples from near the study area (McNeely et al. 2006; Coulthard et al. 2010; Dyke et al. 2019). The R software package BACON was used to produce the ‘best fit’ linearly interpolated age models (Blaauw and Christen 2011). BACON uses a Bayesian approach to estimate the best fit or weighted mean age for each depth with a 95% confidence interval that allows calibrating single radiocarbon ages and taking into account other chronostratigraphical markers (such as ^{210}Pb dating and paleomagnetic tie points). The paleomagnetic data were compared with another paleomagnetic record from northern Baffin Bay (St-Onge and St-Onge 2014) and the CALS10k.1b geomagnetic field model (Korte et al. 2011) in order to establish a chronostratigraphy for this area.

Table 2. Radiocarbon ages from core 02PC. The ages were calibrated with the Marine20 calibration curve with a $\Delta R = 157 \pm 18$ (Heaton et al., 2020).

Laboratory number	Depth (cm)	Dated material	^{14}C ages (yr BP)	Error (\pm yr BP)
UCIAMS-221385	371	<i>Hiatella arctica</i>	9185	20
UCIAMS-221386	413	<i>Hiatella arctica</i>	9585	20
UCIAMS-221387	436	<i>Portlandia arctica</i>	9825	20

3.9. Statistical approach

PCA was performed on the mineralogical and elemental geochemical data. The main goal of this analysis was to identify associations with similar relative variations (e.g., von Eynatten et al., 2003; Montero-Serrano et al., 2010b). A total of 10 key minerals (quartz, plagioclase, K-feldspar, carbonate, Fe-bearing, amphibole, kaolinite, biotite+chlorite, illite, and smectite) and 9 major elements (Mn, P, Ti, Al, Fe, Si, K, Ca and Mg) were used in the PCA. A log-centered (clr) transform was applied to all data sets (Aitchison, 1990). This operation removes statistical constraints on compositional variables, such as the constant-unit sum, and allows the valid application of classical (Euclidean) statistical methods to compositional data (e.g., Aitchison, 1990; Montero-Serrano et al., 2010). PCA was conducted with Compositional Data Package (CODAPAK) software (Comas & Thió-Henestrosa, 2011), which automatically applies a log-centered (clr) transformation to the data.

3.10. Sediment sources and unmixing model

We used the nonlinear unmixing Excel macro program SedUnMixMC (Andrews et al., 2015; Andrews and Eberl, 2012) to explore and quantify long-term variations in bulk sediment provenance. The program uses a Monte Carlo approach to randomly sample ($n = 100$) the available source samples, defines a degree of fit between the observed and

calculated minerals (raw data), and calculates a standard deviation of the estimates for each sample and each source (Andrews and Eberl, 2012; Caron et al., 2020). To quantify potential sources of sediment, seven terrestrial samples and two marine surface sediment samples were retrieved during the 2018 and 2019 ArcticNet expeditions (Montero-Serrano et al., 2018; Montero-Serrano and Brossard, 2019) and processed for qXRD (Fig. 6): three samples were collected near the Belcher Glacier (2 till and 1 rock) and are representative of the Canadian Shield source; four were collected on southwestern Ellesmere Island and are characteristic of detrital carbonate-rich sources of Cambrian-Devonian age; and two marine surface sediment samples were collected in the South Cape Fiord (close to the Sydkap Glacier), which are also derived from detrital carbonate-rich sources. In addition, qXRD data of four marine sediment samples rich in kaolinite and chlorite (HU820038, HU85-048, sap 2, sap021 from Andrews et al., 2018) were used in the sediment unmixing model. Note that although these last sediment samples were collected around Baffin Bay, they are representative of sediments derived from weathered sources (Andrews et al., 2018). Overall, we ran SedUnMixMC on the normalized (100%) data for the 10 key minerals (Fig. S8) that represent more than 83% of the overall mineral concentration in the sediment samples.

4. RESULTS AND INTERPRETATIONS

4.1. Chronology of the cores

4.1.1. Core 27BC

The chronology of core 27BC was determined based on ^{210}Pb dating of the top 20 cm. The ^{210}Pb total activity profile indicates a supported ^{210}Pb activity of 41.9 mBq/g. The excess ^{210}Pb was calculated by subtracting the supported ^{210}Pb from the total ^{210}Pb activity (Fig. 7). $^{210}\text{Pb}_{\text{excess}}$ activities plotted on a logarithmic scale reveal two linear trends that suggest two mean SR of $0.074 \pm 0.015 \text{ cm yr}^{-1}$ below 7.5 cm and $0.103 \pm 0.016 \text{ cm yr}^{-1}$ in the uppermost part of the sequence (0-7.5 cm; corresponding to the period from 1954 to 2017 AD; Fig. 7). The SR calculated in the uppermost part of core 02PC ($\sim 0.071 \text{ cm yr}^{-1}$)

are similar to those in core 27BC. On this basis, core 27BC spans the last 550 years, from ~1467 to 2017 AD (Fig. 7).

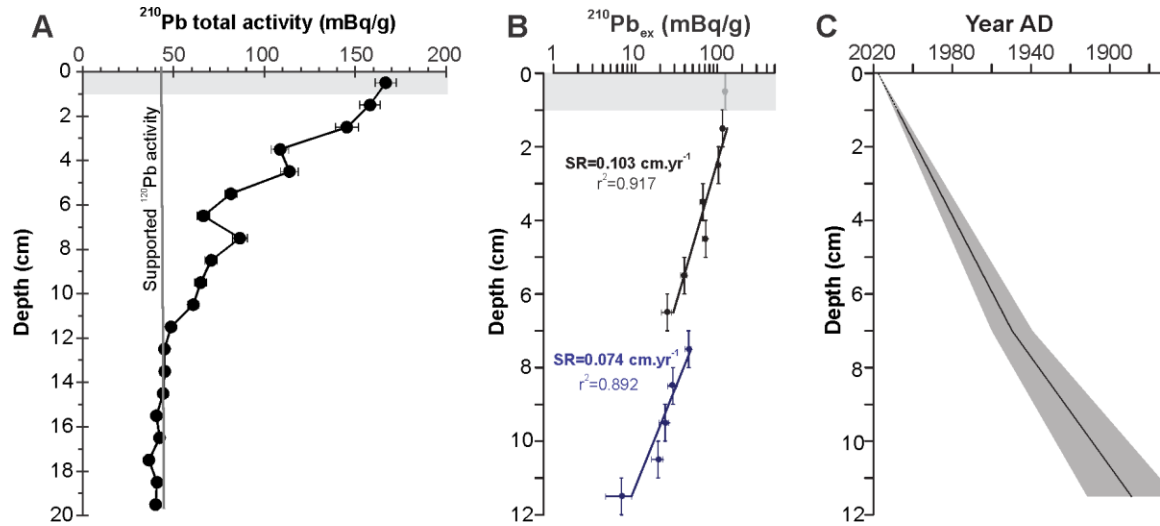


Fig. 7. (A) ^{210}Pb total activity in the top 20 cm of core 27BC. The vertical line represents the supported ^{210}Pb activity (asymptote = 41.9 mBq g $^{-1}$). (B) Logarithm of excess ^{210}Pb activity used for the estimation of mean sedimentation rates (SR). The gray boxes in (A) and (B) represent the biological mixing zones. (C) Age-depth model for the first 12 cm of core 27BC.

4.1.2. Core 02PC

Considering the difficulties of chronostratigraphic methods in the Canadian Arctic, mostly because of the poor preservation of foraminifera and mollusks (Aksu, 1983; de Vernal et al., 1992; Azetsu-Scott et al., 2010), a combination of dating techniques, including AMS ^{14}C and paleomagnetic analysis, were used to produce a reliable age model for core 02PC. Indeed, only very few foraminifera (<0.05 mg) were recovered in core 02PC, which was not enough to perform AMS analysis. All AMS ^{14}C dates were obtained on shells and shell fragments found between 370 and 440 cm and suggest that the age of the core below 440 cm is as old as 10.5 cal ka BP. Further support of the age model at the base of core 02PC comes from the assumption that the detrital carbonate (DC)-rich layer

observed between 429 and 493 cm corresponds with the most recent Baffin Bay Detrital Carbonate event (BBDC-0) dated between 10.7 and 12.2 cal ka BP in northern Baffin Bay (Andrews et al., 1998; Simon et al., 2014).

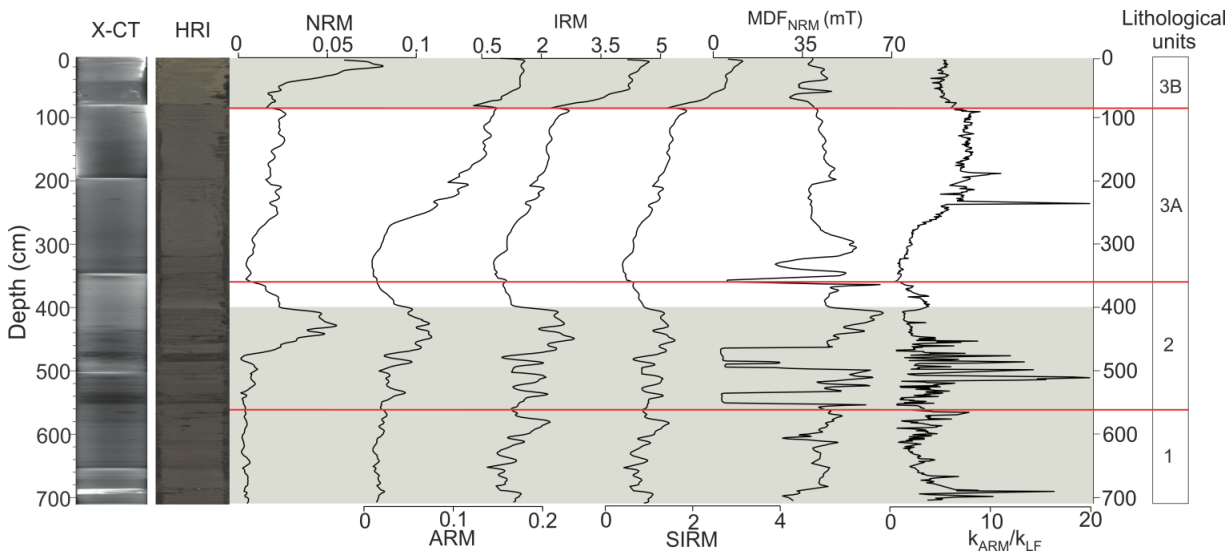


Fig. 8. Magnetic properties for core 02PC. X-ray computed tomography images (X-CT) of the core; High-resolution digital image (HRI); natural remanent magnetization (NRM), anhysteretic remanent magnetization (ARM), isothermal remanent magnetization (IRM), saturated isothermal remanent magnetization (SIRM) calculated for the demagnetization range from 10-50 mT; MDF_{NRM} (mT) is a magnetic mineralogy indicator; k_{ARM}/k_{LF} is a magnetic grain-size indicator (lower values indicate an enhanced contribution of coarser magnetic grains, whereas higher values indicate finer magnetic grains; Banerjee et al., 1981). Distinct lithological facies are delimited by red lines. Unreliable intervals for paleomagnetic reconstruction are highlighted in gray.

To compensate for the lack of AMS ^{14}C dates in the upper 360 cm of core 02PC, paleomagnetic secular variations (PSVs) were used as a complementary dating tool. The paleomagnetic analysis for core 02PC reveals a strong and stable ChRM (Fig. S6). Moreover, we observe a coherent directional signal as the ChRM inclination varies around the expected inclination based on the geocentric axial model (GAD) (82.7° ; Fig. S6). Nevertheless, two intervals in the core (0-88 cm and 400-705 cm) follow the GAD slightly less. Those intervals (highlighted in gray in Fig. 8) are considered less reliable for the

relative paleointensity (RPI) reconstruction and are thus excluded from the reconstruction. Several criteria must be fulfilled to assess the reliability of an RPI proxy (e.g., Tauxe, 1993; Stoner and St-Onge, 2007). The magnetic parameters and hysteresis properties are well defined by a strong and stable ChRM, with low coercivity ferrimagnetic minerals (magnetite) mostly in the pseudo-single domain (PSD) (Fig. S4). Likewise, the MAD values (Fig. S6) are mostly below 5° and are thus the optimum values we can expect for reliable PSV data (Tauxe, 1993). Overall, the sediment magnetic properties satisfy all the criteria for good quality material and can be used for the determination of the RPI and PSV sequences.

Following this, the inclination, declination and relative paleointensity (RPI) were compared with the spherical harmonic model of the geomagnetic field CALS10k.1b (Korte et al., 2011) covering the last 10,000 years and with another Holocene regional paleomagnetic record (HU2008-42PC; St-Onge and St-Onge, 2014). This comparison reveals coherent changes in the geomagnetic field behavior and allows the determination of paleomagnetic tie points (Fig. 9). A total of 16 chronostratigraphic markers (tie points) were identified using the inclination, declination and RPI (I, D and P, respectively; Table 3; Fig. 9). These tie points were then used in the construction of an age model. In addition, the correlation of the physical parameters and mineralogical signatures (Pl+Kfs, Cal+Dol) measured in cores 27BC and 02PC suggest that approximately 13 cm of sediments were lost during piston coring at the top of core 02PC (Fig. S1). Therefore, the depth of core 02PC was adjusted, and the age-depth model was generated using corrected depths. Finally, the age model was established using the R package BACON, which is based on a Bayesian approach (Blaauw and Christen, 2011). According to the proposed age model, core 02PC spans the last 12.6 cal ka BP. The age model shows three different SR representing different sedimentary processes, including a glacial regime, deglacial regime and postglacial regime (Fig. 10). Mean SR range $\sim 0.066 \text{ cm yr}^{-1}$ during the glacial/deglacial interval and from 0.042 to 0.074 cm yr^{-1} during the early-middle to late Holocene. Note that the chronology of the basal unit of core 02PC (~ 580 to 700 cm) cannot be established due to the unreliable paleomagnetic data.

Table 3. Paleomagnetic chronostratigraphic markers (tie points) used in this study. The points marked with I, D and P correspond to inclination, declination and RPI, respectively (Fig. 9). The age is expressed in cal a BP.

Tie points	Depth (cm)	Corrected depth (cm)	Age	Age	Age	Mean	SD
	02PC	02PC	02PC	HU2008-42	CALS10k.1b	age	age
I1	95	108	1333		1429	1381	68
I2	1137	150	2267	2466	2209	2267	135
I3	1179	192	4006	3684	3889	3889	163
I4	2236	249	5648	5893	6529	5648	455
I5	2273	286	6904		6889	6897	11
I6	3308	321	7697	8084	7959	7959	198
D1	884	97	589		619	604	21
D2	1164	177	3076	3173	2529	3076	347
D3	1175	188	3454	3673	3489	3489	118
D4	2228	241	4933		5379	5156	315
D5	2283	296	6633	5862	6559	6559	426
P1	990	103	2028	2249	2109	2109	112
P2	2207	220	5005		4659	4832	245
P3	2271	284	6915	6943	7129	6943	116
P4	3342	355	8842	8240	7909	8240	473
P5	3366	379	9346	9324	9419	9346	50

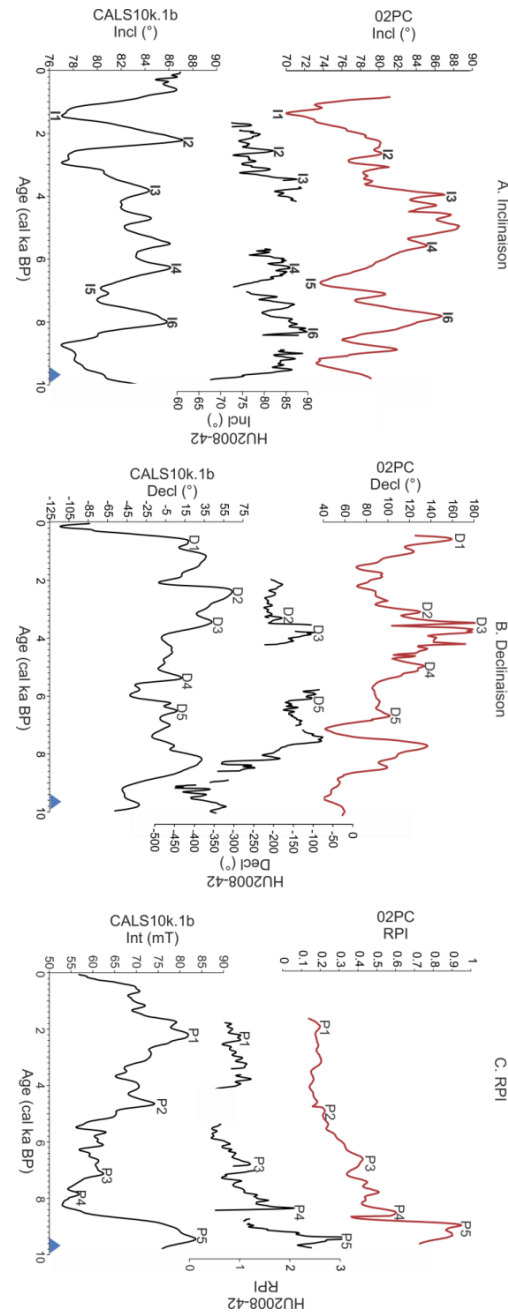


Fig. 9. Full vector paleomagnetic comparison of (A) inclination, (B) declination and (C) relative paleointensity (RPI) from sediment cores 02PC (this study) and HU2008-42 (St-Onge and St-Onge, 2014) and the CALS10k.1b geomagnetic field model (Korte et al., 2011). The blue triangle represents one radiocarbon age determined in this study and used in the age model.

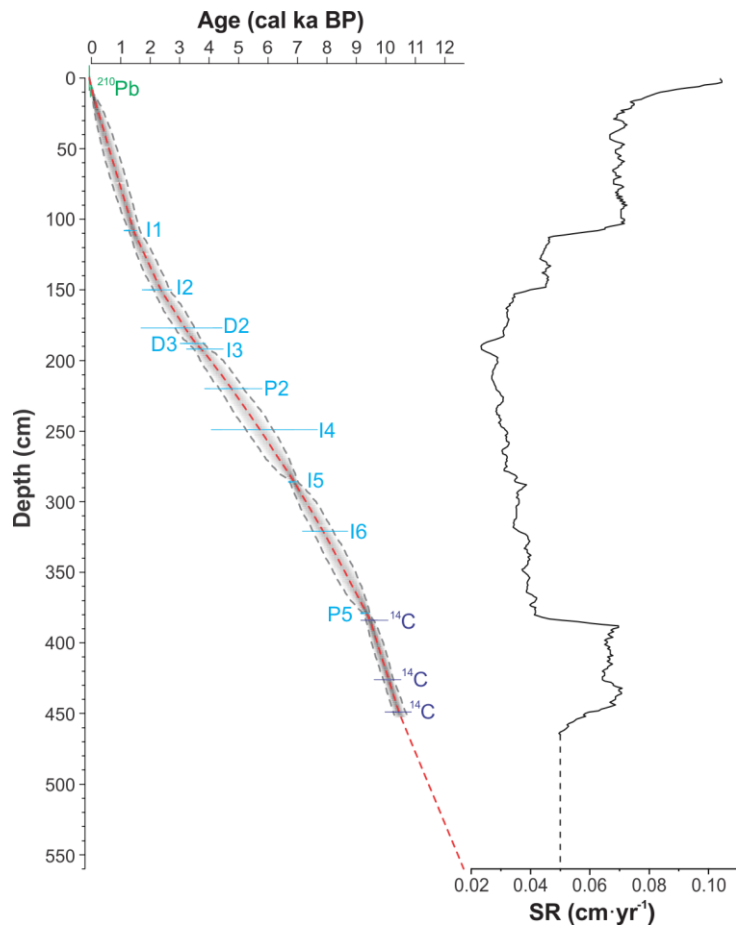


Fig. 10. Composite age model using ^{210}Pb , ^{14}C ages (Table 3) and paleomagnetic tie points (Table 3). The Bayesian age-depth model was constructed using the R package BACON (Blaauw and Christen, 2011). The red dashed line shows the best age model and the gray shading represents the chronological uncertainties (95% confidence interval). Note that the first 80 cm and the basal layer of the core were not reliable for paleomagnetic reconstructions. Due to the lack of dateable material, ages below 10.5 cal ka BP were extrapolated assuming a constant sedimentation rate.

4.2. Mineralogical and geochemical associations

In order to have a better comprehension of the mineral and elemental associations and to choose how to associate them with the different sediment sources, PCA was conducted combining cores 27BC and 02PC (Fig. S2 and S3). The first two principal components

(PC1 and PC2) for both qXRD and ED-XRF accounted for about 90–95% of the total variance and results were distinguished based on age interval. Based on the PCA results, the glacial period is associated with clay minerals (kaolinite, biotite&chlorite, illites and smectite) and Fe-Al-Ti, whereas the deglacial period is associated with detrital carbonates (Cal+Dol) and Ca-Mg. Finally, the postglacial period is associated with total feldspars (Pl+Kfs), amphibole and K. Thus, we selected the Pl+Kfs/total clays, Cal+Dol/total clays, Al/Ca and Ca/Fe ratios to reconstruct downcore changes in detrital input and provenance since the last deglaciation. Likewise, changes in sediment grain size were also investigated by using the Zr/Al ratio. Indeed, Zr is concentrated in zircon grains in the coarser fractions, whereas Al is preferentially associated with clay minerals and aluminosilicate in the fine-grained fractions (e.g., Casse et al., 2017).

4.3. Organic carbon sources

4.3.1. Core 27BC

Core 27BC shows a maximum TOC at 36 cm (1.5%) and a slight decrease toward the top. $\delta^{13}\text{C}_{\text{org}}$ and $\delta^{15}\text{N}_{\text{total}}$ exhibit very few variations in the core. $\delta^{13}\text{C}_{\text{org}}$ values are between -25 and -19 ‰, with a maximum at the bottom of the core (40 cm). $\delta^{15}\text{N}_{\text{total}}$ values are between 6.2 and 7.0 ‰ and are at their lowest at the bottom of the core (42 cm). High $\delta^{13}\text{C}_{\text{org}}$ and $\delta^{15}\text{N}_{\text{total}}$ suggest that the organic compounds in core 27BC mainly come from marine sources (Fig. 11).

4.3.2. Core 02PC

The glacial period (705-560 cm) is composed of the highest TOC, with a maximum of 1.9% at 632 cm, whereas the $\delta^{13}\text{C}_{\text{org}}$ signature is the lowest of the whole core and varies between -25.7 and -25.9 ‰ (Fig. 14A). The $\delta^{13}\text{C}_{\text{org}}-\delta^{15}\text{N}_{\text{total}}$ cross-plot (Fig. 11) suggests that organic compounds during the glacial period were mostly of terrigenous origin with values close to the terrestrial OM EM. The deglacial period (560-360 cm) shows a net decrease in TOC from 1.1 to 0.1%, while $\delta^{13}\text{C}_{\text{org}}$ values increase from -27.5 to -23.9 ‰ at 408 cm and $\delta^{15}\text{N}_{\text{total}}$ values increase from 3.1 to 5.4 ‰ (Fig. 14A). This suggests a transition from terrestrial OM to marine OM (Fig. 11). The postglacial period (360-0 cm)

shows a slight increase upwards of the TOC (0.3 to 1.4 %), $\delta^{13}\text{C}_{\text{org}}$ (-23.5 to -22.1 ‰) and $\delta^{15}\text{N}_{\text{total}}$ (6.6 to 7.4 ‰). $\delta^{15}\text{N}_{\text{total}}$ values show a decrease from 7.4 to 6.6 ‰ at 80 cm. These results suggest that the organic compounds come mostly from marine OM (Fig. 11).

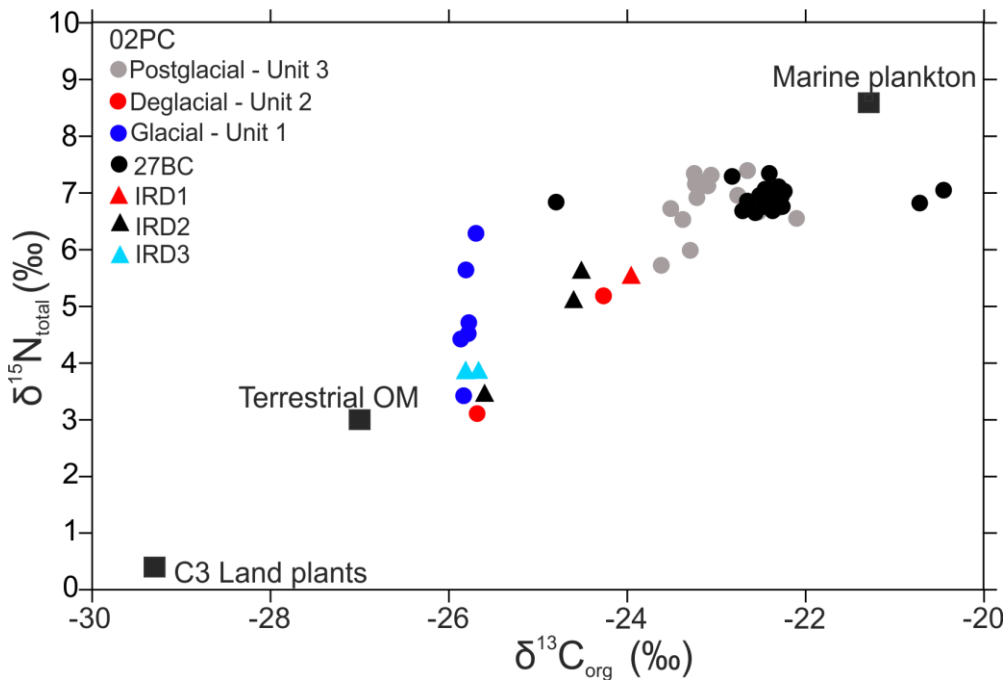


Fig. 11. $\delta^{13}\text{C}_{\text{org}}$ vs. $\delta^{15}\text{N}_{\text{total}}$ for cores 02PC and 27BC. Additional data: C3-land plant and marine plankton EM from Peterson and Howarth (1987) and mean terrestrial OM from Fogel and Cifuentes (1993).

4.4. Grain size end-members

The algorithm of EMMA reveals a polymodal distribution with three grain-size end members (GS-EM; Fig. 12), which explains more than 95% of the total variance. GS-EM1 is associated with clays (<2 µm), GS-EM2 centered on 17 µm is associated with medium to coarse silts (10 to 30 µm), and GS-EM3 corresponds to coarse silts to fine sands (30-100 µm). The poorly sorted and fine-grained characteristics of GS-EM1 are commonly associated with suspension settling from turbid glacial meltwater plumes (Gilbert, 1982). GS-EM2 is consistent with glacial marine settings (Powell, 1981; Jennings, 1993), whereas the poorly sorted and coarse-grained characteristics of GS-EM3 are likely associated with

ice rafting (e.g., IRD and sea ice transport) and intermittent suspended loads (Andrews 2000). The relative contributions of these GS-EMs are plotted against depth in Fig. 12. Both cores are mainly dominated by GS-EM2, while GS-EM3 dominates in the interval with high counts of >2 mm clasts interpreted as IRD in the middle of core 02PC and GS-EM1 dominates at the bottom of core 02PC.

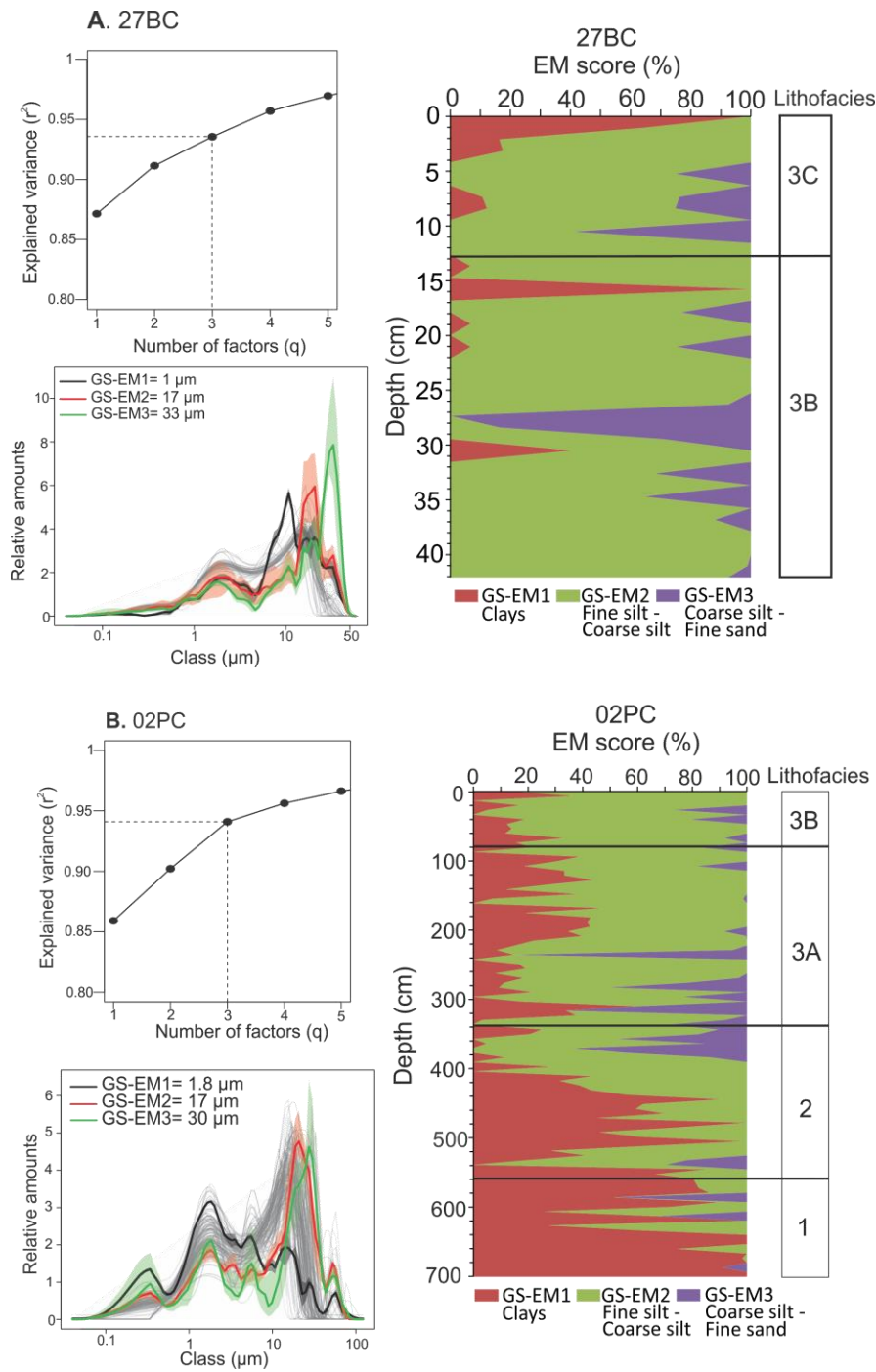


Fig. 12. EMMA performed on the grain-size distribution of the detrital fraction and EM scores (%) derived from EMMA for cores (A) 27BC and (B) 02PC.

4.5. Sedimentary units

The analysis of the sedimentary units of cores 27BC and 02PC was based on visual inspections of the split cores, X-CT scan images, physical properties, sediment grain sizes, and mineralogical and geochemical compositions.

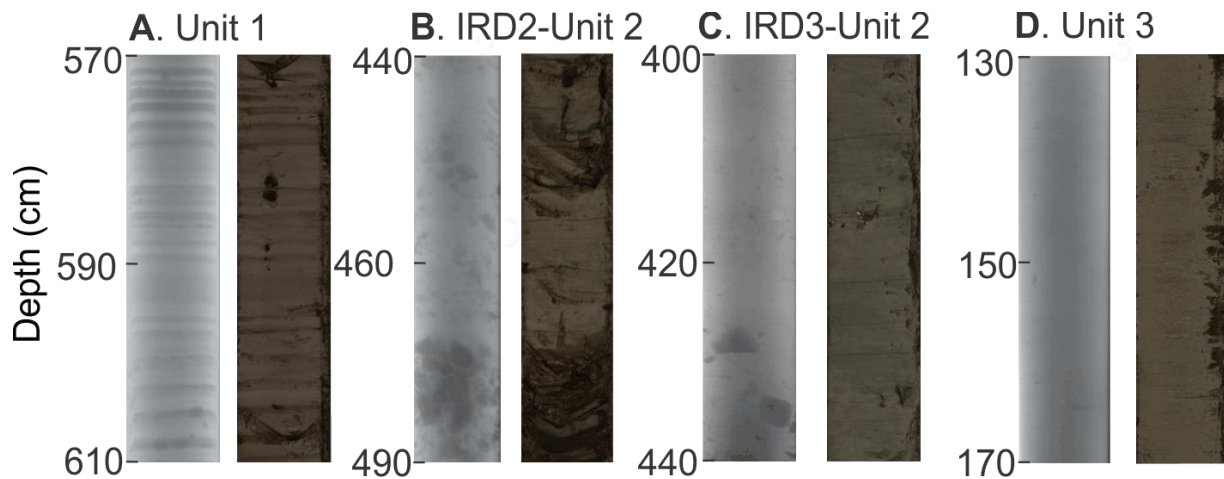


Fig. 13. Examples of X-radiographs and high-resolution photographs of different units identified in core 02PC. (A) Unit 1: laminated clayey silt; (B) Unit 2: IRD2 interval with Cal+Dol coarse silt layer; (C) Unit 2: IRD3 interval with Pl+Kfs coarse silt layer; and (D) Unit 3: homogenous clayey silt.

4.5.1. Core 27BC

Core 27BC presents two distinct sedimentary facies. Unit 3B (1468 to 1866 AD, 42–13 cm) is composed of homogenous dark grayish-brown (2.5Y 4/2) clayey silts (Figs. 13C and 14). Detrital proxies (such as k_{LF} , a^* , wet bulk density, Al/Ca, Ca/Fe and Zr/Al) do not show any significant changes (Fig. 15A). The mean sediment grain size ranges from 4.1 to 6.7 μm (fine silts), and some dropstones are observed towards the base of the unit (between 28 and 35 cm). k_{LF} values show few variations between 42 and 34 cm with a range between 102.9 and 122.3 $\times 10^{-5}$ SI; there is a slight increase at 32.5 cm from 107 to 147.5 $\times 10^{-5}$ SI, and there is a net decrease at 22 and 20.5 cm of 50.7 and 63.3 $\times 10^{-5}$ SI, respectively. Unit

3C (1866 AD to present, 13 cm to the top) is composed of bioturbated olive-brown (2.5Y 4/2) clayey silts and is characterized by high a^* (red) and an increase in several detrital proxies (Fig. 14A). Indeed, a net increase in the Al/Ca ratio and Pl+Kfs concentrations and a decrease in the Ca/Fe and Zr/Al ratios are observed in this unit (Fig. 15A). The grain size and wet bulk density do not show significant changes. There is a slight increase in k_{LF} at 11.5 cm from 114.2 to 138.2×10^{-5} SI, and there is a gradual decrease from 5 cm to the top of the core.

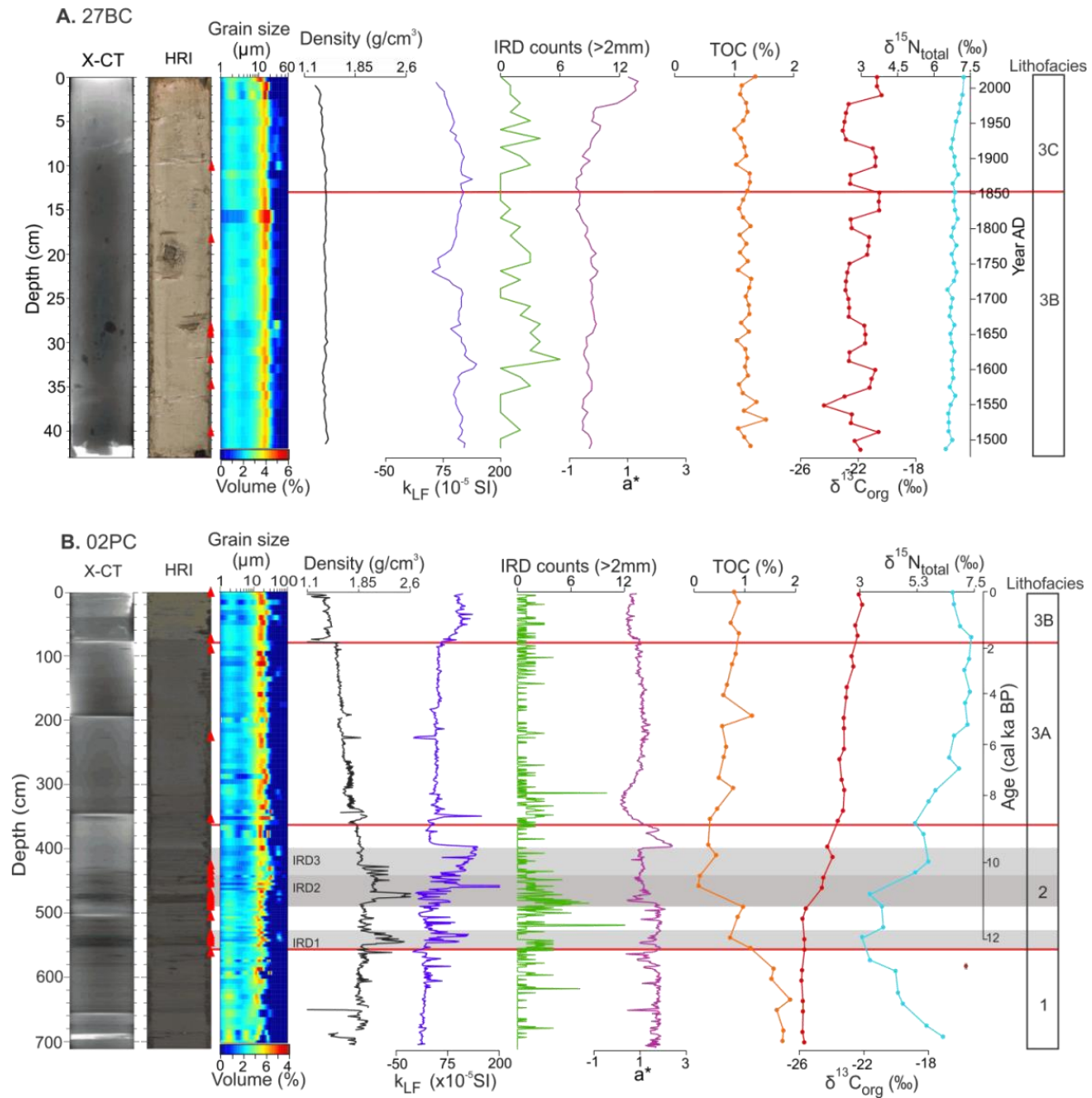


Fig. 14. Downcore variations in core (A) 27BC and (B) 02PC, showing X-CT image, HRI, heat map of grain-size data, wet bulk density, magnetic susceptibility (k_{LF}), IRD counts (>2 mm fraction), a^* , TOC, $\delta^{13}\text{C}_{\text{org}}$ and $\delta^{15}\text{N}_{\text{total}}$. The gray box in (B) represents the IRD-rich intervals identified in core 02PC, and the red triangles represent dropstones. Lithofacies are displayed on the right side of the figure.

4.5.2. Core 02PC

Three different sedimentary units were observed in core 02PC:

Unit 1 (prior to 12.6 cal ka BP, 705-560 cm) is composed of dark gray (10YR 4/1) clayey silts with several dark grayish-brown (10YR 3/2) subcentimeter-scale laminations (Fig. 12). The mean sediment grain size ranges from 2.8 to 7.1 μm (mainly clay and fine silts). Pl+Kfs/clays, Cal+Dol/clays, Ca/Fe and Zr/Al ratios display their lowest values, while kaolinite (up to 16.1%), biotite & chlorite (up to 14.9%) and TOC (up to 1.9%) contents and Al/Ca ratios (up to 5.6) show their highest values (Figs. 14B and 15B). Additionally, GS-EM1 dominates in this part of the core, suggesting a high proportion of fine-grained sediments. The k_{LF} is stable in this unit, varying between -9.5 and 102.3×10^{-5} SI. The MDF_{NRM} values range widely from 3 to 57.4 mT with a mean value of 37 mT, which indicates a variable magnetic assemblage dominated by magnetite (Fig. 8).

Unit 2 (12.6 to 8.9 cal ka BP, 560-360 cm) is composed of grayish-brown silts with pebbles (>2 mm) and shell fragments characterized by higher wet bulk density (up to 2.3 g/cm³) values (Fig. 14B). Some dark grayish-brown (10YR 3/2) laminations are also observed at the base of the unit (Fig. 13). The presence of these numerous pebbles and a dominance of GS-EM3 through Unit 2 strongly suggest glaciomarine deposition with recurrent IRD influence. Moreover, three intervals are very rich in IRD and associated with maximum values of very coarse silts (up to 15%) and fine sands (up to 3%) between 560 and 530 cm (IRD1), between 490 and 440 cm (IRD2) and between 440-400 cm (IRD3). IRD1 is characterized by high quartz (up to 36%), Pl+Kfs (up to 15.3%) and Zr/Al values (up to 0.0036) with a dominance of GS-EM3 (up to 30%), while IRD2 is characterized by high Cal+Dol and Pl+Kfs contents (up to 48.8 and 17.2%, respectively), high Ca/Fe and Zr/Al values (up to 5.1 and 0.0042, respectively), and the lowest Al/Ca values. IRD3 is characterized by high Pl+Kfs (22.1%) and low Zr/Al, Al/Ca and Ca/Fe values (Fig. 15B). The k_{LF} values increase with a peak of 434.8×10^{-5} SI at 461 cm, which represents an IRD layer and a maximum at the top of the core. Unit 2 is also characterized by an increase in the NRM, ARM and IRM. Finally, the MDF_{NRM} values range widely from 2.6 to 63.9 mT with a mean value of 39.2 mT, which indicates the presence of magnetite (Dankers 1981),

as well as other higher coercivity minerals. Higher values of k_{ARM}/k_{LF} observed between 517 and 471 cm indicate variability in the magnetic grain size. On the other hand, the top of Unit 2 (396-360 cm) is characterized by lower k_{ARM}/k_{LF} ratios, indicating coarser magnetic grains.

Unit 3 (8.9 cal ka BP to present, 360 cm to the top) is mainly composed of homogenous olive-gray (5Y 4/1) silts with fine laminations and a mean grain size ranging from 4.1 μm to 9.5 μm (clay to fine silts). Unit 3 was divided into two subunits of different lithological natures. Unit 3A (360-88 cm) shows a progressive increase upward in Pl+Kfs concentration (9.9 to 19.6%) and Al/Ca (0.8 to 2.6) values and a decreasing trend in density (1.82 to 1.03 g/cm³), Cal+Dol (44.8 to 14.6%), quartz contents (25.1 to 13.9%), Ca/Fe (2.7 to 0.7) and Zr/Al (0.0014 to 0.0009) ratios (Figs. 14B and 15B). In this unit, k_{LF} is stable with a peak of 157.2×10^{-5} SI at 351 cm. There is also a gradual increase in the ARM (up to 0.07) and SIRM (up to 1.4). Unit 3B (88 cm to the top) is characterized by a sharp increase in Pl+Kfs (up to 28.3%) content and Al/Ca (up to 3) values as well as by a higher coarse silt content (up to 12%). Cal+Dol contents and Ca/Fe ratios are low in this subunit. The magnetic susceptibility values slightly increase from 59 to 135×10^{-5} SI. The MDF_{NRM} value is constant for Unit 3 (mean value of 39.2 mT), and the NRM, ARM, IRM and SIRM (up to 0.08, 0.016, 4.8 and 3.0, respectively) are higher at the top of the core from 0 to 88 cm (Unit 3B), suggesting a higher concentration of ferrimagnetic minerals. The k_{ARM}/k_{LF} ratio is weaker in Unit 3 than in the previous units, which suggests a coarser magnetic grain size. The NRM, ARM, IRM and SIRM are more stable in Unit 3A than in Units 1 and 2 (Fig. 8). Furthermore, the MDF_{NRM} is more stable than in previous units with a mean value of 39 mT. In Unit 3, together with the hysteresis loops (Fig. S4), the magnetic properties indicate the presence of low coercivity minerals such as magnetite.

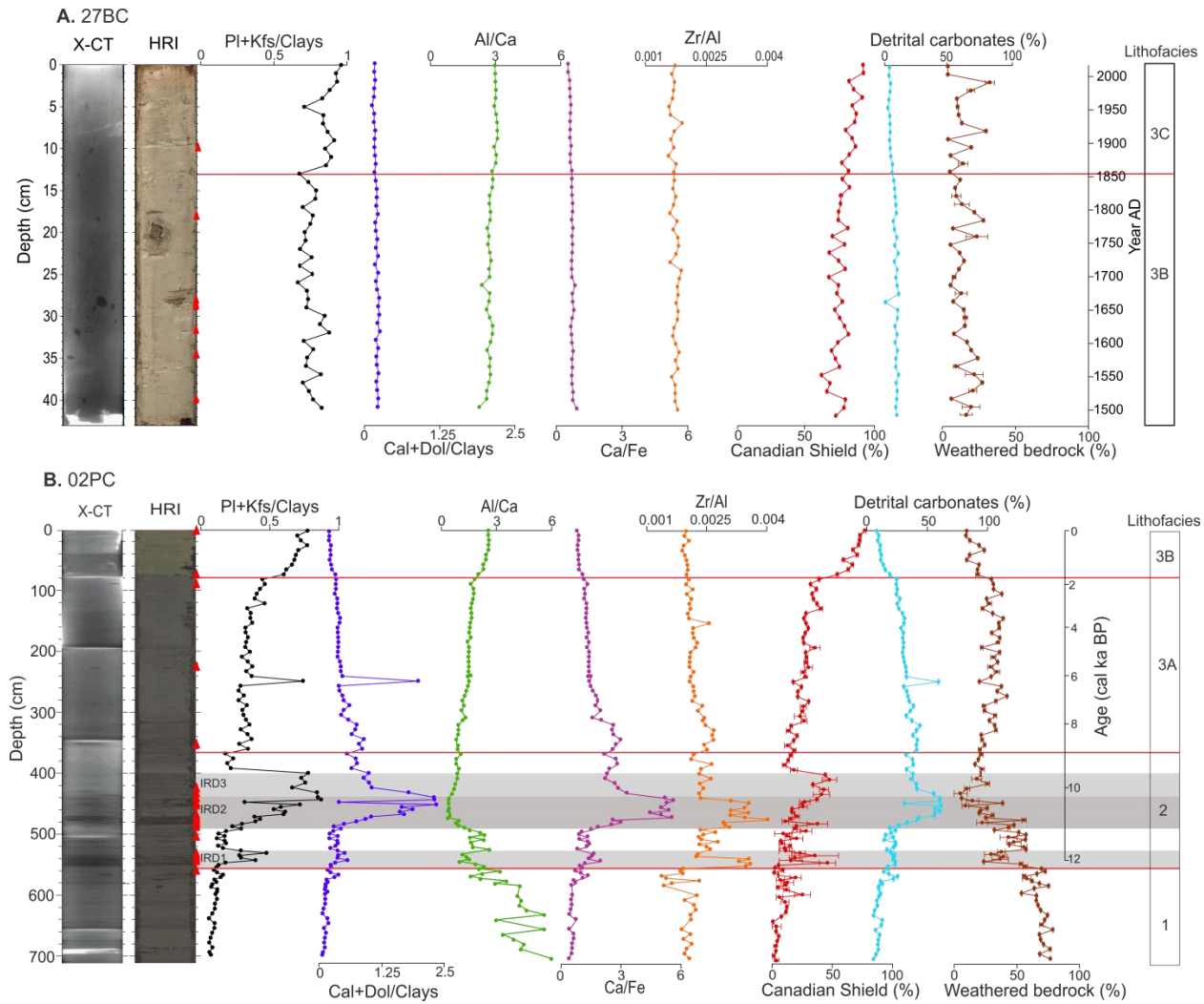


Fig. 15. Downcore variations of core (A) 27BC and (B) 02PC showing: X-ray computed tomography image (X-CT), high-resolution digital image (HRI), ratios of total feldspar/total clays (Pl+Kfs/clays), detrital carbonates/total clays (Cal+Dol/clays), Al/Ca, Ca/Fe and Zr/Al. The grey box represents the IRDs rich intervals in (B) identify in the core 02PC and the red triangles represent dropstones. Lithofacies are displayed on the right side of the figure.

4.6. Sediment provenance

The ternary plot of Al_2O_3 - SiO_2 - CaO (Fig. 16A) illustrates that sediment samples from Unit 1 are enriched in Al and depleted in Si compared to other units, likely reflecting a major input from a clay-rich sediment source, such as weathered bedrock (Fig. 16B).

Moreover, most sediment samples from Units 2 and 3 plot along the mixing line from the Post-Archean average Australian Shale (PAAS) to the detrital carbonate EM (Fig. 16A). This reflects carbonate dilution by a variable contribution in aluminosilicates (mainly feldspars) and quartz-rich sediments during deposition. This last geochemical difference may be related to different sediment sources (Fig. 16B), that is, Al- and Si-rich gneisses and granites from the Canadian Shield and Ca-rich detrital carbonates from the Franklinian mobile belt.

The ternary plot total feldspars–carbonates–kaolinite+chlorite confirms a mineral composition more abundant in kaolinite and chlorite for Unit 1, whereas Units 2 and 3 are composed of a mixture of sediments rich in feldspars and detrital carbonates (Fig. 15). Furthermore, this ternary plot also indicates that the potential sources used in this study have mineral compositions that allow a reasonable degree of sediment discrimination. Indeed, the Canadian Shield source (mainly derived from eastern Devon Island and Coburg Island) is rich in quartz and feldspars, while detrital carbonate sources (Franklinian mobile belt; mainly derived from western Devon and southwestern Ellesmere Islands) are dominated by detrital calcite and dolomite, and weathered sources (likely derived from the Jones Sound seafloor; Harrison et al., 2011) are rich in kaolinite and chlorite with a noticeable proportion of feldspars. Note that because core-top samples (0-1 cm) from cores 27BC and 02PC are rich in quartz (up to 18%) and feldspars (up to 33%), these were also included in the sediment unmixing model as potential Canadian Shield sources.

SedUnMixMC modeling (Fig. 14) reveals that Unit 1 is associated with a high component of weathered sources (60 to 79 wt.%) and Unit 2 is characterized by a decrease in weathered sources (from 50 to 10 wt.%) and an important increase in detrital carbonate sources (30-72 wt.%). In Unit 2, the IRD1 and IRD3 layers have great contributions from the Canadian Shield source (28 wt.% and 51 wt.%, respectively), whereas IRD2 is mainly dominated by detrital carbonate sources (up to 72 wt.%). SedUnMixMC modeling also reveals that in Unit 3, the proportion of sediment derived from the detrital carbonate sources gradually decreases upcore (50 to 10 wt.%), whereas the Canadian Shield source

shows a long-term increase (from 10 to 90 wt.%; Fig. 15). Note that the fraction of source not resolved by the SedUnMixMC program is relatively low (mean ~17 wt.%).

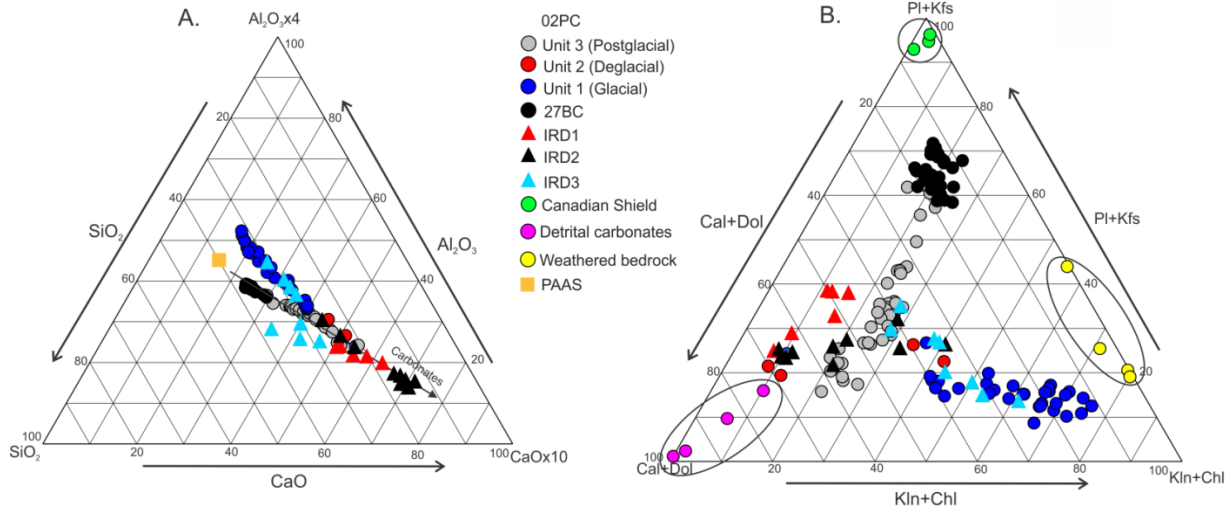


Fig. 16. (A) Al_2O_3 - SiO_2 - CaO ternary plot showing the overall composition of the sediment from cores 27BC and 02PC and the average shale composition (Post-Archean average Australian Shale or PAAS; Turekian and Wedepohl 1961). (B) Total feldspar (Pl+Kfs)-carbonates (Cal+Dol)-kaolinite+chlorite (Kln+Chl) based on the bulk mineralogy and the composition of the three sources of sediments discussed in this study.

5. DISCUSSION

5.1 Unit 1: Glacial sediment dynamics (prior to 12.6 cal ka BP)

The high clay content (GS-EM1) recorded in Unit 1, combined with a lack of bioturbation, low IRD content and well preserved finely laminated intervals, is interpreted to represent the deposition of suspended sediment from subglacial discharge plumes. In an ice-proximal depositional environment, laminated sediments indicate that fine-grained detrital particles were flushed by subglacial meltwater and deposited by either the rain-out of truly fine materials coming from buoyant plumes or gravity flows from the grounding

zone (e.g., Reilly et al., 2019). These sedimentological observations suggest that the core location was between a grounded ice zone and the ice shelf front or open water, without deposition of IRD and no sea ice import.. The high concentrations of clays (notably Kln+Chl), which are less abundant in the crystalline rocks of the Canadian Shield and Paleozoic sedimentary rocks, high Al/Ca and low Zr/Al ratios, and $\delta^{13}\text{C}_{\text{org}}$ values of $\sim 26\text{\textperthousand}$ recorded in Unit 1, together with SedUnMixMC modeling, indicate a specific supply of highly weathered fine-grained terrigenous sediments. Several fluvial–deltaic sedimentary systems ranging from late Miocene to mid-Pliocene in age have been identified on the Jones Sound seafloor during previous seismic surveys (Harrison et al., 2011). Based on these geophysical studies, we hypothesize that sediments in Unit 1 are likely derived from the remobilization of upper Pliocene fluvial deltaic sediments from the Jones Sound seafloor, which were derived from erosion of weathered Precambrian and Paleozoic outcrops (Harrison et al., 2011). This result implies that the core location was closer to grounded ice related to the IIS (England et al., 2008; Dalton et al., 2020) during this period (Fig. 19). Indeed, seafloor mapping together with subbottom profiling of the Belcher Inlet indicates three asymmetric sediment wedges interpreted as grounding-zone wedges (GZWs; Batchelor et al., 2016). Batchelor et al. (2016) indicate that these GZWs illustrate the position of ice margin standstills during overall retreat from the Last Glacial Maximum, in agreement with our interpretations. Overall, our sedimentological, mineralogical and geochemical proxies suggest that during this period: 1) an ice shelf extended from the grounding line in the Belcher Inlet, and likely also at the entrance of the Jones Sound (Dalton et al., 2020), and 2) the glacial sediment dynamics at the location of the core were driven by grounded ice related to the IIS dynamics (Fig. 19).

5.2. Unit 2: Deglacial/early Holocene sediment dynamics (12.6 to 8.2 cal ka BP)

During the deglacial/early Holocene (12 to 8.2 cal ka BP; Walker et al., 2012), high boreal summer insolation drove rapid retreat of the ice sheets (Laurentide Ice Sheet, Greenland Ice Sheet, and IIS; Dyke 1999, 2003; England et al., 2008; Dalton et al., 2020) surrounding northern Baffin Bay, resulting in progressive environmental changes in this

region (e.g., Jennings et al., 2019; Caron et al., 2019, 2020). The net increase in $\delta^{18}\text{O}$ values observed in high-latitude Arctic ice cores (including from Devon and Agassiz Ice Caps; Fisher et al., 1983; Lecavalier et al., 2017) and low sea surface temperature (SST) recorded in Lancaster Sound (core 2004-804-009; Ledu et al., 2010; Fig. 17B) suggest that increased air temperatures (4-5 °C warmer than present; Lecavalier et al., 2017; Fig. 17A) and increased meltwater discharges prevailed in northwestern Baffin Bay during the early Holocene, linked with the Holocene Thermal Maximum (HTM; Kaufman et al., 2004; Gajewski, 2015).

In the Belcher Inlet area during deglaciation (Unit 2), the relatively high SR (~0.05 to 0.09 cm yr⁻¹) compared with those in the middle part of the core, the high wet bulk density (up to 2.2 g cm⁻³), the presence of numerous pebbles and the dominance of coarse-grained sediments (up to 66% of GS-EM3) suggest that sedimentary dynamics were mainly controlled by IRD and meltwater discharges at this time. These deglacial deposition conditions were likely promoted by both high boreal summer insolation and warmer early Holocene air temperatures (Lecavalier et al., 2017). In agreement with other Quaternary glacial marine studies (e.g., Casse et al., 2017; Deschamps et al., 2018, 2019; Caron et al., 2020), sedimentary processes within Jones Sound during the early to middle Holocene could also be influenced by regional relative sea-level (RSL) variations (Dyke, 1998). In fact, the RSL progressively decreased during this interval due to isostatic rebound after the retreat of the IIS in the Jones Sound area (Dyke 1998; England et al., 2008). The glacio-isostatic depression by the IIS over the western sector of Jones Sound was greater than that in the east and induced a higher RSL (+120 m) during the early to middle Holocene than at present (Dyke, 1998). Such marine inundation conditions likely contributed to increasing coastal erosion at the head of Jones Sound (composed of carbonate-rich bedrock outcrops) and therefore a larger Cal+Dol-rich sediment supply from these areas (Fig. 17).

Based on the SedUnMixMC results, we hypothesize that the quartz-, Pl+Kfs- and Zr-rich IRD layers recorded from 12.6 to 12.0 cal ka BP (IRD1) likely originated from the deglaciation of the Coburg Island sector, where crystalline rocks from the Canadian Shield

outcrop (Fig. 2). The net increase in the concentrations of Cal+Dol (up to 48.8%) and Ca-Mg, together with SedUnMixMC modeling, indicate that the IRD-rich interval dated between 11.2 and 10.3 cal ka BP (IRD2) was derived mainly from the deglaciation of the western Devon Island and southwestern Ellesmere Island margins. In agreement with reconstructed patterns of retreat of the IIS in the Jones Sound area during deglaciation (Dalton et al., 2020; Dyke, 1998; Dyke and Evans, 2003; Fig. 19), we suggest that this IRD-rich unit marks the ice retreat into the Jones Sound basin. Enhanced calving rates associated with the deglaciation of Jones Sound could transport detrital Cal+Dol-rich sediments within the icebergs and sea ice to the Baffin Bay basin. The sedimentological characteristics and timing of this detrital Cal+Dol-rich IRD unit could be linked with the BBDC-0 layer recorded between 12.6 and 10.3 cal ka BP in several deglacial sedimentary sequences within Baffin Bay (e.g., Andrews et al., 1998; Simon et al., 2014; Jenner et al., 2018). Likewise, a previous study focusing on foraminiferal assemblages in Smith Sound (Jennings et al., 2019) revealed high relative abundances of the benthic species *Cassidulina neoteretis* between 11.1 and 10.4 cal ka BP, suggesting the influence of chilled bottom waters of Atlantic origin (e.g., Polyak et al., 2002) related to the WGC in the Nares Strait region. There is a faunal switch to *Cassidulina reniforme* after 10.5 cal ka BP, indicating a change to seasonal sea ice conditions (Jennings et al., 2019). Such oceanographic conditions are thought to have promoted the retreat of the ice margin in Smith Sound towards the Kennedy Channel (Jennings et al., 2019). In this context, we find that Jones Sound was completely deglaciated between 11.2 and 10.3 cal ka BP, probably as a result of increased boreal summer insolation and air temperatures and an enhanced influence of the warmer waters from the WGC into northern Baffin Bay during the early Holocene.

From 10.3 to 9.7 cal ka BP, the high SR ($0.08\text{--}0.09 \text{ cm yr}^{-1}$), high k_{LF} (up to $85 \times 10^5 \text{ SI}$), high coarse silt (up to 15%) and Pl+Kfs (up to 22%) contents, SedUnMixMC modeling, subtle laminations with no grain-size grading, and presence of only a few IRD grains at the base of the unit suggest the deposition of glaciogenic sediment, mainly from meltwater plumes that originate from the Belcher Inlet area. This Pl+Kfs-rich layer likely corresponds with the retreat of the Belcher Glacier to the present coastline at ~10 cal ka BP

(Dyke 1999; Dyke and Evans, 2003). Moreover, we hypothesize that the sharp decrease observed in SR (from 0.09 to 0.02-0.04 cm yr⁻¹), Pl+Kfs/clays ratios, k_{LF} values, and in the proportion of sediment derived from the Belcher Glacier at 8.9 cal ka BP suggest that the Belcher Glacier was probably reduced to smaller than its present size at the end of the early Holocene warming. All these observations also reflect the establishment of ice-distal conditions dominated by hemiplegic sedimentation at this time.

5.3. Unit 3A: Middle to late Holocene sediment dynamics (8.0 cal ka BP to 800 AD)

The period from 8 to 3 cal ka BP is associated with the highest relative abundance of “North Atlantic” indicators in the northwestern Greenland margin (core AMD14-204; Caron et al., 2019) and relatively high SST at the entrance of Lancaster Sound (core 2004-804-009; Ledu et al., 2010). This suggests both a strengthened North Atlantic component of the WGC and an enhanced influence of the WGC in northern Baffin Bay (Caron et al., 2019). Such warm oceanographic conditions recorded around the Devon Ice Cap during the middle Holocene promoted both more seasonal sea ice (Mudie et al., 2006) and productive surface waters (Ledu et al., 2010) in this area. In the Belcher Inlet, our results (notably, δ¹³C_{org} and δ¹⁵N_{total}) indicate that the OM is mainly of marine origin during the middle to late Holocene, in agreement with the proposed ice-distal conditions and increase in marine productivity (Figs. 11 and 14).

Furthermore, from 8.0 cal ka BP to 800 AD (Unit 3A), the Pl+Kfs/clays, Cal+Dol/clays, Al/Ca, and Ca/Fe ratios and sediment unmixing models suggest that the proportion of sediment derived from detrital Cal+Dol-rich sources (western Devon and southwestern Ellesmere Islands) dominates during this time with a gradual decrease in this unit (54 to 30 wt.%), whereas Canadian Shield sources (mainly derived from the Belcher Glacier) show a long-term increase (10 to 41 wt.%). In addition, the lower SR (0.02 -0.04 cm ka⁻¹) together with lower very coarse silt contents (<5%) and GS-EM3 values (<20%) observed during the middle Holocene provide evidence for a drastic decrease in erosional processes within the Belcher Glacier. All these results suggest that the Belcher Glacier was

probably reduced in size during the middle Holocene. We speculate that the high local boreal summer insolation and seasonality that characterized the middle Holocene (Laskar et al., 2004) induced a negative balance between winter precipitation and summer ablation in the Belcher Glacier. Detrital proxies derived from proglacial lake sediments on northeastern Baffin Island also suggest that a Holocene glacial minimum occurred ca. 6–2 cal ka BP in this area (Thomas et al., 2010), in agreement with our interpretations.

RSL variations probably continued to influence the sediment dynamics within Jones Sound during the middle Holocene by providing a larger proportion of Cal+Dol-rich sediments from the western part of Jones Sound, as shorelines in these areas were submerged for more than 20 m until ca. 4 cal ka BP (Dyke, 1998). Moreover, based on the good correlation observed between the ice core $\delta^{18}\text{O}$ record from Devon Island Ice Cap and reconstructed SST in northern Baffin Bay, Ledu et al. (2010) suggested that strong atmospheric-oceanic coupling operated throughout the Holocene in this area. The higher SST recorded in northern Baffin Bay during the middle Holocene could have promoted enhanced evaporation and thus snow-rich winters around the Devon Ice Cap at this time (e.g., Thomas et al., 2016). Accordingly, the sedimentary regime in the Belcher Inlet and Jones Sound area is thought to have been dominated by both high RSL in the western Jones Sound basin and a snowmelt runoff regime. The enhanced melting of seasonal snow cover and high postglacial RSL in the western Jones Sound basin could have contributed to a major remobilization of Cal+Dol-rich glaciogenic sediments stored in western Devon and southwestern Ellesmere Islands, as well as subsequent transport towards the Belcher Inlet. This scenario may explain the dominance of detrital Cal+Dol-rich sources in core 02PC during the middle Holocene. High abundance in pre-Quaternary palynomorphs recorded in a nearby core from 02PC during the middle Holocene (Mudie et al., 2006) also suggests a high sediment input from the western Jones Sound basin (including Axel Heiberg basin), which is characterized by sedimentary rocks of Tertiary to Paleozoic ages.

The SR, very coarse silt contents, GS-EM3, coarser magnetic grain size (as shown by the low $k_{\text{ARM}}/k_{\text{LF}}$ ratio), and detrital input from the Belcher Glacier increased markedly

after ~2 cal ka BP in core 02PC, providing evidence for an increase in glacial erosional processes within the Belcher Glacier. Indeed, glacier erosion typically generates a large amount of glaciogenic sediments mainly composed of silt-sized particles, which can then be transported by meltwater streams and deposited in distal glacial marine settings (e.g., Ó Cofaigh et al., 2013; Dowdeswell et al., 2015; Reilly et al., 2019). Thus, assuming that relatively large glaciers produce a higher proportion of glaciogenic sediments (e.g., Røthe et al., 2018), higher Canadian Shield source inputs in the Belcher Inlet can be interpreted to reflect higher Belcher Glacier activity and/or greater meltwater discharges from the Belcher Glacier. Likewise, the late Holocene (4.2 cal ka BP to present; Walker et al., 2012) in the Arctic region is characterized by a cooling trend driven by a long-term decrease in boreal summer insolation, which corresponds to the Neoglacial period associated with glacier growth (e.g., Solomina et al., 2015) and cooler conditions in surface waters (e.g., Ledu et al., 2010; Caron et al., 2019). In the Belcher Inlet, variations in our detrital proxies suggest that the long-term regional cooling that characterized northern Baffin Bay since 6 cal ka BP (e.g., Ledu et al., 2010) led to progressive Belcher Glacier regrowth throughout the middle to late Holocene. This was intensified at the onset of the Neoglacial period at approximately 3-2 cal ka BP. Similar Neoglacial glacier readvances are also suggested for glaciers from northeastern Baffin Island (Briner et al., 2016), Arctic Canada (Solomina et al., 2015; Briner et al., 2016), and Svalbard (Røthe et al., 2018). Overall, our results suggest that RSL variations, high boreal summer insolation and seasonality, and the Neoglacial advance of the Belcher Glacier exerted a significant control on sedimentation in the Belcher Inlet area during the middle to late Holocene.

5.4. Units 3B and 3C: Late Holocene to modern sediment dynamics (800 AD to present)

To explore the potential impacts of insolation variability (Laskar et al., 2004), the Medieval Climate Anomaly (MCA; ~900-1500 AD; Bradley et al., 2003; Spielhagen et al., 2011), the Little Ice Age (LIA; ~1500-1900 AD; Jones and Mann 2004) and modern warming (late 1800s AD; Jones and Mann 2004; Kaufman et al., 2009) on the sedimentary dynamics of the Belcher Glacier, core 27BC and the top of core 02PC (Unit 3B) were

combined into a composite sequence covering the last 800 years (Fig. 18). The first 42 cm of the composite sequence corresponds to core 27BC, and the rest of the sequence corresponds to core 02PC (45 to 85 cm; corrected depth; Fig. S1). In this composite sequence, mineralogical (Pl+Kfs/clays and Cal+Dol/clays) and elemental (Al/Ca and Ca/Fe) ratios, as well as sediment unmixing models, reveal a long-term increase in detrital inputs from the Belcher Glacier (54-92% wt.%), which closely follows the increasing trend in boreal winter insolation (Fig. 18), and a steadily decreasing input in detrital Cal+Dol-rich sources (20 to 4 wt.%). There is also a net increase in the magnetic parameters NRM, ARM, IRM and SIRM, probably associated with a readvance of the ice margin during this period. These results suggest that both the gradual increase in winter insolation and decreased summer insolation promoted a positive balance between winter precipitation and summer ablation in the Belcher Glacier during the late Holocene. In turn, enhanced snow cover and winter precipitation on the Belcher Glacier could have generated a progressive increase in snowmelt runoff and meltwater plumes during spring/summer within the Belcher Inlet. Other Arctic paleoclimatic reconstructions (e.g., D'Andrea et al., 2012; Røthe et al., 2018) also reported a long-term winter warming trend during the middle to late Holocene together with increased winter precipitation, in agreement with our results. Moreover, the decrease in detrital inputs from Cal+Dol-rich sources (Franklinian mobile belt) observed in the composite sequence during the last 800 years suggests a reduced detrital influence of most distal sediment sources in the Belcher Inlet at this time.

During the MCA, which is a climatic period characterized by warmer temperatures in Arctic summer temperature reconstructions (e.g., Moore et al. 2001; Kaufman et al. 2009), the detrital inputs in the composite sequence are characterized by a mixed sediment provenance (mainly originating from the Belcher Glacier with a minor influence from Cal+Dol-rich sources) and lower GS-EM3 values (background levels). This result suggests that sedimentary regimes in the Belcher Inlet were dominated by snowmelt runoff and meltwater plumes with lower iceberg calving rates. Furthermore, GS-EM3 shows high values from 1545-1665 AD and at ~1910 AD, suggesting enhanced silty glacial meltwater discharges and ice rafting from the Belcher Glacier (Fig. 18). The enhanced coarse detrital

input recorded at ~1545-1665 AD occurred during a period of glacier growth and cool conditions related to the LIA (Jones and Mann 2004). This interpretation is in agreement with results from transfer functions based on dinoflagellate cyst assemblages from the nearby core 2008-029-040BC (Cormier et al., 2016), which suggest 0.6 °C cooler than the present summer SSTs and an increase in the duration of sea ice cover between 1560 and 1800 AD in northern Baffin Bay (Fig. 18B). Additionally, the North Atlantic SSTs indicate that the coldest time in the past 3 millennia was between 1400 and 1800 AD (Lapointe et al., 2020). Reconstructed Arctic surface air temperature (Kaufman et al., 2009) and climate model simulations (Crespin et al., 2009) suggest that the cool climatic conditions during the LIA were interrupted by an episode of warming between 1450 and 1650 AD that was driven by enhanced southerly advection of warm air into the Arctic (Kinnard et al. 2011). In this context, and as no substantial changes are observed in the strength of the WGC during the MCA-LIA transition (Perner et al., 2011), we argue that warmer Arctic air temperatures and extended melt seasons during this climatic cold period likely promoted a substantial increase in snowmelt runoff and calving activity from the Belcher Glacier.

Finally, the relatively high GS-EM3 values observed at ~1910 AD, together with a sharp increase (80 to 92 wt.%) in detrital inputs from the Belcher Glacier, suggest an enhanced iceberg calving rate at this time, which marks the beginning of the anthropogenic warming influence on the Belcher Glacier (Fig. 18). The correlation observed between our detrital proxies and the Arctic surface air temperature anomalies during this interval (Fig. 18) supports the idea that increased atmospheric temperature (linked to anthropogenic-induced Arctic amplification; Kaufman et al., 2009) is one of the main factors driving the acceleration in marine-terminating glacier frontal retreat in the CAA during the industrial period (e.g., Lecavalier et al., 2017; Cook et al., 2019). This is also correlated with the current SSTs, which are at their warmest in the past 2 900 years (Lapointe et al., 2020).

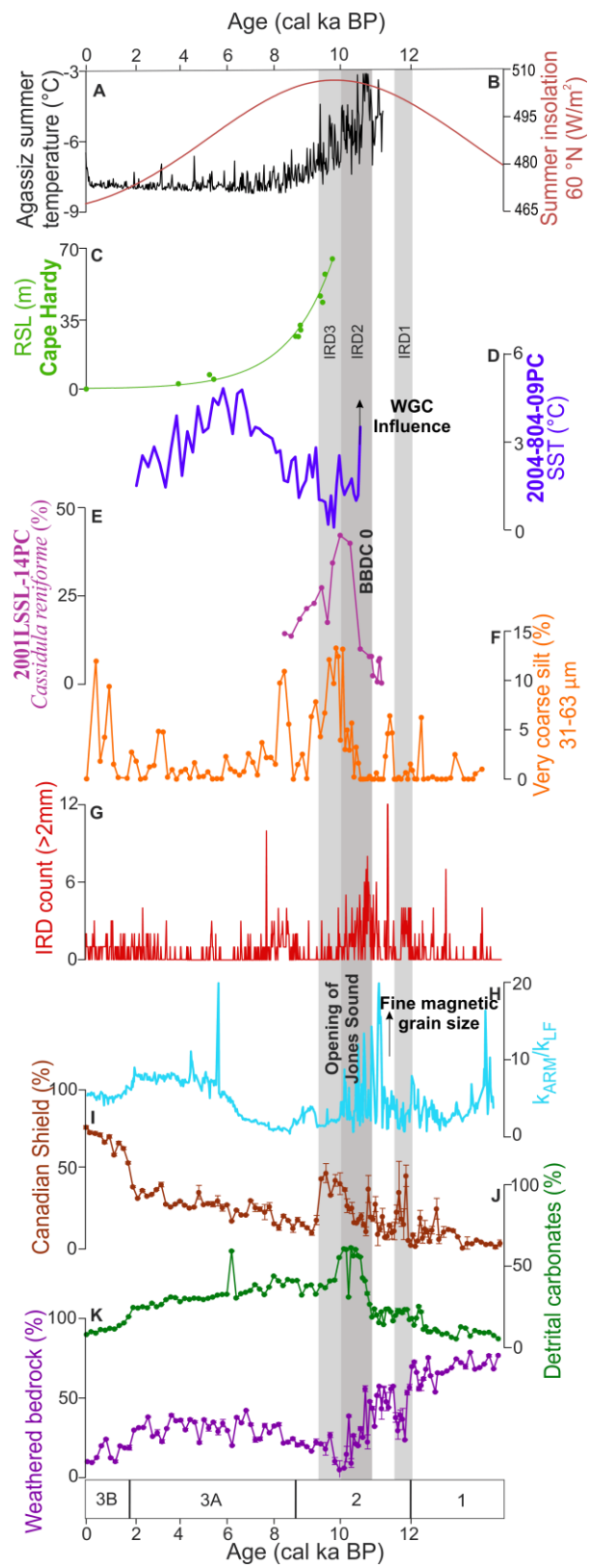


Fig. 17. (A) Summer temperature reconstruction from the Agassiz Ice Cap (Lecavalier et al., 2017), (B) summer insolation at 60°N (W/m^2 , Laskar et al., 2004), (C) RSL reconstruction from Cape Hardy (Devon Island; Dyke, 1998), (D) SST (Ledu et al., 2010), (E) *Cassidulina reniforme* percentages from core 2001LSSL-014 collected in Smith Sound (Jennings et al. 2019); from core 02PC: (F) very coarse silt content, (G) IRD counts of >2 mm clasts from X-CT radiographs, (H) $k_{\text{ARM}}/k_{\text{LF}}$ ratio (magnetic grain-size indicator), and proportion of sediment from the (I) Canadian Shield, (J) detrital carbonates, and (K) weathered bedrock for core 02PC. Note that ages below 12 cal ka BP were extrapolated, and thus, our interpretations remain hypothetical.

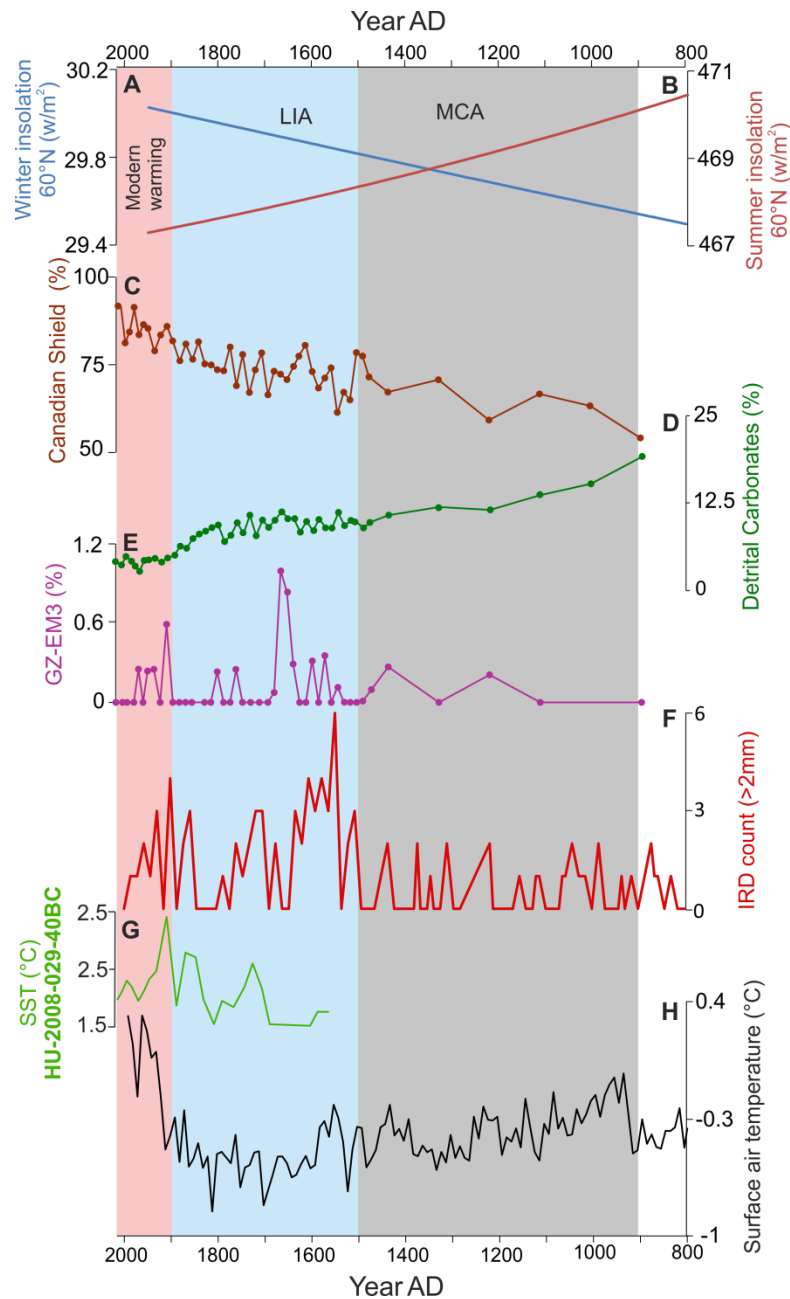


Fig. 18. (A-B) Winter and summer insolation at 60°N (W/m², Laskar et al., 2004), (C-D) proportion of sediments from the Canadian Shield and Paleozoic carbonates, (E) GS-EM3, (F) IRD counts of >2 mm clasts from X-CT radiographs, (G) SST and primary production (Cormier et al., 2016), and (H) reconstructed Arctic surface air temperature (SAT) anomalies (Kaufman et al., 2009).

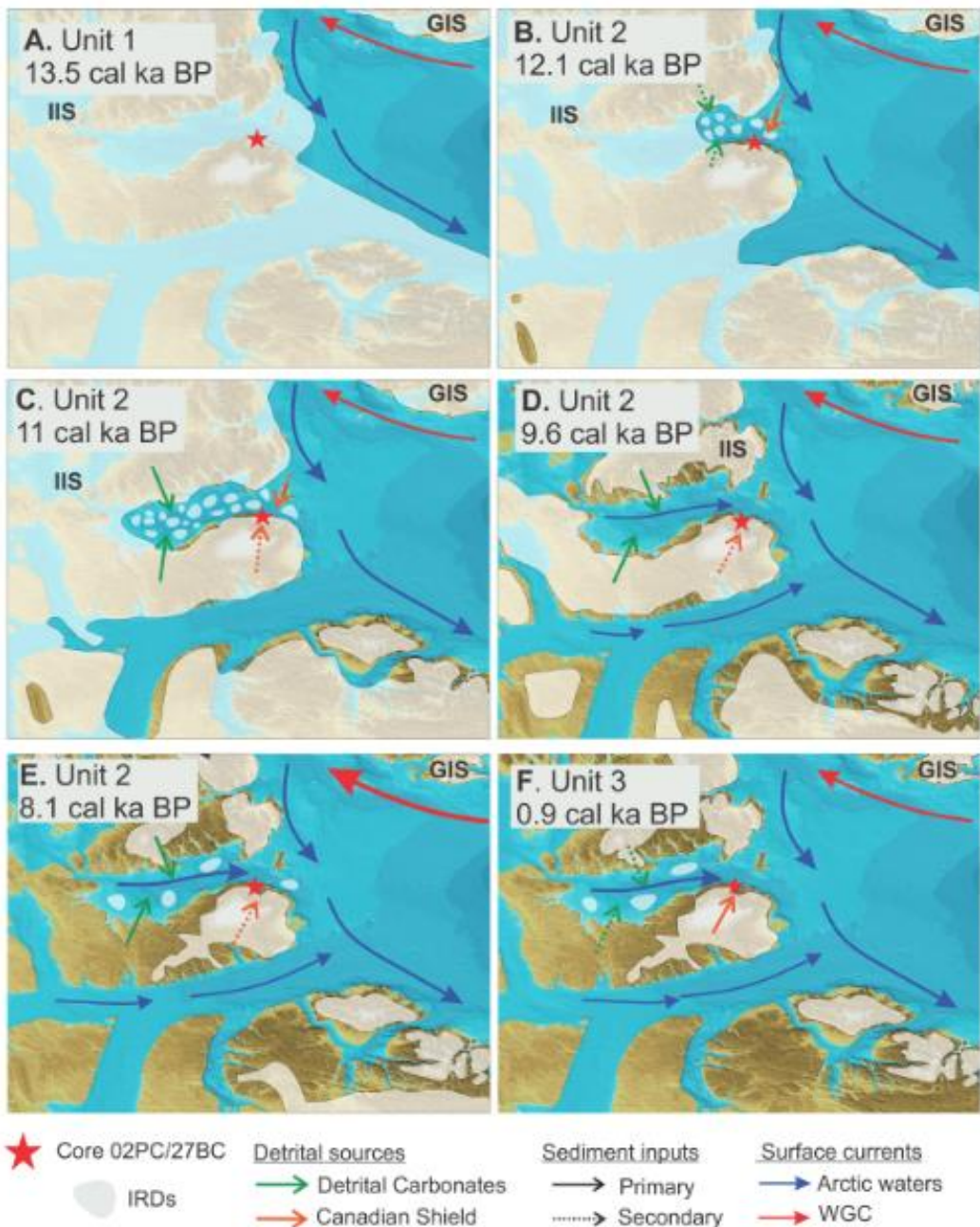


Fig. 19. Schematic map showing the evolution of the sedimentary dynamics in the Jones Sound basin since the last deglaciation. (A) During the last glaciation, at approximately 13.5 cal ka BP, the sediment dynamics were mainly controlled by subglacial outwashes bringing fine-grained sediments (GS-EM1) rich in Kln+Chl, Al and terrestrial OM. An ice shelf could have been present at the entrance of the Jones Sound during this time. (B) Ice margin retreat started at approximately 12 cal ka BP with an increase in iceberg delivery in Jones Sound (IRD1), an increase in Zr/Al- and Pl+Kfs-rich sediments and an increase in the SR. (C) At 11 cal ka BP (IRD2), there is an increase in the Ca/Fe and Zr/Al ratios and Cal+Dol-rich sediments with an increase in the wet bulk density, k_{ARM}/k_{LF} and a predominant marine origin for the OM. These results suggest that sediments originated mainly from the deglaciation of the western Devon and southwestern Ellesmere Island margins and that more distal glaciomarine conditions were established in Belcher Inlet during this time. (D) The Belcher Glacier retreated to the present coastline at ~10 cal ka BP (Dyke 1999; Dyke and Evans, 2003) and promoted a large Pl+Kfs-rich IRD input (IRD3) to the Belcher Inlet. The decrease in the IRD input recorded at approximately 9.7 cal ka BP supports the idea (e.g., Dalton et al, 2020) that deglaciation in the Jones Sound sector ended at this time. (E) During the early mid-Holocene, the proportion of sediment derived from detrital Cal+Dol-rich sources dominate relative to Pl+Kfs-rich sources, suggesting that sediment dynamics continued to be impacted by the progressive inland ice retreat in the southwestern Ellesmere Islands, and that Belcher Glacier was probably reduced in size during this time. (F) During the late Holocene, detrital sediment supply rich in Al/Ca and Pl+Kfs in the Belcher Inlet was largely dominated by meltwater plumes and ice rafting from the Belcher Glacier. The West Greenland Current (WGC) and Baffin Island Current (BIC) are represented by red and blue arrows, respectively. The size of arrows represents the strength/intensity of the ocean currents. The reconstruction of ice sheet extents is adapted from Dalton et al. (2020).

6. SUMMARY AND CONCLUSION

The multiproxy approach performed on the two sediment cores (27BC and 02PC) recovered near the Belcher Glacier highlights the evolution of sediment transport and dynamics since the last deglaciation and reveals important environmental changes within the Jones Sound basin (Fig. 19). Overall, the results of this study yield the following generalizations and conclusions:

- (i) The fine-grained laminated intervals rich in KIn+Chl, Al and terrestrial OM and the low IRD content recorded during the glaciation phase (prior to 12.6 cal ka BP) suggest that glacial sediment dynamics at the location of the core were driven by grounded ice related to the IIS dynamics. These conditions likely promoted remobilization and subsequent transport via subglacial discharge plumes of upper Pliocene fluvial deltaic sediments preserved on the Jones Sound seafloor. Sedimentological observations suggest also that an ice shelf could have been present at the entrance of the Jones Sound during this time.
- (ii) During the deglaciation phase (12.6 to 8.8 cal ka BP), the presence of numerous pebbles and the dominance of coarse-grained sediments together with high SR suggest that the sediment dynamics were mainly controlled by IRD and meltwater discharge related to the deglaciation of the Jones Sound basin. The correlation of our detrital proxies with the reconstructed air temperature record of the Agassiz Ice Cap suggests that the high boreal summer insolation prevalent during the early Holocene likely promoted gradual ice cap and glacier melting in the Jones Sound area.
- (iii) The Pl+Kfs and Zr-rich IRD layers dated from 12.6 to 12.0 cal ka BP (IRD1) are likely related to the deglaciation of the Coburg Island sector, where crystalline rocks from the Canadian Shield outcrop. The detrital carbonate-rich IRD layer from 11.2 to 10.3 cal ka BP (IRD2) originated mainly from the deglaciation of the western Devon and southwestern Ellesmere Island margins and is likely related to the progressive ice retreat of the Jones Sound basin. Following this ice retreat, the Pl+Kfs-rich IRD layer dated from 10.3 to 9.7 cal ka BP (IRD3) derived from the Belcher Inlet area confirms

that the retreat of the Belcher Glacier to the present coastline occurred during the early Holocene.

- (iv) During the middle to late Holocene (8.0 cal ka BP to 800 AD), the gradual decrease in sediment inputs from the Franklinian mobile belt (detrital carbonates) and the progressive increase in sediment derived from the Canadian Shield (gneiss and granite) suggest that sediment dynamics were probably influenced by regional sea-level variations, strengthening of the WGC, and long-term boreal summer insolation variability. Higher Canadian Shield input can also be interpreted by higher Belcher Glacier activity. In addition, the progressive increase in TOC concentrations and dominance of marine OM in core 02PC suggest that ice-distal conditions with more seasonal sea ice and productive surface waters were gradually established in the Belcher Inlet area during this interval. Detrital proxies also suggest a cooling trend since 6 cal ka BP related to the Neoglacial period and characterized by glacier growth and cooler surface water conditions.
- (v) During the late Holocene (800 AD to present), grain size and mineralogical and geochemical proxies suggest that the detrital sediment supply in the Belcher Inlet was largely dominated by meltwater plumes and ice rafting from the Belcher Glacier triggered by increased boreal winter insolation, enhanced winter precipitation and a subsequent increase in snowmelt runoff during spring/summer.
- (vi) Finally, the similar trend observed between the detrital proxies in core 27BC, and the Arctic surface air temperature anomalies since the late 1800s, suggest that increased atmospheric temperatures have an important influence on the Belcher Glacier dynamics during the industrial period.

7. ACKNOWLEDGMENTS

We are grateful to the captain, officers, crew and scientists on board the CCGS Amundsen during the 2017 (Leg 2b) and 2018 (Leg 3) ArcticNet expeditions for the recovery of cores and glacier samples used in this study. We also thank Quentin Beauvais

(UQAR-ISMER), Édouard Philippe (ISMER-UQAR), and Mathieu Babin (ISMER-UQAR) for their technical support and advice in the laboratory. We also thank Anne E. Jennings (INSTAAR, University of Colorado) and André Rochon (ISMER-UQAR) for their insightful comments on an earlier version of the manuscript as well as the American Journal Experts for the support with the English editing. This research was funded by ArcticNet (a Network of Centres of Excellence Canada), GEOTOP, Québec-Océan, CREATE ArcTrain program, and the Natural Sciences and Engineering Research Council of Canada (NSERC) through Discovery Grants to J.-C. Montero-Serrano and G. St-Onge. All analytical data presented will be available electronically in the PANGAEA database (<https://www.pangaea.de/>).

CONCLUSION GÉNRALE

Dans le cadre de ce projet de maîtrise, nous avons utilisé une méthode multi-traceurs : les propriétés sédimentologiques (granulométrie), physiques (couleurs et densité), minéralogiques, géochimiques (éléments majeurs et isotopes) et magnétiques (concentration, granulométrie et minéralogie des grains magnétiques) ont été analysées pour reconstituer les variations de la dynamique sédimentaire du glacier Belcher dans le temps. Ces analyses ont été effectuées sur 2 carottes de sédiments : une courte de 43 cm (27BC) pour une résolution accrue au cours des derniers siècles et une longue de 705 cm (02PC) pour une reconstitution paléoclimatique des derniers milliers d'années. Les différents faciès sédimentaires observés dans ces deux carottes constituent des enregistrements importants des grands changements climatiques dans la baie de Baffin et dans le détroit de Jones.

Dans la carotte 02PC, trois lithofaciès différents ont été observés et reflètent des dynamiques sédimentaires distinctes. La base de la carotte est principalement caractérisée par des laminations d'argile foncée et une granulométrie très fine, ce qui suggère que les sédiments ont été transportés par des courants turbides sous-glaciaires durant la dernière glaciation (avant 12.6 cal ka BP). De plus, ces sédiments sont particulièrement riches en minéraux argileux, soit en kaolinite, chlorite et illite, en plus d'être caractérisés par un rapport Al/Ca très élevé comparativement au reste de la carotte. Ceci indique que ces sédiments proviennent de l'érosion du substrat rocheux altéré suggérant une couverture de glace importante dans le détroit de Jones ainsi qu'une extension maximale et un ancrage du glacier Belcher dans le fond marin. Cette période est suivie d'une intense phase de déglaciation (12.6 à 9.2 cal ka BP) apportant une quantité importante de débris délestés par les icebergs (IRD) dont des dropstones et des couches riches en sable. Cette période est aussi caractérisée par un ratio Ca/Fe plus élevé et un ratio Al/Ca plus faible. Ces débris sont particulièrement riches en dolomie suggérant un apport de sédiments provenant de la déglaciation du détroit de Jones et de l'Ouest de l'Île de Devon. Le début de l'Holocène (9.2 cal ka BP à aujourd'hui) est caractérisé par l'augmentation de la concentration du plagioclase et la diminution de la dolomie, suggèrent un apport de sédiments provenant

principalement du Bouclier canadien, faisant en sorte que le glacier est à son extension minimale et est ancré sur le socle rocheux de l'île de Devon. Par contre, à partir de 6 cal ka BP, les indicateurs détritiques suggèrent un retour vers des conditions plus froides, associées à la période Néoglaciaire. De plus, en combinant le sommet de la carotte 02PC avec la carotte 27BC, on remarque une hausse de l'activité du glacier Belcher avec le réchauffement climatique moderne, soit au début des années 1900s. En effet, l'augmentation de la concentration du plagioclase et du rapport Al/Ca indiquent une augmentation des apports détritiques et des débâcles d'icebergs du Bouclier canadien et donc une activité plus intense du glacier.

Ce mémoire de maîtrise a aussi permis la reconstitution des propriétés magnétiques de la carotte AMD2017-02PC depuis la dernière glaciation. En comparant les résultats avec d'autres données régionales dans l'Arctique canadien et en comparant avec un modèle géomagnétiques, une chronostratigraphie a pu être établie pour pallier aux lacunes du modèle d'âge. Il a été possible de construire un modèle d'âge solide en associant l'inclinaison, la déclinaison et la paléointensité relative (RPI) avec une autre carotte ayant un bon modèle d'âge. Ce modèle d'âge corrèle bien avec les âges ^{14}C des trois coquilles retrouvées dans la base de la carotte et avec les données de ^{210}Pb de la carotte à boite. Par contre, les données paléomagnétiques n'étaient pas fiables au-delà de 10 000 cal a BP et aucune coquille ni de tests de foraminifères n'ont été retrouvés dans la période glaciaire. Une extrapolation du modèle d'âge a donc été faite jusqu'à la base de la carotte.

Ce projet démontre bien l'utilité d'une étude multi-traceurs pour reconstituer la dynamique sédimentaire des glaciers à terminaison marine. En effet, les traceurs décrivent des propriétés différentes et permettent d'avoir une vue d'ensemble sur la dynamique du glacier Belcher. Par exemple, les rapports Al/Ca, Ca/Fe et Zr/Al sont de très bons outils pour reconstituer la variabilité sédimentaire et les processus d'apport de sédiments dans le bassin de Jones. Les concentrations de plagioclase, feldspath-K, quartz et dolomie sont des bons indicateurs pour retracer la provenance et l'origine des sédiments. Finalement, une compréhension précise de la dynamique sédimentaire des autres glaciers de l'AAC pourrait

mener à une meilleure connaissance des changements climatiques dans l'ensemble de cette région et aider à combler les incertitudes scientifiques concernant la dynamique des glaciers à terminaison marine.

ANNEXES

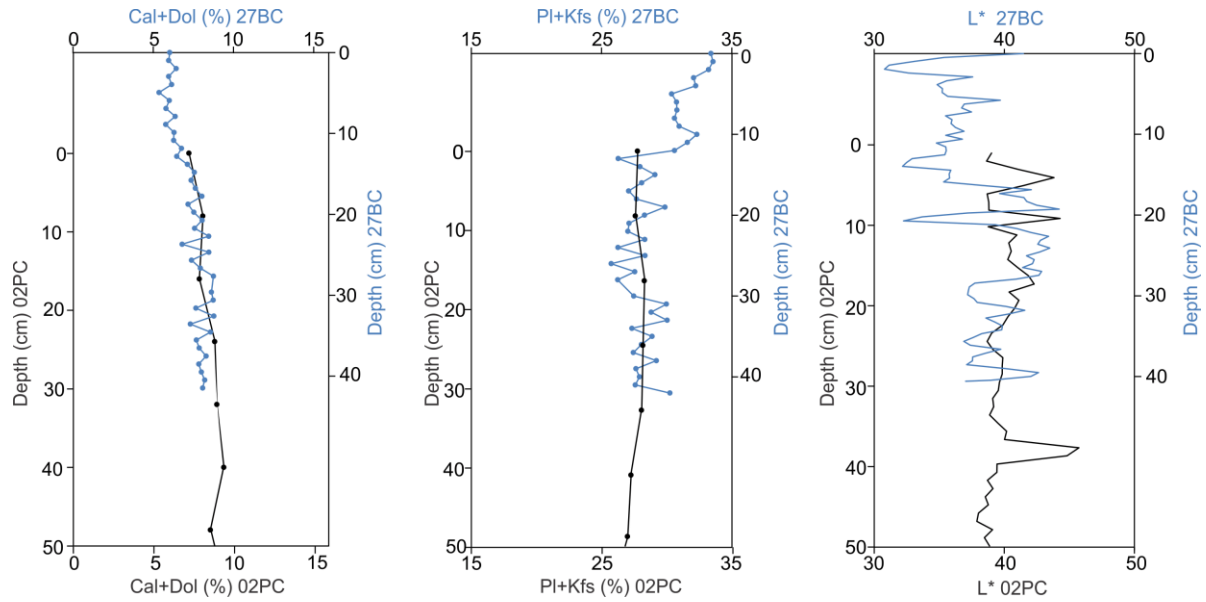


Fig. S1. Correlation of Cal+Dol, Pl+Kfs and L^* between the piston and the box cores (02PC and 27BC, respectively). This correlation indicates that the top 13 cm is missing from 02PC.

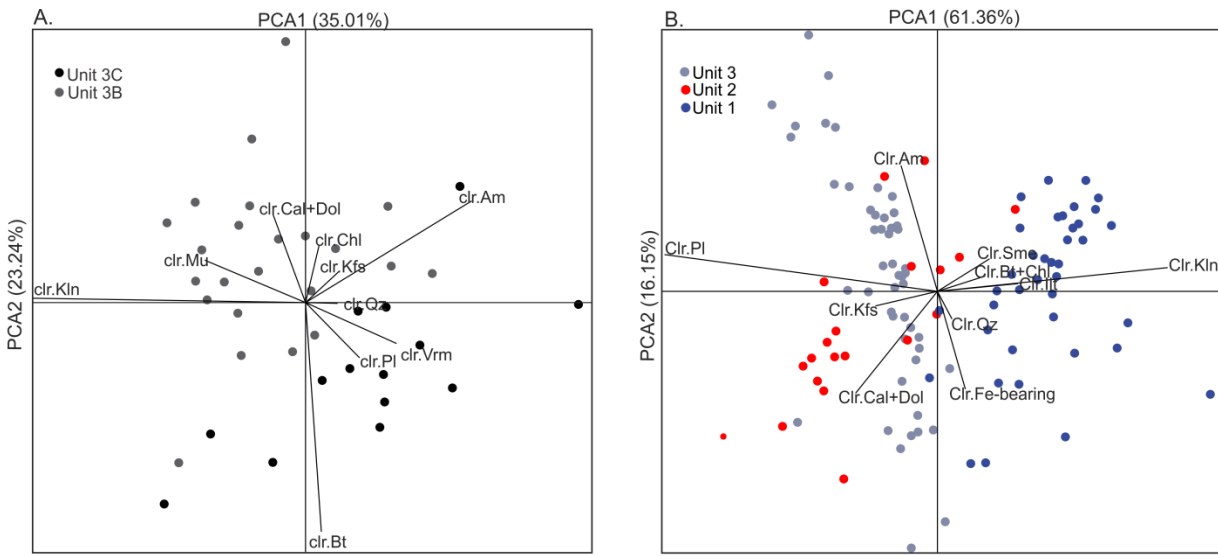


Fig. S2. Biplots of PC1 and PC2 obtained from the log-centered transformation of the mineralogical data from cores (A) 27BC and (B) 02PC. The PCA of 27BC indicates that PC1 (35.01) is positively associated with kaolinite, carbonates (Cal+Dol), biotite, chlorite, smectite, amphibole, K-feldspar and quartz and negatively associated with plagioclase and illite. Whereas PC2 (23.24%) is positively associated with illite, kaolinite and carbonates (Cal+Dol) and negatively associated with plagioclase, amphibole, quartz, K-feldspar, smectite, biotite and chlorite. The mineralogical analysis of 02PC indicates that PC1 (61.36%) is positively associated with clay minerals (smectite, biotite, chlorite, illite and kaolinite), quartz and Fe-bearing minerals and negatively associated with carbonates (Cal+Dol), K-feldspar, amphibolite and plagioclase. PC2 (16.15%) is positively associated with plagioclase, amphibolite and clay minerals and negatively associated with K-feldspar, carbonates (Cal+Dol), quartz and Fe-bearing minerals. The distributions of the PCA based on qXRD data reveal that Unit 3 is associated with plagioclase, K-feldspar, carbonates (Cal+Dol) and Fe-bearing minerals, Unit 2 is associated with plagioclase, K-feldspar, carbonates (Cal+Dol), Fe-bearing minerals and quartz, and Unit 1 is characterized by a high concentration of clay minerals, which suggests a high proportion of fine-grained glaciomarine sediments. Mineral abbreviations: quartz (Qz), K-feldspar (Kfs), plagioclase (Pl), Calcite+Dolomite (Cal+Dol), amphibole (Am), Fe-bearing, kaolinite (Kln), chlorite (Chl), illite (Ill), biotite (Bt), muscovite (Mus), smectite (Sme) and vermiculite (Vrm).

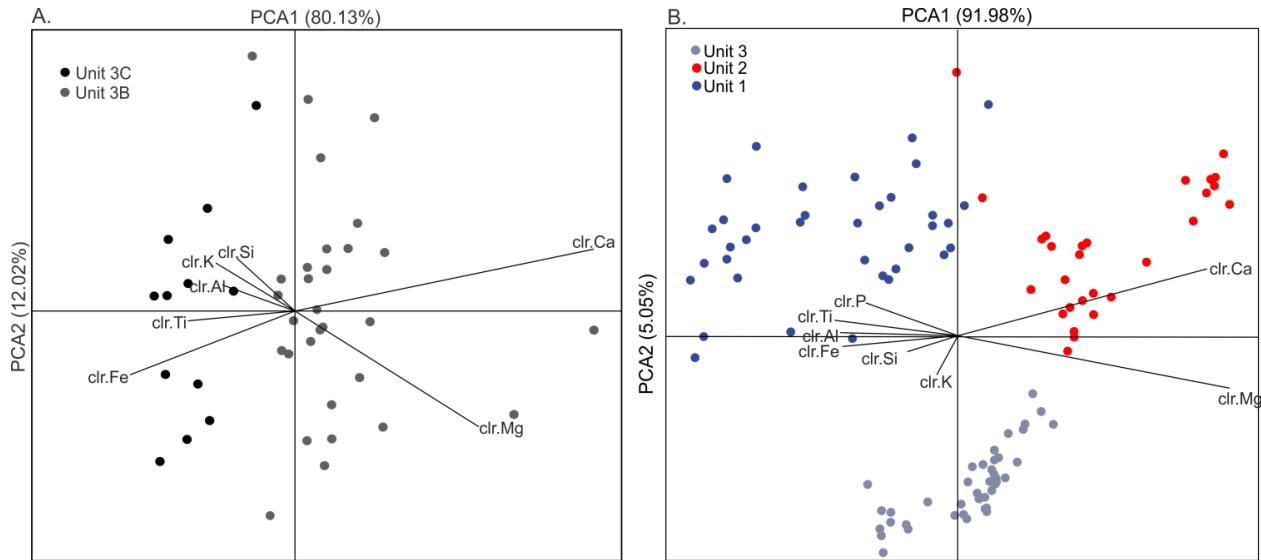


Fig. S3. Biplots of PC1 and PC2 obtained from the log-centered transformation of the elemental data from cores (A) 27BC and (B) 02PC. The PCA (ED-XRF) of 27BC shows that PC1 (80.13%) is positively associated with Ca and Mg and negatively associated with Si, K, Al, Ti and Fe. PC2 (12.02%) is positively associated with Ca, Si, K and Al and negatively associated with Ti, Fe and Mg. The PCA (ED-XRF) of 02PC shows that PC1 (91.98%) is positively associated with Ca and Mg and negatively associated with Mn, P, Ti, Al, Fe, Si and K. PC2 (5.05%) is positively associated with P, Ti and Ca and negatively associated with Al, Fe, Si and K. The distribution of the elemental scores indicated that sediments in Unit 3 are associated with Si, K and Mg and Ca. Unit 2 has a strong association with Mg and Ca, while Unit 1 is enriched in Si, P, Ti, Al and Fe.

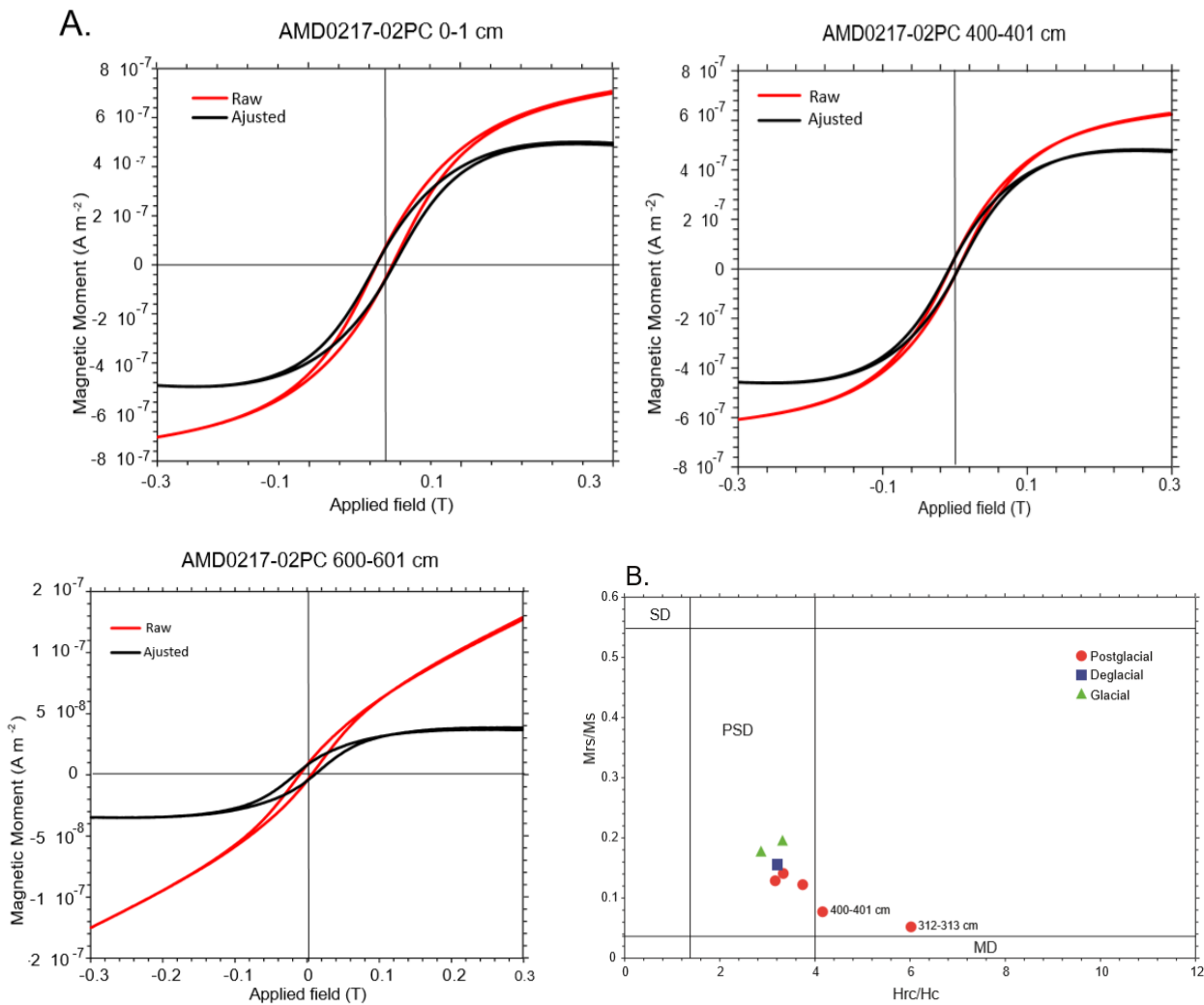


Fig. S4. (A) Hysteresis curves of core 02PC at depths of 0-1 cm, 400-401 cm and 600-601 cm. (B) Day plot showing that a majority of minerals in the pseudo-single domain (PSD) are magnetite or titanomagnetite grains (Day et al. 1977 ; Tauxe 1993). The horizontal and vertical lines delineates the theoretical area for single domain (SD), PSD and MD magnetic grains. There are points outside the theoretical line of the PSD (400 cm and 312 cm).

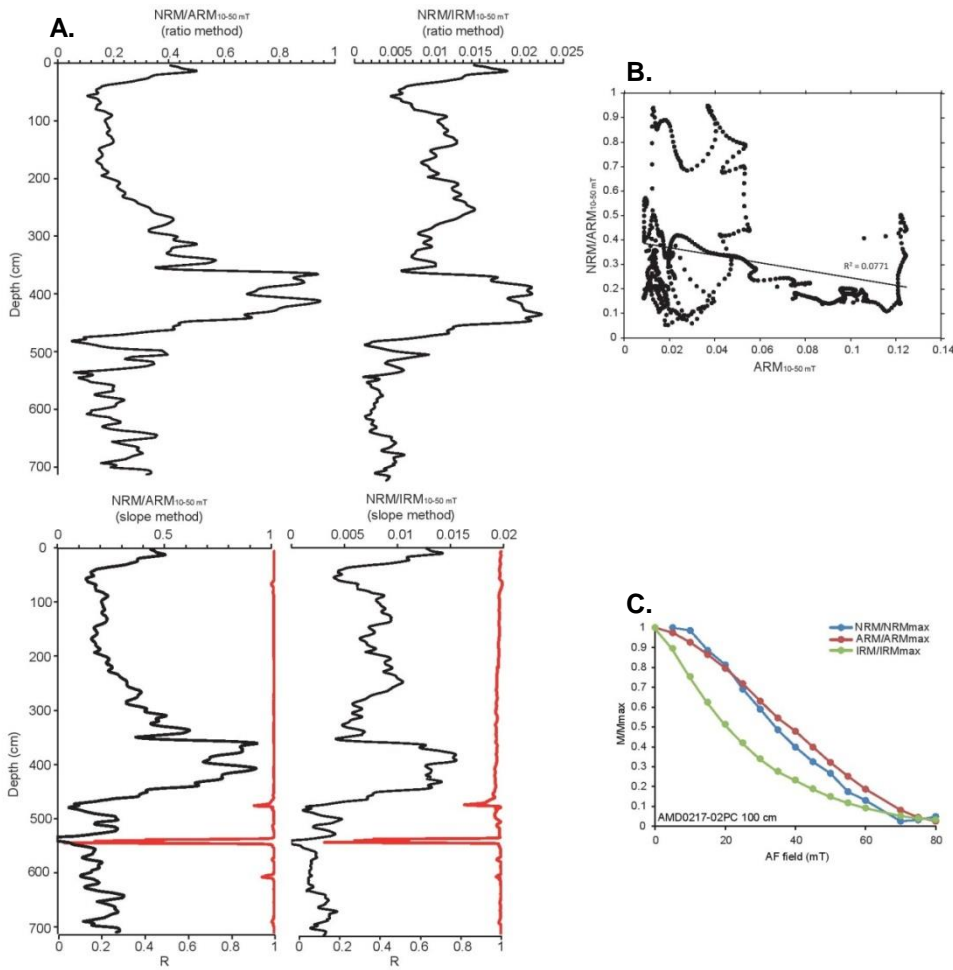


Fig. S5. (A) Comparison of the relative paleointensity (RPI) estimates based on the average ratio method (e.g., Deschamps et al. 2018b ; Caron et al. 2019 ; Channell et al. 2000), which consists of averaging the normalized NRM at different demagnetization steps and the pseudo-Thellier method or the slope method, which uses the best fit slopes of the NRM and the normalizer between different magnetization steps (Tauxe et al. 1995 ; Channell et al. 2002). (B) RPI proxy vs. its normalizer with correlation coefficient. (C) Demagnetization curves for NRM, ARM and IRM suggesting that the magnetic grains that acquire the ARM better mimic the coercivity spectrum of the NRM than the IRM and that the ARM most likely activates the same magnetic assemblage as the NRM. No correlation is shown with the normalizer NRM/ARM ($r^2=0.0771$).

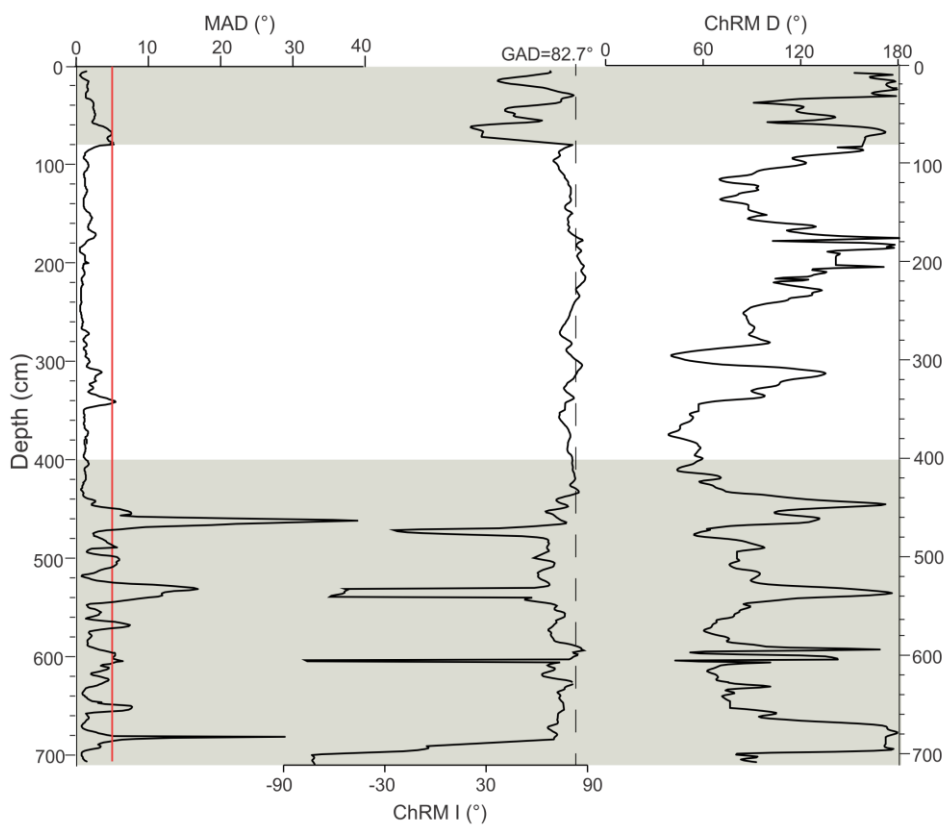


Fig. S6. Downcore variations in magnetic properties for core 02PC. The MAD values are mostly below 5° , the vertical red line delineates a MAD value of 5° , and the ChRM inclination and declination of core 02PC are shown. Unreliable intervals for paleomagnetic reconstruction are highlighted in gray.

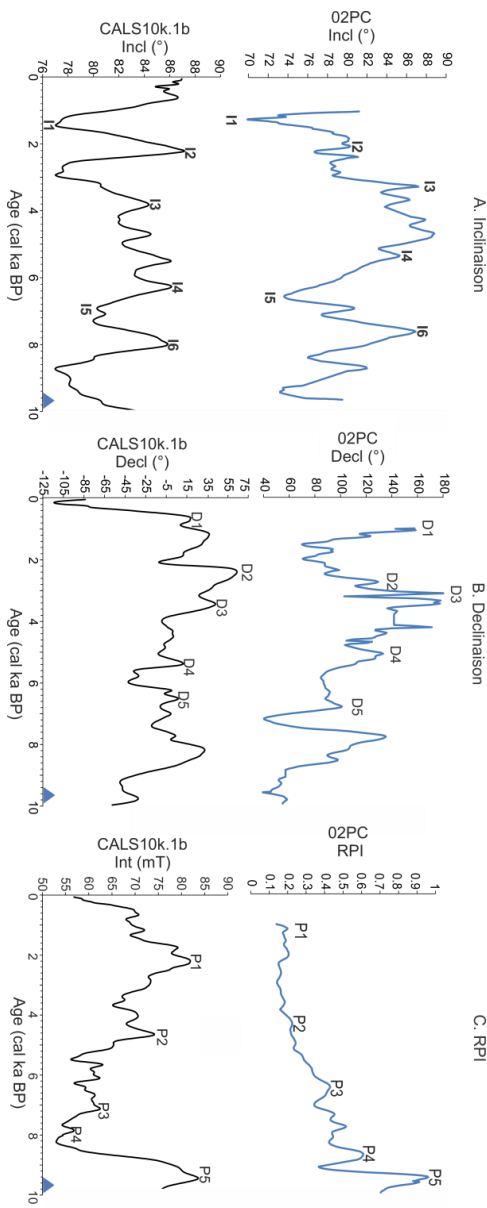


Fig. S7. Full vector paleomagnetic comparison of (A) inclination, (B) declination and (C) relative paleointensity (RPI) in sediment core 02PC and the CALS10k.1b geomagnetic field model (Korte et al., 2011). The blue triangle represents one radiocarbon age determined in this study and used in the age model.

Table S1. Average mineralogical composition of the main sources used in the SedUnMixMC modeling.

Minerals	Canadian Shield		Detrital Carbonates		Weathered Bedrock	
	Average	SD	Average	SD	Average	SD
Quartz	24.1	8.1	10.6	5.0	17.1	10.8
K-feldspar	9.6	1.1	4.6	2.4	10.5	5.4
Plagioclase	24.8	5.8	1.0	0.8	0.0	0.0
Calcite	0.7	1.1	24.9	18.5	0.2	0.4
Dolomite	4.3	2.7	43.6	27.4	0.2	0.1
Amphibole	3.0	0.9	0.8	0.8	0.03	0.1
Kaolinite	0.7	0.6	0.05	0.1	16.3	2.6
Smectite	3.4	2.5	2.6	2.6	9.7	4.3
Illite	8.1	3.9	3.8	2.2	4.8	5.5
Biotite+Chlorite	6.8	4.6	3.6	2.4	10.8	4.1

RÉFÉRENCE S BIBLIOGRAPHIQUES

- Aitchison, J. 1990. Relative variation diagrams for describing patterns of compositional variability. *Mathematical Geology* 22, 487–511.
- Aksu, A. E. 1983. Holocene and Pleistocene dissolution cycles in deep-sea cores of Baffin Bay and Davis Strait: Palaeoceanographic implications. *Marine Geology* 53: 331-348.
- Alley, R. B., S. Anandakrishnan, T. K. Dupont, B. R. Parizek, and D. Pollard. 2007. Effect of Sedimentation on Ice-Sheet Grounding-Line Stability. *Science* 315: 1838.
- Amundsen Science Data Collection. 2017. CTD-Rosette data collected by the CCGS Amundsen in the Canadian Arctic. Arcticnet Inc., Québec, Canada. Processed data. Version 1. Archived at www.polardata.ca, Canadian Cryospheric Information Network (CCIN), Waterloo, Canada. doi: 10.5884/12713. Accessed on 2019/12/03.
- Andresen, C. S., F. Straneo, M. Ribergaard, A. A. Bjørk, A. Kuijpers, and K. H. Kjær. 2013. Using marine sediment archives to reconstruct past outlet glacier variability. *Pages News* 21: 12-13.
- Andrews, J. T. 2000. Icebergs and iceberg rafted detritus (IRD) in the North Atlantic: facts and assumptions. *Oceanography* 13: 100-108.
- Andrews, J., and J. Syvitski. 1994. Sediment fluxes along high latitude glaciated continental margins: Northeast Canada and Eastern Gree. *Material Fluxes on the Surface of the Earth* 7: 99-115.
- Andrews, J. T., G. R. Bigg, and D. J. Wilton. 2014. Holocene ice-rafting and sediment transport from the glaciated margin of East Greenland (67–70°N) to the N Iceland shelves: detecting and modelling changing sediment sources. *Quaternary Science Reviews* 91: 204-217.
- Andrews, J. T., and D. D. Eberl. 2012. Determination of sediment provenance by unmixing the mineralogy of source-area sediments: The “SedUnMix” program. *Marine Geology* 291-294: 24-33.

- Andrews, J. T., M. E. Kirby, A. Aksu, D. C. Barber, and D. Meese. 1998. Late Quaternary detrital carbonate (DC-) layers in Baffin Bay marine sediment (67° – 74° N): correlation with Heinrich events in the north atlantic? *Quaternary Science Reviews* 17: 1125-1137.
- Andrews, J. T., A. J. Klein, K. A. Jenner, A. E. Jennings, and C. Campbell. 2018. The variability of Baffin Bay seafloor sediment mineralogy: the identification of discrete glacial sediment sources and application to Late Quaternary downcore analysis. *Canadian Journal of Earth Sciences* 55: 620-639.
- Andrews, J. T., R. Stein, M. Moros, and K. Perner. 2016. Late Quaternary changes in sediment composition on the NE Greenland margin ($\sim 73^{\circ}$ N) with a focus on the fjords and shelf. *Boreas* 45: 381-397.
- Appleby, P. G., and F. Oldfieldz. 1983. The assessment of ^{210}Pb data from sites with varying sediment accumulation rates. *Hydrobiologia* 103: 29-35.
- Azetsu-Scott, K., A. Clarke, K. Falkner, J. Hamilton, E.P. Jones, C. Lee, B. Petrie, S. Prinsenberg, M. Starr, and P. Yeats. 2010. Calcium carbonate saturation states in the waters of the Canadian Arctic Archipelago and the Labrador Sea. *Journal of Geophysical Research: Oceans* 115: 1-18.
- Bailey, J. N. L., R. W. Macdonald, H. Sanei, P. M. Outridge, S. C. Johannessen, K. Hochheim, D. Barber, and G. A. Stern. 2013. Change at the margin of the North Water Polynya, Baffin Bay, inferred from organic matter records in dated sediment cores. *Marine Geology* 341: 1-13.
- Batchelor, C. L., J. A. Dowdeswell, E. K. Dowdeswell, B. J. Todd, and M. J. Sharp. 2016. A tidewater glacier landform assemblage in Belcher Inlet, Canadian Arctic. *Geological Society, London, Memoirs* 46: 155-158.
- Belkin, I. M., S. Levitus, J. Antonov, and S.-A. Malmberg. 1998. “Great Salinity Anomalies” in the North Atlantic. *Progress in Oceanography* 41: 1-68.
- Blaauw, M., and J. A. Christen. 2011. Flexible paleoclimate age-depth models using an autoregressive gamma process. *Bayesian Analysis* 6: 457-474.

- Blott, S. J., and K. Pye. 2001. GRADISTAT: a grain size distribution and statistics package for the analysis of unconsolidated sediments. *Earth Surface Processes and Landforms* 26: 1237-1248.
- Bradley, R. S., M. K. Hughes, and H. F. Diaz. 2003. Climate in Medieval Time. *Science* 302: 404-405.
- Briner, J. P., A. C. Bini, and R. S. Anderson. 2009. Rapid early Holocene retreat of a Laurentide outlet glacier through an Arctic fjord. *Nature Geoscience* 2: 496-499.
- Briner, J. P., N. P. McKay, Y. Axford, O. Bennike, R. S. Bradley, A. de Vernal, D. Fisher, P. Francus, B. Fréchette, K. Gajewski, A. Jennings, D. S. Kaufman, G. Miller, C. Rouston, and B. Wagner. 2016. Holocene climate change in Arctic Canada and Greenland. *Quaternary Science Reviews* 147: 340-364.
- Burgess, D. O., and M. J. Sharp. 2004. Recent Changes in Areal Extent of the Devon Ice Cap, Nunavut, Canada. *Arctic, Antarctic, and Alpine Research* 36: 261-271.
- Caron, M., J.-C. Montero-Serrano, G. St-Onge, and A. Rochon. 2020. Quantifying Provenance and Transport Pathways of Holocene Sediments From the Northwestern Greenland Margin. *Paleoceanography and Paleoclimatology* 35: e2019PA003809.
- Caron, M., A. Rochon, J. C. Montero-Serrano, and G. St-Onge. 2019. Evolution of sea-surface conditions on the northwestern Greenland margin during the Holocene. *Journal of Quaternary Science* 34: 569-580.
- Caron, M., G. St-Onge, J.-C. Montero-Serrano, A. Rochon, E. Georgiadis, J. Giraudeau and G. Massé. 2018. Holocene chronostratigraphy of northeastern Baffin Bay based on radiocarbon and palaeomagnetic data. *Boreas* 48: 147-165.
- Casse, M., J.-C. Montero-Serrano, and G. St-Onge. 2017. Influence of the Laurentide Ice Sheet and relative sea-level changes on sediment dynamics in the Estuary and Gulf of St. Lawrence since the last deglaciation. *Boreas* 46: 541-561.
- Channell, J. E. T., A. Mazaud, P. Sullivan, S. Turner, and M. E. Raymo. 2002. Geomagnetic excursions and paleointensities in the Matuyama Chron at Ocean Drilling Program Sites 983 and 984 (Iceland Basin). *Journal of Geophysical Research: Solid Earth* 107: EPM 1-1-EPM 1-14.

- Channell, J. E. T., J. S. Stoner, D. A. Hodell, and C. D. Charles. 2000. Geomagnetic paleointensity for the last 100 kyr from the sub-antarctic South Atlantic: a tool for inter-hemispheric correlation. *Earth and Planetary Science Letters* 175: 145-160.
- Clark, P. U., J. D. Shakun, S. A. Marcott, A. C. Mix, M. Eby, S. Kulp, A. Levermann, G. A. Milne, P. L. Pfister, B. D. Santer, D. P. Schrag, S. Solomon, T. F. Stocker, B. H. Strauss, A. J. Weaver, R. Winkelmann, D. Archer, E. Bard, A. Goldner, K. Lambeck, R. T. Pierrehumbert, and G. K. Plattner. 2016. Consequences of twenty-first-century policy for multi-millennial climate and sea-level change. *Nature Climate Change* 6: 360-369.
- Cofaigh, C., J. Taylor, J. Dowdeswell, and C. Pudsey. 2003. Palaeo-ice streams, trough mouth fans and high-latitude continental slope sedimentation. *Boreas* 32: 37-55.
- Comas-Cufí, M., S. Henestrosa. 2011. Codapack 2.0: A Stand-Alone, Multi-Platform Compositional Software. *CoDaWork'11: 4th International Workshop on Compositional Data Analysis*.
- Cook, A. J., L. Copland, B. P. Y. Noël, C. R. Stokes, M. J. Bentley, M. J. Sharp, R. G. Bingham, and M. R. van den Broeke. 2019. Atmospheric forcing of rapid marine-terminating glacier retreat in the Canadian Arctic Archipelago. *Science Advances* 5: eaau8507.
- Cormier, M.-A., A. Rochon, A. de Vernal, and Y. Gélinas. 2016. Multi-proxy study of primary production and paleoceanographical conditions in northern Baffin Bay during the last centuries. *Marine Micropaleontology* 127: 1-10.
- Coulthard, R. D., M. F. A. Furze, A. J. Pieńkowski, F. Chantel Nixon, and J. H. England. 2010. New marine ΔR values for Arctic Canada. *Quaternary Geochronology* 5: 419-434.
- Crespin, E., H. Goosse, T. Fichefet, and M. E. Mann. 2009. The 15th century Arctic warming in coupled model simulations with data assimilation. *Clim. Past* 5: 389-401.
- Curry, R., C. Mauritzen. 2005. Dilution of the Northern North Atlantic Ocean in Recent Decades. *Science*, 308(5729), 1772.

- Dalton, A. S. and others 2020. An updated radiocarbon-based ice margin chronology for the last deglaciation of the North American Ice Sheet Complex. *Quaternary Science Reviews* 234: 106223.
- D'Andrea, W. J., D. A. Vailencourt, N. L. Balascio, A. Werner, S. R. Roof, M. Retelle, and R. S. Bradley. 2012. Mild Little Ice Age and unprecedented recent warmth in an 1800 year lake sediment record from Svalbard. *Geology* 40: 1007-1010.
- Dankers, P. 1981: Relationship between median destructive field and remanent coercive forces for dispersed natural magnetite, titanomagnetite and hematite. *Geophysical Journal of the Royal Astronomical Society* 64, 447–461.
- Darby, D. A., L. Polyak, and H. A. Bauch. 2006. Past glacial and interglacial conditions in the Arctic Ocean and marginal seas – a review. *Progress in Oceanography* 71: 129-144.
- Day, R., M. Fuller, and V. A. Schmidt. 1977. Hysteresis properties of titanomagnetites: Grain-size and compositional dependence. *Physics of the Earth and Planetary Interiors* 13: 260-267.
- de Vernal, A., G. Bilodeau, C. Hillaire-Marcel, and N. Kassou. 1992. Quantitative assessment of carbonate dissolution in marine sediments from foraminifer linings vs. shell ratios: Davis Strait, northwest North Atlantic. *Geology* 20: 527-530.
- Deschamps, C.-E., J.-C. Montero-Serrano, and G. St-Onge. 2018. Sediment Provenance Changes in the Western Arctic Ocean in Response to Ice Rafting, Sea Level, and Oceanic Circulation Variations Since the Last Deglaciation. *Geochemistry, Geophysics, Geosystems* 19: 2147-2165.
- Deschamps, C.-E., G. St-Onge, J.-C. Montero-Serrano, and L. Polyak. 2018. Chronostratigraphy and spatial distribution of magnetic sediments in the Chukchi and Beaufort seas since the last deglaciation. *Boreas* 47: 544-564.
- Dietze, E., K. Hartmann, B. Diekmann, J. Ijmker, F. Lehmkuhl, S. Opitz, G. Stauch, B. Wünnemann, and A. Borchers. 2012. An end-member algorithm for deciphering modern detrital processes from lake sediments of Lake Donggi Cona, NE Tibetan Plateau, China. *Sedimentary Geology* 243-244: 169-180.

- Dong, L., Y. Liu, X. Shi, L. Polyak, Y. Huang, X. Fang, J. Liu, J. Zou, K. Wang, F. Sun, and X. Wang. 2017. Sedimentary record from the Canada Basin, Arctic Ocean: implications for late to middle Pleistocene glacial history. *Clim. Past* 13: 511-531.
- Dowdeswell, J. A., T. J. Benham, M. R. Gorman, D. Burgess, and M. J. Sharp. 2004. Form and flow of the Devon Island Ice Cap, Canadian Arctic. *Journal of Geophysical Research: Earth Surface* 109: F02002.
- Dowdeswell, J. A., K. A. Hogan, N. S. Arnold, R. I. Mugford, M. Wells, J. P. P. Hirst, and C. Decalf. 2015. Sediment-rich meltwater plumes and ice-proximal fans at the margins of modern and ancient tidewater glaciers: Observations and modelling. *Sedimentology* 62: 1665-1692.
- Dunbar, M., and M. J. Dunbar. 1972. 21. The History of the North Water. *Proceedings of the Royal Society of Edinburgh. Section B. Biology* 72: 231-241.
- Dyke, A. S. 1998. Holocene delevelling of Devon Island, Arctic Canada: implications for ice sheet geometry and crustal response. *Canadian Journal of Earth Sciences* 35: 885-904.
- Dyke, A. 1999. Last Glacial Maximum and deglaciation of devon island, arctic canada: support for an innuitian ice sheet. *Quaternary Science Reviews* 18: 393-420.
- Dyke, A., and D. Evans. 2003. Ice-marginal terrestrial landsystems: northern Laurentide and Innuitian ice sheel margins, p. 143-165.
- Dyke, A. S., J. T. Andrews, P. U. Clark, J. H. England, G. H. Miller, J. Shaw, and J. J. Veillette. 2002. The Laurentide and Innuitian ice sheets during the Last Glacial Maximum. *Quaternary Science Reviews* 21: 9-31.
- Eberl, D. D. 2003. User guide to RockJock—A program for determining quantitative mineralogy from X-ray diffraction data. *USGS Open File Report* 40: 03-78.
- England, J., N. Atkinson, J. Bednarski, A. S. Dyke, D. A. Hodgson, and C. Ó Cofaigh. 2006. The Innuitian Ice Sheet: configuration, dynamics and chronology. *Quaternary Science Reviews* 25: 689-703.
- England, J. H., T. R. Lakeman, D. S. Lemmen, J. M. Bednarski, T. G. Stewart, and D. J. A. Evans. 2008. A millennial-scale record of Arctic Ocean sea ice variability and the

- demise of the Ellesmere Island ice shelves. *Geophysical Research Letters* 35: L19502
- Fisher, D. A., R. M. Koerner, W. S. B. Paterson, W. Dansgaard, N. Gundestrup, and N. Reeh. 1983. Effect of wind scouring on climatic records from ice-core oxygen-isotope profiles. *Nature* 301: 205-209.
- Fisher, D., J. Zheng, D. Burgess, C. Zdanowicz, C. Kinnard, M. Sharp, and J. Bourgeois. 2012. Recent melt rates of Canadian arctic ice caps are the highest in four millennia. *Global and Planetary Change* 84-85: 3-7.
- Fogel, M. L., and L. A. Cifuentes. 1993. Isotope Fractionation during Primary Production, p. 73-98. *In* M. H. Engel and S. A. Macko [eds.], *Organic Geochemistry: Principles and Applications*. Springer US.
- Frisch, T. 1988. Reconnaissance geology of the Precambrian Shied of Ellesmere, Devon and Coburg islands, Canadian Arctic Archipelago, Commission géologique du Canada, Memoir 409: 102p.
- Gajewski, K. 2015. Quantitative reconstruction of Holocene temperatures across the Canadian Arctic and Greenland. *Global and Planetary Change* 128: 14-23.
- Gamboa, A., J.-C. Montero-Serrano, G. St-Onge, A. Rochon, and P.-A. Desiage. 2017. Mineralogical, geochemical, and magnetic signatures of surface sediments from the Canadian Beaufort Shelf and Amundsen Gulf (Canadian Arctic). *Geochemistry, Geophysics, Geosystems* 18: 488-512.
- Gardner, A., G. Moholdt, A. Arendt, and B. Wouters. 2012. Accelerated contributions of Canada's Baffin and Bylot Island glaciers to sea level rise over the past half century. *The Cryosphere* 6: 1103-1125.
- Georgiadis, E., J. Giraudeau, P. Martinez, P. Lajeunesse, G. St-Onge, S. Schmidt, and G. Massé. 2018. Deglacial to postglacial history of Nares Strait, Northwest Greenland: a marine perspective from Kane Basin. *Clim. Past* 14: 1991-2010.
- Ghaleb, B. 2009. Overview of the methods for the measurement and interpretation of short-lived radioisotopes and their limits. *IOP Conference Series: Earth and Environmental Science* 5: 012007.

- Gilbert, R. 1982. Contemporary Sedimentary Environments on Baffin Island, N.W.T., Canada: Glaciomarine Processes in Fiords of Eastern Cumberland Peninsula. *Arctic and Alpine Research* 14: 1-12.
- Grove, H. 1987. A Simple Method for the Determination of Ice-Rafted Debris in Sediment Cores*. *Polarforschung* 57 (3): 123-126.
- Harrison, J. C., T. A. Brent, and G. N. Oakey. 2011. Chapter 40 Baffin Fan and its inverted rift system of Arctic eastern Canada: stratigraphy, tectonics and petroleum resource potential. *Geological Society, London, Memoirs* 35: 595-626.
- Heaton, T. J., P. Köhler, M. Butzin, E. Bard, R.W. Reimer, W. Austin, C. Bronk Ramsey, P.M. Grootes, K.A. Hughen, B. Kromer, P.J. Reimer, J. Adkins, A. Burke, M.S. Cook, J. Olsen, and L.C. Skinner. 2020. Marine20—The Marine Radiocarbon Age Calibration Curve (0–55,000 cal BP). *Radiocarbon* 62: 779-820.
- Hiscott, R., A. E. Aksu, and O. Nielsen. 1989. Provenance and Dispersal Patterns, Pliocene-Pleistocene Section at Site 645, Baffin Bay. Proc., scientific results, ODP, Leg 105, Baffin Bay and Labrador Sea: 31-52.
- Hodson, D. L. R., S. P. E. Keeley, A. West, J. Ridley, E. Hawkins, and H. T. Hewitt. 2012. Identifying uncertainties in Arctic climate change projections. *Climate Dynamics* 40: 2849-2865.
- Holland, D. M., R. H. Thomas, B. de Young, M. H. Ribergaard, and B. Lyberth. 2008. Acceleration of Jakobshavn Isbræ triggered by warm subsurface ocean waters. *Nature Geoscience* 1: 659-664.
- IPCC, 2014: Climate Change 2014: Synthesis Report. Contribution of Working Groups I, II and III to the Fifth Assessment Report of the Intergovernmental Panel on Climate Change [Core Writing Team, R.K. Pachauri and L.A. Meyer (eds.)]. IPCC, Geneva, Switzerland, 151 pp.
- IPCC, 2019. Special Report on the Ocean and Cryosphere in a Changing Climate (SROCC). 1170 p.

- Jenner, K. A., D. C. Campbell, and D. J. W. Piper. 2018. Along-slope variations in sediment lithofacies and depositional processes since the Last Glacial Maximum on the northeast Baffin margin, Canada. *Marine Geology* 405: 92-107.
- Jennings, A. 1993. The Quaternary History of Cumberland Sound, Southeastern Baffin Island: The Marine Evidence. *Géographie physique et Quaternaire* 47: 21-42.
- Jennings, A. E., J. T. Andrews, B. Oliver, M. Walczak, and A. Mix. 2019. Retreat of the Smith Sound Ice Stream in the Early Holocene. *Boreas* 48: 825-840.
- Jennings, A. E., C. Sheldon, T. M. Cronin, P. Francus, J. Stoner, and J. Andrews. 2011. The Holocene history of Nares strait Transition from Glacial Bay to Arctic-Atlantic Throughflow. *Oceanography* 24: 26-41.
- Jones, P. D., and M. E. Mann. 2004. Climate over past millennia. *Reviews of Geophysics* 42: RG2002.
- Jones, E. P., J. H. Swift, L. G. Anderson, M. Lipizer, G. Civitarese, K. K. Falkner, G. Kattner, and F. McLaughlin. 2003. Tracing Pacific water in the North Atlantic Ocean. *Journal of Geophysical Research: Oceans* 108: 3118.
- Kaufman, D. S., D. P. Schneider, N. P. McKay, C. M. Ammann, R. S. Bradley, K. R. Briffa, G. H. Miller, B. L. Otto-Bliesner, J. T. Overpeck, and B. M. Vinther. 2009. Recent warming reverses long-term arctic cooling. *Science* 325: 1236-1239.
- Keen, C.E., D.L. Barrett 1973. Structural Characteristics of some Sedimentary Basins in Northern Baffin Bay. *Canadian Journal of Earth Sciences*, 10(8), 1267-1278.
- Kinnard, C., C. M. Zdanowicz, D. A. Fisher, E. Isaksson, A. de Vernal, and L. G. Thompson. 2011. Reconstructed changes in Arctic sea ice over the past 1,450 years. *Nature* 479: 509-512.
- Kirschvink, J. L. 1980. The least-squares line and plane and the analysis of palaeomagnetic data. *Geophysical Journal International* 62: 699-718.
- Knudsen, K. L., B. Stabell, M.-S. Seidenkrantz, J. EirÍKsson, and W. Blake. 2008. Deglacial and Holocene conditions in northernmost Baffin Bay: sediments, foraminifera, diatoms and stable isotopes. *Boreas* 37: 346-376.

- Koerner, R. M. 1977. Devon Island Ice Cap: Core Stratigraphy and Paleoclimate. *Science* 196: 15-18.
- Korte, M., C. Constable, F. Donadini, and R. Holme. 2011. Reconstructing the Holocene geomagnetic field. *Earth and Planetary Science Letters* 312: 497-505.
- Lapointe, F., R. S. Bradley, P. Francus, N. L. Balascio, M. B. Abbot, J. S. Stoner, G. St-Onge, A. De Coninck, and T. Labarre. 2020. Annually resolved Atlantic sea surface temperature variability over the past 2,900 y. *Proceedings of the National Academy of Sciences* 117: 27171.
- Laskar, J., P. Robutel, F. Joutel, M. Gastineau, A.C.M. Correia, and B. Levrard. 2004. A long-term numerical solution for the insolation quantities of the Earth. *Astronomy & Astrophysics* 428:261-285.
- Lecavalier, B. S., D. A. Fisher, G. A. Milne, B. M. Vinther, L. Tarasov, P. Huybrechts, D. Lacelle, B. Main, J. Zheng, J. Bourgeois, and A. S. Dyke. 2017. High Arctic Holocene temperature record from the Agassiz ice cap and Greenland ice sheet evolution. *Proceedings of the National Academy of Sciences* 114: 5952-5957.
- Ledu, D., A. Rochon, A. de Vernal, and G. St-Onge. 2010. Holocene paleoceanography of the northwest passage, Canadian Arctic Archipelago. *Quaternary Science Reviews* 29: 3468-3488.
- Lévesque, Y., St-Onge, G., Lajeunesse, P., Desiage, P.-A., Brouard, É. 2020. Defining the maximum extent of the Laurentide Ice Sheet in Home Bay cross-shelf trough during the Last glacial episode. *Boreas* 49, 52-70.
- Luckman, A., D. I. Benn, F. Cottier, S. Bevan, F. Nilsen, and M. Inall. 2015. Calving rates at tidewater glaciers vary strongly with ocean temperature. *Nature communications* 6: 8566.
- Lyn Lewis, E., D. Ponton, L. Legendre, and B. Leblanc. 1996. Springtime sensible heat, nutrients and phytoplankton in the Northwater Polynya, Canadian Arctic. *Continental Shelf Research* 16: 1775-1792.

- MacLean, B., Woodside,J.M.& Giroud, P. 1984. Geological and geophysical investigations in Jones Sound, District of Franklin. Geological Survey of Canada Papers, 84-1A, 359–365.
- Mair, D. 2005. Thirty-seven year mass balance of Devon Ice Cap, Nunavut, Canada, determined by shallow ice coring and melt modeling. *Journal of Geophysical Research* 110: F01011.
- Marlowe, J. I. 1966. Mineralogy as an indicator of long-term current fluctuations in Baffin Bay. *Canadian Journal of Earth Sciences* 3: 191-201.
- Marzeion, B., A. H. Jarosch, and M. Hofer. 2012. Past and future sea-level change from the surface mass balance of glaciers. *The Cryosphere* 6: 1295-1322.
- Mazaud, A. 2005: User-friendly software for vector analysis of the magnetization of long sediment cores. *Geochemistry, Geophysics, Geosystems* 6: Q12006,
- McNeely, R., Dyke, A.S., Southon, J., 2006. Canadian Marine Reservoir Ages: Preliminary Data Assessment. Geological Survey of Canada. Open File 5049.
- Meyers, P. A. 1994. Preservation of elemental and isotopic source identification of sedimentary organic matter. *Chemical Geology* 114: 289-302.
- Montero-Serrano, J-C and J. Brossard. 2019. Collecting sedimentary sequences and plankton samples in the continental margins from the eastern Canadian Arctic Archipelago. ArcticNet Leg 2b Cruise Report - CCGS Amundsen expedition (25 July to 15 August 2019). ArcticNet, 22 p.
- Montero-Serrano, J-C, J. Brossard, A. Corminboeuf. 2018. Collecting sedimentary sequences for paleoclimate, paleoceanographic and environmental studies in the eastern Canadian Arctic Archipelago and Baffin Bay. ArcticNet Leg 3 Cruise Report - CCGS Amundsen expedition (16 August to 9 September). ArcticNet 14 p.
- Montero-Serrano J.-C, Furze M. Zindorf, and M. Pienkowski. 2017. The marine sedimentary record of paleoclimate, paleoceanography, and deglacial history in the eastern Canadian Arctic Archipelago and Northern and Eastern Baffin Bay. ArcticNet Leg 2b Cruise Report - CCGS Amundsen expedition (13 July to 17 August). ArcticNet. 40 p.

- Montero-Serrano, J.-C., K. B. Föllmi, T. Adatte, J. E. Spangenberg, N. Tribovillard, A. Fantasia, and G. Suan. 2015. Continental weathering and redox conditions during the early Toarcian Oceanic Anoxic Event in the northwestern Tethys: Insight from the Posidonia Shale section in the Swiss Jura Mountains. *Palaeogeography, Palaeoclimatology, Palaeoecology* 429: 83-99.
- Montero-Serrano, J. C., V. Bout-Roumazeilles, T. Sionneau, N. Tribovillard, A. Bory, B. P. Flower, A. Riboulleau, P. Martinez, and I. Billy. 2010. Changes in precipitation regimes over North America during the Holocene as recorded by mineralogy and geochemistry of Gulf of Mexico sediments. *Global and Planetary Change* 74: 132-143.
- Montero-Serrano, J. C., V. Bout-Roumazeilles, N. Tribovillard, T. Sionneau, A. Riboulleau, A. Bory, and B. Flower. 2009. Sedimentary evidence of deglacial megafloods in the northern Gulf of Mexico (Pigmy Basin). *Quaternary Science Reviews* 28: 3333-3347.
- Montero-Serrano, J. C., J. Palarea-Albaladejo, J. A. Martín-Fernández, M. Martínez-Santana, and J. V. Gutiérrez-Martín. 2010. Sedimentary chemofacies characterization by means of multivariate analysis. *Sedimentary Geology* 228: 218-228.
- Moore, J. J., K. A. Hughen, G. H. Miller, and J. T. Overpeck. 2001. Little Ice Age recorded in summer temperature reconstruction from varved sediments of Donard Lake, Baffin Island, Canada. *Journal of Paleolimnology* 25: 503-517.
- Motyka, R. J., M. Truffer, M. Fahnestock, J. Mortensen, S. Rysgaard, and I. Howat. 2011. Submarine melting of the 1985 Jakobshavn Isbræ floating tongue and the triggering of the current retreat. *Journal of Geophysical Research: Earth Surface* 116.
- Mudie, P. J., and F. M. G. McCarthy. 2006. Marine palynology: potentials for onshore—offshore correlation of Pleistocene—Holocene records. *Transactions of the Royal Society of South Africa* 61: 139-157.

Neatby, Leslie H. et Peter Kikkert. "Exploration de l'Arctique". *l'Encyclopédie Canadienne*, 14 juillet 2016, Historica Canada.
<https://www.thecanadianencyclopedia.ca/fr/article/arctique-exploration-de-l>.

Noël, B., W. J. van de Berg, S. Lhermitte, B. Wouters, N. Schaffer, and M. R. van den Broeke. 2018. Six Decades of Glacial Mass Loss in the Canadian Arctic Archipelago. *Journal of Geophysical Research: Earth Surface* 123: 1430-1449.

Oldfield, F., and P. G. Appleby. 1984. A combined radiometric and mineral magnetic approach to recent geochronology in lakes affected by catchment disturbance and sediment redistribution. *Chemical Geology* 44: 67-83.

Ó Cofaigh, C., J. A. Dowdeswell, A. E. Jennings, K. A. Hogan, A. Kilfeather, J. F. Hiemstra, R. Noormets, J. Evans, D. J. McCarthy, J. T. Andrews, J. M. Lloyds, and M. Moros. 2013. An extensive and dynamic ice sheet on the West Greenland shelf during the last glacial cycle. *Geology* 41: 219-222.

Perner, K., M. Moros, J. M. Lloyd, A. Kuipers, R. J. Telford, and J. Harff. 2011. Centennial scale benthic foraminiferal record of late Holocene oceanographic variability in Disko Bugt, West Greenland. *Quaternary Science Reviews* 30: 2815-2826.

Perry, R. B. 1961. A study of the marine sediments of the Canadian eastern Arctic Archipelago, Fisheries Research Board of Canada, Manuscript Report 89, 80p.

Peterson, B. J., and R. W. Howarth. 1987. Sulfur, carbon, and nitrogen isotopes used to trace organic matter flow in the salt-marsh estuaries of Sapelo Island, Georgia. *Limnology and Oceanography* 32: 1195-1213.

Polyak, L., J. Bischof, J. D. Ortiz, D. A. Darby, J. E. T. Channell, C. Xuan, D. S. Kaufman, R. Lovlie, D. A. Schneider, D. D. Eberl, R. E. Adler, and E. A. Council. 2009. Late Quaternary stratigraphy and sedimentation patterns in the western Arctic Ocean. *Global and Planetary Change* 68: 5-17.

Polyak, L., S. Korsun, L. A. Febo, V. Stanovoy, T. Khusid, M. Hald, B. E. Paulsen, and D. J. Lubinski. 2002. Benthic foraminiferal assemblages from the southern Kara sea, a

- river-influenced arctic marine environnement. *Journal of Foraminiferal Research* 32: 252-273.
- Powell, R. D. 1981. A Model for Sedimentation by Tidewater Glaciers. *Annals of Glaciology* 2: 129-134.
- Prins, M. & Weltje, G.J. 1999: End-member modelling of siliciclastic grain-size distributions: the late Quaternary record of eolian and fluvial sediment supply to the Arabian Sea and its paleoclimatic significance. *SEPM, Special Publication* 62, 91-111.
- Reilly, B. T., J. S. Stoner, A. C. Mix, M. H. Walczak, A. Jennings, M. Jakobsson, L. Dyke, A. Glueder, K. Nicholls, K. A. Hogan, L. A. Mayer, R. G. Hatfield, S. Albert, S. Marcott, S. Fallon, and M. Cheseby. 2019. Holocene break-up and reestablishment of the Petermann Ice Tongue, Northwest Greenland. *Quaternary Science Reviews* 218: 322-342.
- Rochon, A., and A. d. Vernal. 1994. Palynomorph distribution in Recent sediments from the Labrador Sea. *Canadian Journal of Earth Sciences* 31: 115-127.
- Røthe, T. O., J. Bakke, E. W. N. Støren, and R. S. Bradley. 2018. Reconstructing Holocene Glacier and Climate Fluctuations From Lake Sediments in Vårfluesjøen, Northern Spitsbergen. *Frontiers in Earth Science* 6: 91.
- Serreze, M. C., and J. A. Francis. 2006. The Arctic Amplification Debate. *Climatic Change* 76: 241-264.
- Serreze, M. C., A. P. Barrett, A. G. Slater, R. A. Woodgate, K. Aagaard, R. B. Lammers, M. Steele, R. Mortiz, M. Meredith, and C. M. Lee. 2006. The large-scale freshwater cycle of the Arctic. *Journal of Geophysical Research: Oceans* 111: C11010.
- Shepherd, A., Z. Du, T. J. Benham, J. A. Dowdeswell, and E. M. Morris. 2007. Mass balance of Devon Ice Cap, Canadian Arctic. *Annals of Glaciology* 46: 249-254.
- Sharp, M., D. O. Burgess, J. G. Cogley, M. Ecclestone, C. Labine, and G. J. Wolken. 2011. Extreme melt on Canada's Arctic ice caps in the 21st century. *Geophysical Research Letters* 38: L11501.

- Simon Q. 2013. Propriétés magnétiques, minéralogiques et sédimentologique des sédiments profond de la baie de Baffin: chronologie et dynamique des glaciers ouest groenlandais, innuitiens et laurentidiens au cours de la dernière glaciation. PhD Thesis, Université du Québec à Montréal.
- Simon, Q., C. Hillaire-Marcel, G. St-Onge, and J. T. Andrews. 2014. North-eastern Laurentide, western Greenland and southern Innuitian ice stream dynamics during the last glacial cycle. *Journal of Quaternary Science* 29: 14-26.
- Simon, Q., G. St-Onge, and C. Hillaire-Marcel. 2012. Late Quaternary chronostratigraphic framework of deep Baffin Bay glaciomarine sediments from high-resolution paleomagnetic data. *Geochemistry, Geophysics, Geosystems* 13: Q0AO03.
- Solomina, O. N., R. S. Bradley, D. A. Hodgson, S. Ivy-Ochs, V. Jomelli, A. N. Mackintosh, A. Nesje, L. A. Owen, H. Wanner, G. C. Wiles, and N. E. Young. 2015. Holocene glacier fluctuations. *Quaternary Science Reviews* 111: 9-34.
- Spielhagen, R. F., K. H. Baumann, H. Erlenkeuser, N. R. Nowaczyk, N. Norgaard-Pedersen, C. Vogt, and D. Weiel. 2004. Arctic Ocean deep-sea record of northern Eurasian ice sheet history. *Quaternary Science Reviews* 23: 1455-1483.
- Spielhagen, R. F., K. Werner, S. A. Sorensen, K. Zamelczyk, E. Kandjano, G. Budeus, K. Husum, T. M. Marchitto, and M. Hald. 2011. Enhanced Modern Heat Transfer to the Arctic by Warm Atlantic Water. *Science* 331: 450.
- St-Onge, G., and C. Hillaire-Marcel. 2001. Isotopic constraints of sedimentary inputs and organic carbon burial rates in the Saguenay Fjord, Quebec. *Marine Geology* 176: 1-22.
- St-Onge, G., T. Mulder, P. Francus, and B. Long. 2007. Chapter Two Continuous Physical Properties of Cored Marine Sediments, p. 63-98. In C. Hillaire-Marcel and A. De Vernal [eds.], *Developments in Marine Geology*. Elsevier.
- St-Onge, M.-P., and G. St-Onge. 2014. Environmental changes in Baffin Bay during the Holocene based on the physical and magnetic properties of sediment cores. *Journal of Quaternary Science* 29: 41-56.

- Steffen, K., and A. Ohmura. 1985. Heat Exchange and Surface Conditions in North Water Northern Baffin Bay. *Annals of Glaciology* 6: 178-181.
- Stirling, I. 1980. The Biological Importance of Polynyas in the Canadian Arctic. *Arctic* 33: 303-315.
- Stoner, J. S., and G. St-Onge. 2007. Chapter Three Magnetic Stratigraphy in Paleoceanography: Reversals, Excursions, Paleointensity, and Secular Variation, p. 99-138. In C. Hillaire-Marcel and A. De Vernal [eds.], *Developments in Marine Geology*. Elsevier.
- Stuiver, M., Reimer, P.J., Reimer, R.W., 2017. CALIB 7.1. Available online at: calib.qub.ac.uk/calib.
- Stuut, J.-B. W., F. Temmesfeld, and P. De Deckker. 2014. A 550 ka record of aeolian activity near North West Cape, Australia: inferences from grain-size distributions and bulk chemistry of SE Indian Ocean deep-sea sediments. *Quaternary Science Reviews* 83: 83-94.
- Tang, C. C. L., C. K. Ross, T. Yao, B. Petrie, B. M. DeTracey, and E. Dunlap. 2004. The circulation, water masses and sea-ice of Baffin Bay. *Progress in Oceanography* 63: 183-228.
- Tauxe, L. 1993. Sedimentary records of relative paleointensity of the geomagnetic field: Theory and practice. *Reviews of Geophysics* 31: 319-354.
- Tauxe, L., T. Pick, and Y. S. Kok. 1995. Relative paleointensity in sediments: A Pseudo-Thellier Approach. *Geophysical Research Letters* 22: 2885-2888.
- Thomas, E. K., Y. Huang, J. P. Briner, and S. McGrane. 2010. An assessment of leaf wax hydrogen isotopes as a climate proxy in proglacial arctic lake sediments, p. PP51A-1604.
- Thomas, E. K., J. P. Briner, J. J. Ryan-Henry, and Y. Huang. 2016. A major increase in winter snowfall during the middle Holocene on western Greenland caused by reduced sea ice in Baffin Bay and the Labrador Sea. *Geophysical Research Letters* 43: 5302-5308.

- Thorsteinsson, R., and Mayr, U. 1987. The sedimentary rocks of Devon Island, Canadian Arctic Archipelago. Geological Survey of Canada, Memoir 411. 182p.
- Trettin, H.P. 1991. Chapter 4 Tectonic Framework. In Geology of the Innuitian Orogen and Arctic Platform of Canada and Greenland. Edited by H.P. Trettin. Geological Survey of Canada, Geology of Canada, 3: 59–66.
- Turekian, K. K., and K. H. Wedepohl. 1961. Distribution of the Elements in Some Major Units of the Earth's Crust. GSA Bulletin 72: 175-192.
- Van Wychen, W., L. Copland, L. Gray, D. Burgess, B. Danielson, and M. Sharp. 2012. Spatial and temporal variation of ice motion and ice flux from Devon Ice Cap, Nunavut, Canada. Journal of Glaciology 58: 657-664.
- Van Wychen, W., J. Davis, D. O. Burgess, L. Copland, L. Gray, M. Sharp and C. Mortimer. 2016. Characterizing interannual variability of glacier dynamics and dynamic discharge (1999–2015) for the ice masses of Ellesmere and Axel Heiberg Islands, Nunavut, Canada. Journal of Geophysical Research: Earth Surface 121: 39-63.
- Van Wychen, W., J. Davis, L. Copland, D. O. Burgess, L. Gray, M. Sharp, J. A. Dowdeswell, and T. J. Benham. 2017. Variability in ice motion and dynamic discharge from Devon Ice Cap, Nunavut, Canada. Journal of Glaciology 63: 436-449.
- von Eynatten, H., C. Barceló-Vidal, and V. Pawlowsky-Glahn. 2003. Composition and Discrimination of Sandstones: A Statistical Evaluation of Different Analytical Methods. Journal of Sedimentary Research 73: 47-57.
- Walker, M. J. C., M. Berkelhammer, S. Björck, L. C. Cwynar, D. A. Fisher, A. J. Long, J. J. Lowe, R. M. Newnham, S. O. Rasmussen, and H. Weiss. 2012. Formal subdivision of the Holocene Series/Epoch: a Discussion Paper by a Working Group of INTIMATE (Integration of ice-core, marine and terrestrial records) and the Subcommission on Quaternary Stratigraphy (International Commission on Stratigraphy). Journal of Quaternary Science 27: 649-659.

- Weltje, G. J. 1997. End-member modeling of compositional data: Numerical-statistical algorithms for solving the explicit mixing problem. *Mathematical Geology* 29: 503-549.
- Williams, K. M. 1990. Late Quaternary paleoceanography of the western Baffin Bay region: evidence from fossil diatoms. *Canadian Journal of Earth Sciences* 27: 1487-1494.
- Zhang D 2000. Flux de radio-isotopes à courte périodes dans les bassins marins marginaux de l'est canadien. PhD Thesis, Université du Québec à Montréal.
- Zhang, S., Mirza, K., and Barnes, C.R. 2016. Upper Ordovician – Upper Silurian conodont biostratigraphy, Devon Island and southern Ellesmere Island, Canadian Arctic Islands, with implications for regional stratigraphy, eustasy and thermal maturation. *Canadian Journal of Earth Sciences*, 53: 931–949.
- Zweng, M. M., and A. Münchow. 2006. Warming and freshening of Baffin Bay, 1916–2003. *Journal of Geophysical Research: Oceans* 111: C07016.

